Track Reconstruction and Point Source Searches with ANTARES

The picture on the cover was produced with the event display program, A3D, which was developed in the context of the work for this thesis. The image shows a simulated neutrino with an energy of 30 TeV, which interacts just below the sea bed to produce an 11 TeV muon. The optical modules are represented by the small spheres. The larger, coloured spheres represent the hits. The size of the spheres is a measure of the hit amplitude, while the colour encodes the detection time (according to the figure on the back). Lines connecting the hits to the muon track indicate the path of the Cherenkov photons. Hits which are not connected to the muon track are background hits. For clarity, the distance between the optical modules and the string is exaggerated by a factor of four. The grid drawn on the sea bed measures 300×300 m^2.
The image in the background is a photograph of the star Antares (top-right) and its surroundings. I thank the photographer, Rick Krejci, for his kind permission to use this image.

ISBN 90 6464 510 8

Track Reconstruction and Point Source Searches with ANTARES

Academisch Proefschrift

ter verkrijging van de graad van doctor
aan de Universiteit van Amsterdam
op gezag van de Rector Magnificus
prof.mr. P.F. van der Heijden
ten overstaan van een door het college voor promoties
ingestelde commissie, in het openbaar te verdedigen
in de Aula der Universiteit
op dinsdag 8 juni 2004, te 10:00 uur

door

Adriaan Jacob Heijboer

geboren te Breda

Promotor: Prof.Dr. J.J. Engelen
Co-promotor: Dr. E. de Wolf

Faculteit der Natuurwetenschappen, Wiskunde en Informatica

Aan mijn ouders

Contents

Introduction

As we know, there are known knowns. There are things we know we know.
We also know there are known unknowns.
That is to say, we know there are some things we do not know.
But there are also unknown unknowns: the ones we don't know we don't know.
— D.H. Rumsfeld

In 2002, the Nobel prize for physics was awarded to Raymond Davis, Masatoshi Koshiba, and Riccardo Giacconi. Giacconi is one of the founders of the field of X-ray astronomy. Davis and Koshiba were awarded the prize *"for pioneering contributions to astrophysics, in particular for the detection of cosmic neutrinos"*.

Davis and his colleagues were the first to take on the challenge to measure neutrinos from the Sun by detecting the reaction $\nu_e + {}^{37}\mathrm{Cl} \rightarrow {}^{37}\mathrm{Ar} + e^-$ in a tank of chlorine [1]. The detection of these neutrinos proved that nuclear fusion is the energy source of the Sun. However, the number of detected neutrinos was smaller than what was predicted by models of the nuclear processes in the Sun. These observations were confirmed, amongst others, by the group headed by Koshiba using the Kamiokande-II detector [2]. In 1998, the successor of this experiment, called Super-Kamiokande, observed evidence for oscillations of atmospheric muon-neutrinos, which implies a non-zero neutrino mass. Since then, it has become widely accepted that neutrino oscillations also offer an explanation for the observed deficit of solar neutrinos. The final piece of this puzzle was provided in 2002 by the SNO experiment. By measuring (flavour blind) neutral current interactions, this experiment showed that the total number of neutrinos is in agreement with the model predictions [3]. The missing electron-neutrinos must therefore have oscillated into muon- or τ-neutrinos.

In 1987, the Kamiokande-II [4] and IMB [5] detectors observed a total of 20 neutrinos from a supernova explosion in the Large Magellanic cloud, thereby confirming the theoretical models for core collapse supernovae. The observation of cosmic neutrinos has thus not only lead to an increase in our understanding of the Sun and of supernova explosions, but it has also provided new knowledge in the field of particle physics. In fact, the existence of massive neutrinos is one of the few experimental results available today that hint directly at physics beyond the standard model of particle physics. Interestingly, other clues also seem to come predominantly from the field of astronomy (e.g. dark matter) or cosmology (dark energy).

Another longstanding problem that involves both particle physics and astronomy is the origin of high energy cosmic rays. Since their discovery in 1912, it has become clear that primary cosmic rays consist of protons and nuclei that have been accelerated up to

(very) high energies. The acceleration is thought to take place in astrophysical objects that release large amounts of energy, such as Active Galactic Nuclei, Gamma Ray Bursts and (Galactic) Supernova remnants. However, this hypothesis cannot easily be tested because the detected cosmic rays do not point to their source, because they are deflected by the magnetic fields in the universe. Fortunately, many models of cosmic ray acceleration predict that a fraction of the accelerated particles interacts with matter or photons in the source. These interactions inevitably produce neutrinos, which will escape from the acceleration region. Since the neutrinos are not perturbed by magnetic fields, their detection could make it possible to identify the source, thus providing evidence for the acceleration of cosmic rays in that source.

More generally, at very high energies astronomy with photons becomes infeasible, because they are absorbed on the low energy photons from the cosmic background radiation. This limits the path length of a 10 TeV photon, for example, to roughly the distance of the nearest active galaxy [6]. In contrast, neutrinos offer a means to study the universe at very high energies or large distances. Moreover, they can be used to study dense regions of the universe from which photons can not escape.

Whereas the neutrinos produced in the Sun and in supernova explosions have energies of the order of several MeVs, the neutrinos produced by cosmic ray accelerators are thought to have much higher energies. The ANTARES detector, which is described in this thesis, is being built to detect these neutrinos. Focusing on high energy neutrinos has several advantages: 1) The cross-section for neutrino interactions increases with energy, which enhances the detection probability. 2) The energetic reaction products are detectable with a sparsely instrumented detector. This makes it possible to use very large (natural) detection volumes cost effectively. 3) The direction of the particles produced in a neutrino interaction is closely correlated to the direction of the neutrino. The direction of the neutrino can thus be determined, provided that the direction of the reaction products can be determined.

In this thesis, the emphasis is on the detection of muon-neutrinos. The direction of the muon that is produced in a charged current interaction, must be reconstructed from the measurement of the Cherenkov light it emits while traversing the detector. A method that was developed for this purpose is one of the subjects of this thesis. If multiple neutrinos will be observed from the same direction in the sky, this may indicate the presence of a point-like source of neutrinos. A method to search for point sources and the expected discovery potential of the ANTARES detector are also presented.

This thesis is organised as follows. In chapter 1 a brief overview of the knowledge of cosmic rays and the mechanism for neutrinos production is given. Chapter 2 starts with an introduction to the ANTARES experiment. This is followed by a summary of the first measurements that were obtained with a small prototype detector. In chapter 3 the tools used for the simulation of the neutrino interaction, the propagation of the muon and the response of the detector are described. Chapter 4 describes the method that was developed for the reconstruction of the direction of the muons that traverse the detector, which is of crucial importance for the pointing accuracy of the telescope. The method used to reconstruct the muon energy is also briefly discussed. In chapter 5 it is discussed how the background from atmospheric muons can be rejected. This is followed by a discussion of the detector performance in terms of pointing accuracy and effective area.

In chapter 6 a method is presented that can be used to search for astrophysical point sources of neutrinos. This leads to an estimate of the discovery potential of the final ANTARES detector.

Chapter 1

Cosmic ray acceleration and neutrino production

The motivation for the attempts to detect cosmic neutrinos is related to the present (lack of) knowledge on high energy Cosmic Rays (CRs). The very high energies these particles can reach suggest that some astrophysical objects are capable of particle acceleration up to high energies. However, the sources of the CRs cannot be directly identified, because their directions are randomised by the (inter-)galactic magnetic fields. One way of identifying CR sources is via detection of neutrinos produced by interactions of CR in or around the source.

Section 1.1 contains a brief discussion of CRs and the mechanism by which they may be accelerated. This is relevant because the question of the CR origin is one of the main motivations for the search for point sources of high energy cosmic neutrinos, but also because the CR spectra at the source are an ingredient for models of neutrino production. Some aspects of these models and candidate neutrino sources are the topic of section 1.2. A more extensive discussion of CRs and neutrino production can be found in e.g. [7] and [8].

1.1 Cosmic rays

High energy protons and nuclei are detected directly by experiments on board satellites and balloons and indirectly by observing the extensive air showers they cause in the Earth's atmosphere. The measured flux of high energy protons and nuclei impinging on the Earth's atmosphere is shown in figure 1.1. The energies of the particles span many orders of magnitude, up to energies above 10^{20} eV. The differential flux can be described by a power law:

$$\frac{dN}{dE} \propto E^{-\gamma}, \tag{1.1}$$

where γ is the spectral index. The measured value of γ changes from about 2.7 to about 3.0 at an energy of roughly 3×10^{15} eV. This feature is known as the 'knee' of the spectrum. At energies of about 3×10^{18} eV, the spectral index changes again to a value of about 2.7. This feature is known as the 'ankle'.

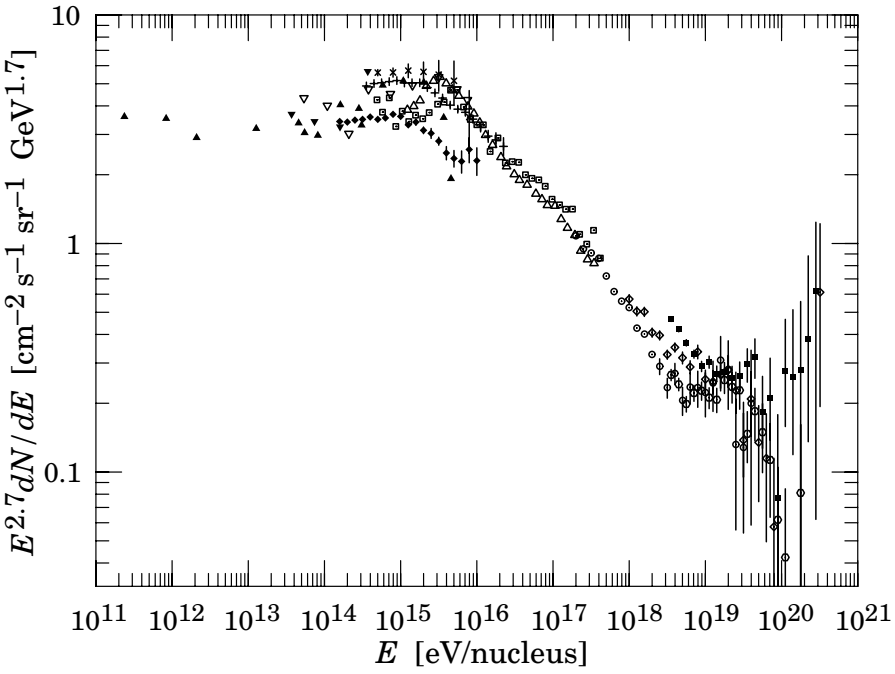

Figure 1.1: *The all particle spectrum of cosmic rays taken from [9].*

For a relativistic particle with electric charge q and energy E in a magnetic field B, the radius of gyration is given by the Larmor radius $R_L = E/qB$. In the Galactic magnetic field protons with energies up to 10^{18} eV have a Larmor radius which is smaller than the size of the Galaxy and can remain confined to the Galaxy. Up to these energies, CRs are therefore thought to have a Galactic origin. The flattening of the spectrum at the ankle may be associated with the onset of the extra-Galactic component.

1.1.1 Shock acceleration

The mechanism most likely responsible for accelerating particles up to observed CR energies is known as 'shock acceleration' or 'first order Fermi acceleration' (see [7] or [10] for more details). This process occurs when two plasmas collide, forming a shock at the boundary. In this model, particles are magnetically confined to the source and they are elastically scattered by magnetic irregularities that are frozen into the plasma. On both sides of the shock front, the scattering will result in an isotropic velocity distribution of the particle with respect to the local medium. Figure 1.2 depicts the situation in the 'lab' frame, where the shock propagates through the stationary interstellar medium with velocity V_s. The velocity u of the matter behind the shock is related to the shock velocity by hydrodynamics. In case the shock speed is much larger than the speed of sound in the plasma, the relation is [10]

$$u = \frac{3}{4} V_s. \tag{1.2}$$

When a relativistic particle with energy E_1 crosses the shock front from the unshocked to the shocked medium at an angle θ_1, its energy in the rest frame of the shocked medium is

$E_1' = \Gamma E_1(1 + \frac{u}{c}\cos\theta_1)$, where $\Gamma = (1 - \frac{u^2}{c^2})^{-\frac{1}{2}}$. This energy will not change in the elastic scattering. When the particle enters the unshocked medium again, under an angle θ_2' as measured from the shocked medium, its energy is

$$E_2 = \Gamma^2 E_1(1 + \frac{u}{c}\cos\theta_1)(1 + \frac{u}{c}\cos\theta_2'). \tag{1.3}$$

For isotropic fluxes, average values of $\cos\theta_1$ and $\cos\theta_2'$ for particles crossing the shock front are $\langle\cos\theta_1\rangle = \langle\cos\theta_2'\rangle = 2/3$. The average fractional energy increase ϵ is thus given by

$$\epsilon \equiv \left\langle \frac{\Delta E}{E} \right\rangle = \frac{E_2 - E_1}{E_1} = \frac{4}{3}\frac{u}{c} = \frac{V_s}{c}, \tag{1.4}$$

where terms of order $\frac{u^2}{c^2}$ are neglected. Thus, the energy of the particle is increased by a constant factor every time it goes back and forth over the shock front.

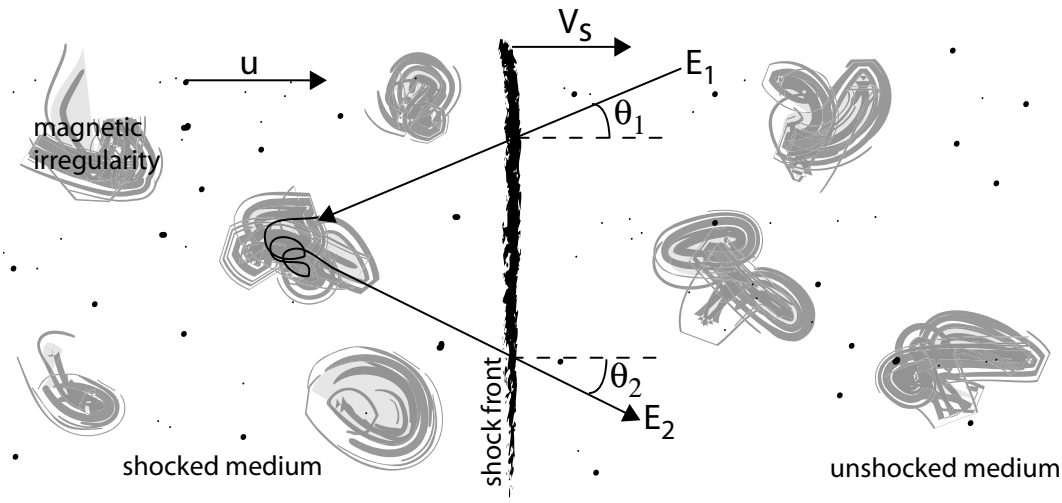

Figure 1.2: *Cartoon of the shock acceleration mechanism. A particle moves from the unshocked medium, which is at rest in this picture, into the shocked medium, where it elastically scatters on the irregular magnetic fields. When returning back to the unshocked medium, the particle has gained a fraction V_s/c of its original energy.*

Particles are advected away from the shock region together with the shocked material with velocity $V_s/4$. The number of particles escaping from the source per unit time and area is therefore $\rho V_s/4$, where ρ is the density of cosmic rays. The flux of particles crossing the shock back into the unshocked medium follows from the projection of an isotropic flux on the plane of the shock front. It is given by $c\rho/4$. The probability that a particle escapes from the shock region by advection instead of crossing back into the unshocked medium, is therefore $P_{\rm esc} = V_s/c$. The combination of a constant increase in energy ϵ with a constant escape probability $P_{\rm esc}$, gives rise to a power law spectrum:

$$\frac{dN}{dE} \propto E^{-\gamma} = E^{-1+\frac{\ln(1-P_{\rm esc})}{\ln(1+\epsilon)}}. \tag{1.5}$$

The values of $P_{\rm esc}$ and ϵ derived above are both much smaller than one and lead to a value for the spectral index of $\gamma = 2$. More detailed calculations indicate that values between 2.1 and 2.4 may be more realistic [6]. Nevertheless, many models of neutrino production assume a 'generic' spectrum of protons proportional to E^{-2}.

The acceleration stops when the particles can no longer be confined to the source region by the magnetic field, when the energy loss via synchrotron radiation or inelastic interactions becomes comparable to the energy gain from the acceleration process, or when the shock decays.

The observed CR spectrum is steeper than the typical spectra predicted by the shock acceleration mechanism. This can be explained by models of CR propagation through the galaxy, which predict that high energy CRs have a higher probability to escape from the Galactic magnetic field. The remaining particles therefore have a steeper spectrum. For extra-Galactic sources, the steepness of the observed spectrum is influenced by redshift and the GZK effect [11] [12]. The expected shape of the spectrum at very high energies therefore depends on the distribution of CR sources in the universe.

1.2 Neutrinos

The sources of CRs can not be identified easily, since the directional information of the particles is lost as they propagate through the (inter-)galactic magnetic field. Instead, the sources could be identified by observing neutrinos that are produced in interactions of CRs in or near the source.

1.2.1 Neutrino production

Models of neutrino production rely on interactions of accelerated protons (or nuclei) with photon or matter fields in or near the accelerating astrophysical objects. In these interactions, charged and neutral pions are produced:

$$p + \gamma \text{ or } p \rightarrow N_1\pi^{\pm} + N_2\pi^0 + X, \tag{1.6}$$

where $N_1 \approx N_2$. The charged pions then decay to give neutrinos, while neutron pions decay into photons:

$$\begin{aligned} \pi^+ &\rightarrow \mu^+ + \nu_\mu \rightarrow e^+ + \nu_e + \nu_\mu + \bar{\nu}_\mu \\ \pi^- &\rightarrow \mu^- + \bar{\nu}_\mu \rightarrow e^- + \bar{\nu}_e + \nu_\mu + \bar{\nu}_\mu \\ \pi^0 &\rightarrow \gamma + \gamma. \end{aligned} \tag{1.7}$$

The exact value of the ratio between the number of charged and neutral pions depends on the type (p or γ) and on the centre of mass energy, but the numbers of produced photons and neutrinos[1] are always roughly equal [13]. The fluxes of neutrinos and high energy photons are therefore closely related. In many environments, however, the high energy photons from the π^0 decay initiate electro-magnetic cascades via the production of e^+e^--pairs. The result is that the energy of the photons is emitted as non-thermal

[1] Since neutrino telescopes can not distinguish between ν and $\bar{\nu}$, this distinction is not made.

radiation at lower energies (where the cross section for pair production has decreased to the point where photons can escape). As a result, only the bolometric (i.e. integrated over energy) fluxes of photons and neutrinos are related. Many models of the neutrino fluxes are therefore normalised to (some fraction of) the X-ray or gamma ray luminosity of the source. It should, however, be noted that this is not a very robust procedure, since non-thermal radiation can also be generated through synchrotron radiation of electrons (in which case no neutrinos are predicted).

The shape of the neutrino spectrum is calculated from the shape of the spectrum of the interacting protons, which is almost always taken to be proportional to E^{-2}, and from the spectrum of the target photons or protons. Near the pion production threshold, interactions with photons occur predominantly via the Δ^+ resonance:

$$p + \gamma \rightarrow \Delta^+ \rightarrow \pi^+ + n, \tag{1.8}$$

which establishes a relation between the energies of the interacting photon and proton:

$$4E_p E_\gamma = c^4(M_\Delta^2 - M_p^2). \tag{1.9}$$

For high proton energies, roughly 20% of the proton energy is transferred to the pion and the neutrinos finally acquire about 5% of the proton energy. The neutrino spectrum thus follows the distribution of the energy of the interacting protons, which can be calculated by computing the number of $p\gamma$ pairs available for Δ production. The relevant photon spectra are often known from observations. For a sharply peaked photon spectrum, as is the case for a thermal radiation field, the neutrino energy spectrum follows the shape of the proton spectrum (E^{-2}). In many sources, the target photons are non-thermal and have a (broken) power law spectrum, which results in a break in the predicted neutrino spectrum. If interactions with protons dominate, the centre of mass energy is virtually always above the pion production threshold and the produced spectrum of neutrinos follows the proton energy spectrum (see e.g.[14]).

1.2.2 Candidate neutrino sources

Many astrophysical objects exhibiting non-thermal photon spectra, which hints at particle acceleration. If hadrons are accelerated in these objects, they could be sources of high energy neutrinos. A number of candidate sources is discussed below.

Active Galactic Nuclei: Active Galactic Nuclei (AGN) are objects associated with the centres of galaxies. The amount of energy released by these objects as non-thermal radiation exceeds that of any other type of object known. The energy is thought to be provided by the gravitational energy of matter falling onto a super-massive (10^8 Solar masses) black hole. In some cases, AGNs are observed to emit relativistic jets. Models exist for neutrino production in both the accretion disk, where the target for photomeson production is provided by thermal photons, and in the jets, where the target can also consist of synchrotron photons [15]. Neutrino production in jets is particularly interesting if the jet axis is oriented along the line of sight. Such objects are called blazars.

Gamma ray bursts: Gamma ray bursts (GRBs) are short, very luminous eruptions of MeV photons. The observed radiation is believed to be produced by electrons that are accelerated by shock waves in relativistic ($\Gamma \approx 300$) jets. It is suggested in [16] that protons accelerated in GRBs may be responsible for the highest energy CRs. If protons are indeed accelerated in GRBs, the MeV photons provide a target for photomeson production [17]. In this model, the neutrino flux is thus normalised to the CR flux and may be detectable by ANTARES (see section 6.6). There is recent evidence that GRBs are associated with supernovae [18]. If the GRB and supernova occur simultaneously, neutrinos are also generated while the GRB jet is still burrowing its way through the stellar envelope [19].

Supernova Remnants: The matter ejected in supernova explosions collides with interstellar matter, forming a shock wave at which particle acceleration may occur. These supernova remnants (SNRs) are thought to be responsible for the production of the bulk of the CRs with energies up to about 10^{15} eV. Interactions of CRs with ambient matter are expected to produce neutrinos and gamma rays via decay of charged and neutral pions. Indeed, a number of SNRs have been observed to emit gamma rays of energies up to the TeV range. For one SNR, it has been claimed that the TeV gamma spectrum is indicative of π^0 decay [20], which would be evidence for the acceleration of protons. However, such claims are controversial [21] and models that explain the TeV emission by inverse Compton scattering of accelerated electrons on ambient photons are not considered obsolete.

In a sub-class of SNRs, a rapidly spinning neutron star, which is the residue of the progenitor star, fills the SNR with a 'pulsar wind' consisting of electrons and positrons emitting strong synchrotron radiation. Such configurations are called plerions. Acceleration of protons and nuclei could take place at shocks in the pulsar wind [7]. Alternatively, the magnetic field configuration of a rapidly rotating neutron star could lead to acceleration of protons and nuclei [22]. The supernova remnant would provide a target for these particles. The neutrino fluxes are usually predicted by assuming that (part of) the observed gamma ray flux is produced by the decay of π^0s, which should be produced in roughly equal amounts as $\pi^{\pm}$s, which produce neutrinos [23] [24].

Microquasars: Microquasars are Galactic X-ray binary systems, which exhibit relativistic jets. They are believed to consist of a central stellar mass black hole or neutron star that accretes matter from a companion star. Microquasars thus resemble AGNs, but on a much smaller scale. If, in addition to electrons, hadrons are accelerated in the jet, interactions with the synchrotron photons produced by accelerated electrons would lead to neutrino production [25]. In [26] neutrino fluxes and event rates are predicted for a number of Galactic microquasars. Some of them may be detectable by ANTARES as will be shown in section 6.6.

Figure 1.3 shows a compilation of flux predictions for point-like sources of neutrinos, taken from [6]. In section 6.6 we will comment the sensitivity of ANTARES to these fluxes.

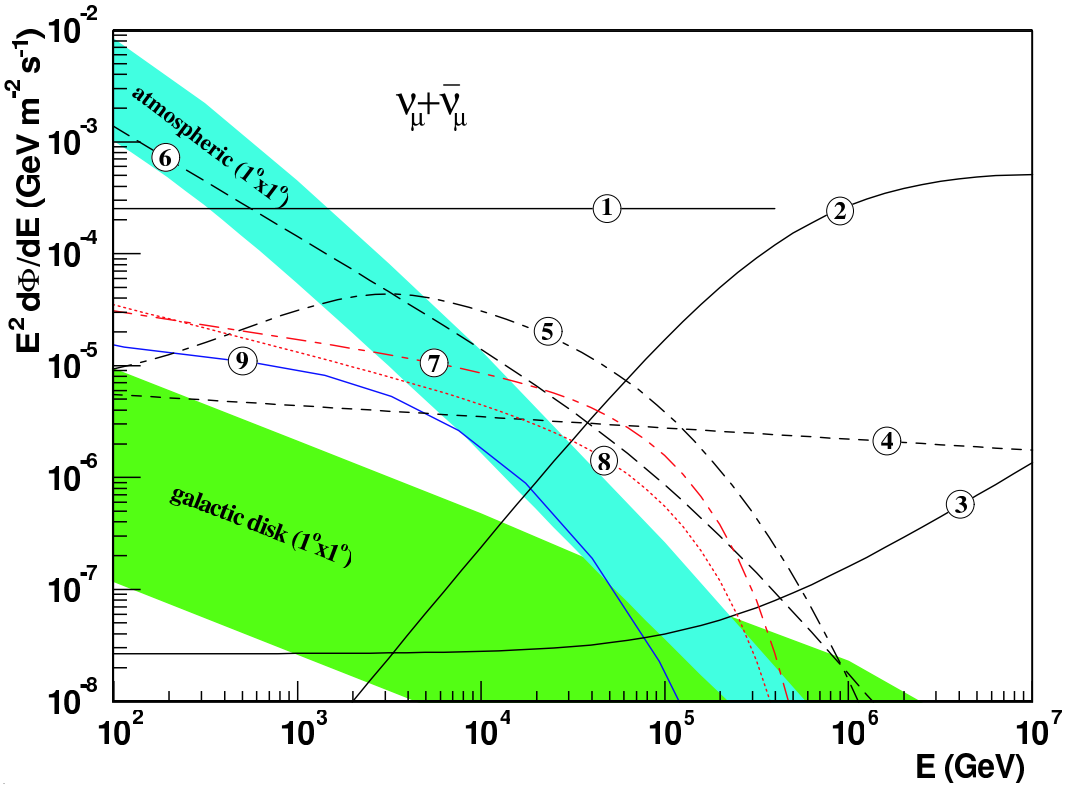

Figure 1.3: *Summary of neutrino flux models for point sources of ν_μs. The diffuse atmospheric neutrino flux and the flux of CR neutrinos from the Galactic disc have been integrated over a $1° \times 1°$ solid angle.* ① *AGN core model (with pp interactions) by Nellen et. al. [14] for 3C273 or similarly for Mrk501 during its bursting phase in 1997, if it emits half of the TeV gamma ray flux in neutrinos.* ② *Stecker and Salomon [15] for 3C273 due to $p\gamma$ interactions.* ③ *Mannheim [27] model for the jet of 3C273.* ④ *Colafrancesco et al. [28] model for the Coma cluster of galaxies.* ⑤ *Bednarek and Protheroe [29] model for the Crab nebula.* ⑥ *Ingelman and Thunman [30] model for neutrinos produced by CR interactions in the Sun.* ⑦ *Gaisser et al. [31] model for SNR IC443.* ⑧ *idem for γ Cygni.* ⑨ *Atoyan et al. [32] model for SNR CasA. Figure taken from [6].*

1.2.3 Other sources of neutrinos

Detection of cosmic neutrinos produced via proton acceleration is the main goal of large neutrino telescopes such as ANTARES, but other sources of neutrinos are known to exist. In addition there are some speculative sources that could provide an interesting neutrino signal. The most important sources of neutrinos are listed below.

Atmospheric neutrinos: Cosmic rays interact in the Earth's atmosphere, producing a shower of particles. In this shower, neutrinos are produced through the decay of charged pions (and also kaons and charmed mesons). The resulting neutrino flux dominates any (hypothetical) cosmic neutrino flux at low energies. Thousands of these neutrinos will be detected by ANTARES.

Cosmic ray neutrinos from the Galactic disc: Diffuse CRs propagating through the Galaxy will interact with the interstellar medium and produce gamma rays (from π^0) and neutrinos (from $\pi^{\pm}$ decay). As a result, one expects part of the neutrino flux to be correlated with the matter density in the Galaxy.

GZK neutrinos: If the highest energy CRs are produced at cosmological distances and the GZK effect exists, the energy lost by the protons will be converted into neutrinos and photons of very high energy. Only the neutrinos can propagate further and can be detected. Having very high energies and a flux comparable to the flux of the highest energy CRs, they could be detected by experiments like AUGER [33].

Neutrinos from dark matter annihilation: There is evidence that a large fraction of the matter in the Universe must be non-baryonic. One possibility is that this matter consists of WIMPs (weakly interacting massive particles), which may be associated with the particles predicted by supersymmetric extensions of the Standard Model. The supersymmetric partners of the Higgs and gauge bosons combine into mass eigenstates called neutralinos. The lightest neutralino could be stable, which would make it a viable dark matter candidate.

Neutralinos produced shortly after the big bang, may become gravitationally bound to astrophysical objects like the Sun, Earth or the Calactic centre, where they lose energy in elastic interactions with ordinary matter. The result is a dense population of neutralinos, which may then lead to annihilation. Depending on the properties of the neutralino, the annihilation produces a mix of gauge and Higgs bosons and heavy fermions, which subsequently decay. Among the decay products are gamma rays and neutrinos. The latter are particularly interesting when the neutralinos are clustered in the core of objects that are opaque to gamma rays. Neutrinos from neutralino annihilation in the centre of the Sun may be detected by ANTARES for certain supersymmetric models [34].

1.2.4 Effect of neutrino oscillations on the flux

Being unaffected by magnetic fields, photons and large column densities of matter, neutrinos can propagate freely through the universe without being absorbed or deflected. The only complication is that oscillations of neutrinos will induce flavour changes while the neutrinos propagate through the universe.

The present knowledge on neutrino mixing is summarised in [35]. The smallest allowed Δm^2 is 5.4×10^{-5} eV^2/c^2. For neutrino energies below a PeV, this leads to an oscillation length $\lesssim 0.01$ lightyear. The potential sources of cosmic neutrinos are thus located many oscillation lengths away. On Earth, all oscillations will be averaged out, so that the probability of a neutrino changing flavour from α to β is given by the 'classical limit':

$$P(\nu_\alpha \rightarrow \nu_\beta) = \sum_i |U_{\alpha i}|^2 |U_{\beta i}|^2, \tag{1.10}$$

Where U is the 3×3 neutrino mixing matrix and the summation is over the three mass eigenstates.

The neutrino mixing matrix is now fairly well constrained by a global fit to data from Solar, atmospheric, accelerator and reactor experiments [36]. This allows the flavour composition of the neutrino flux on Earth to be calculated as a function of the composition at production. The flavour composition expected from charged pion decay is $\nu_e : \nu_\mu : \nu_\tau = 1 : 2 : 0$ (see equation 1.7). In environments with very high magnetic fields, the muons lose energy due to synchrotron radiation before decaying, leading to a suppression of the ν_e flux with respect to the ν_μ flux. In the extreme case this leads to a flavour mixture $\nu_e : \nu_\mu : \nu_\tau = 0 : 1 : 0$. For either mixture, the resulting neutrino flux at the Earth has been calculated. The result is shown in figure 1.4. One can see that all neutrino flavours occur with roughly the same flux, regardless of the composition at production. The flux of muon neutrinos is reduced by a factor 2 (or 3 in case $\nu_e : \nu_\mu : \nu_\tau = 0 : 1 : 0$). It is furthermore clear that, for the purpose of neutrino astronomy, the neutrino mixing matrix is already sufficiently constrained, since neutrino mixing only accounts for a systematic uncertainty of about 20%.

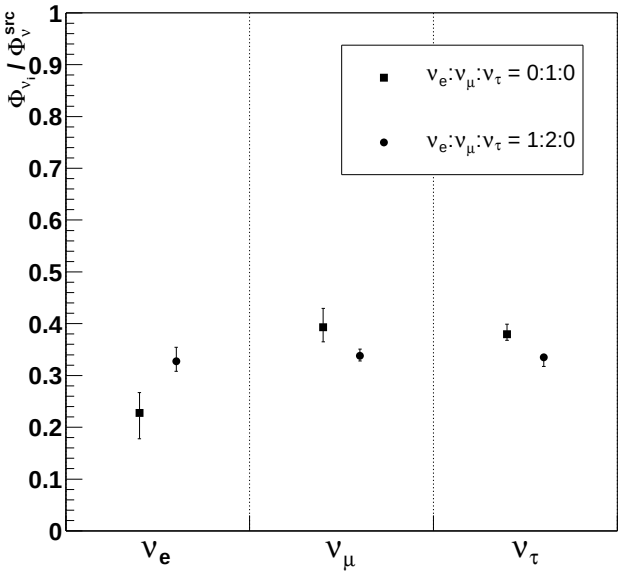

Figure 1.4: *Fluxes of the three neutrino flavours at the Earth as a fraction of the total flavour neutrino flux for a source producing only muon neutrinos and for a source producing a mix of electron and muon neutrinos in proportion* $1 : 2$. *The error bars are calculated using the allowed values of the mixing angles at 1* σ *confidence level.*

Chapter 2

The ANTARES detector

In this chapter, the basic principles of large underwater neutrino telescopes are discussed. The detector that is being built by the ANTARES collaboration is described. A summary of the first results obtained with a prototype detector is presented in section 2.4.

2.1 High energy neutrino telescopes

2.1.1 Detection principle

The detection principle is depicted in figure 2.1. Neutrinos are detected when they interact with a nucleon[1] N via either charged current ($\nu_l + N \rightarrow l + X$) or neutral current ($\nu_l + N \rightarrow \nu_l + X$) weak interactions. Relativistic charged particles produced by the neutrino interaction emit Cherenkov radiation in the sea water. The detector operates by detecting the intensity and arrival time of this light on a three-dimensional array of PhotoMultiplier Tubes (PMTs). From these measurements, the properties of the neutrino are inferred.

The experimental signature depends on the type of reaction and on the neutrino flavour (see figure 2.2). In general, high energy neutrino interactions result in the breakup of the target nucleon. The remnants form a hadronic shower. The Cherenkov light emitted by the charged particles in the shower can be detected if the interaction occurs inside or near the instrumented volume of the detector. In the case of a neutral current interaction, only the hadronic shower can be detected, while charged current interactions will produce charged leptons that produce additional light. The electron resulting from a charged current ν_e interaction will produce an electro-magnetic shower. Muons, resulting from ν_μ interactions can travel a considerable distance before they are stopped. In ν_τ interactions, the produced τ-lepton travels some distance (depending on its energy) before it decays and produces a second shower.

In this thesis the focus will be on up-going muon neutrinos, which are especially interesting for a search for point sources in the energy range between about 100 GeV and 1 PeV. In this energy range, the hadronic shower can occur outside the detector volume, while the muons are energetic enough to completely traverse the detector. This gives a clean experimental signal which allows accurate reconstruction of the muon direction.

[1] For our purposes, cross-sections for interaction with atomic electrons are negligible, except in the case of $\bar{\nu}_e$, which can interact via the exchange of a resonant W^- at $E_{\bar{\nu}_e} = 6.3$ PeV [37].

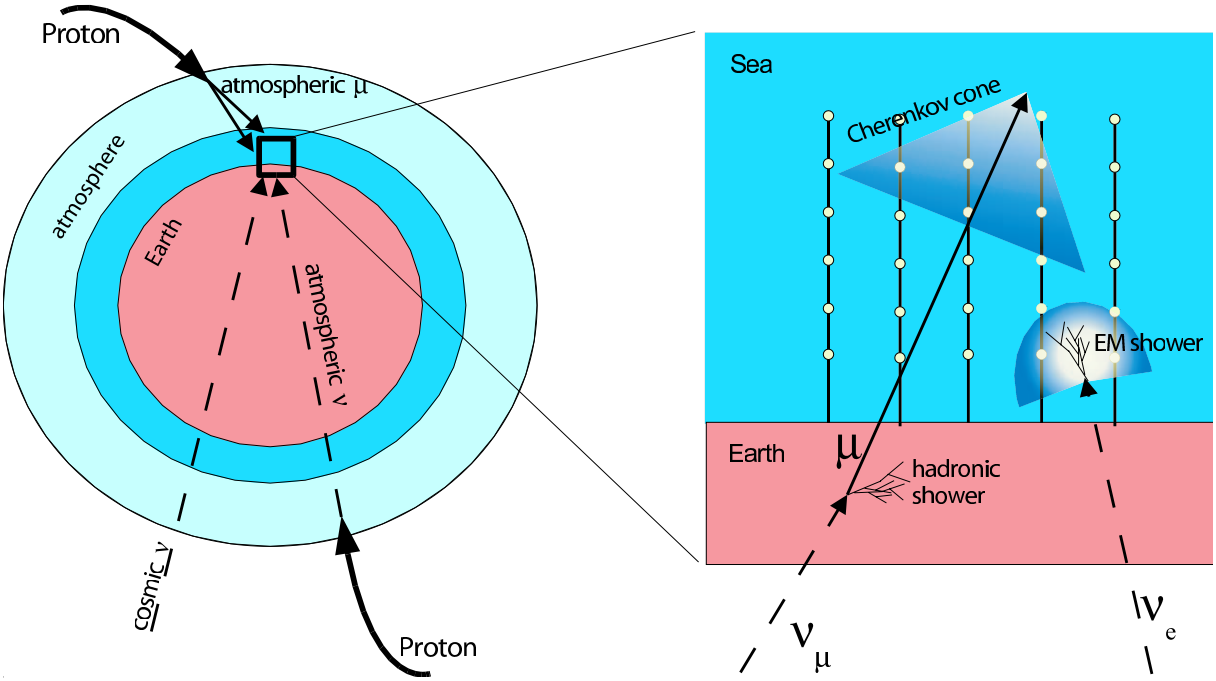

Figure 2.1: *Detection principle of neutrino telescopes. After having traversed the Earth, neutrino interactions can produce up-going muons or electrons. The Cherenkov light they produce in the sea water is detected by an array of photomultiplier tubes. The main background consists of atmospheric muons. Up-going muons produced by atmospheric neutrinos also form a background.*

As will be shown in chapter 3, the directions of the muon and the neutrino are closely correlated, which allows for accurate determination of the neutrino direction. Furthermore, the long range of the muon effectively increases the volume of the detector, since neutrinos can be detected even when the interaction occurs several kilometres outside the instrumented volume.

Air showers induced by interactions of cosmic rays with the Earth's atmosphere produce so-called atmospheric muons and neutrinos. The atmospheric muons can penetrate the atmosphere and up to several kilometres of sea water. Despite the overburden of 2 km of water, many atmospheric down-going muons will reach the detector. As is shown in figure 2.3, the flux of down-going atmospheric muons exceeds the muon flux due to neutrinos by six orders of magnitude. Up-going muons, on the other hand, can only be produced by interactions of (up-going) neutrinos. Therefore neutrino telescopes must be sensitive to up-going muons; i.e. neutrino telescopes are 'looking downward'. Most of the up-going muons are produced by atmospheric neutrinos that have traversed the Earth. These neutrinos form a largely irreducible background for the study of cosmic muon neutrinos.

A diffuse flux of high energy cosmic neutrinos, which may be the combined result of many unresolvable neutrino sources, could only be detected above the atmospheric neutrino background at very high energies, where the atmospheric neutrino flux is low due to the steep energy spectrum (see [38] for a recent study of the sensitivity of ANTARES

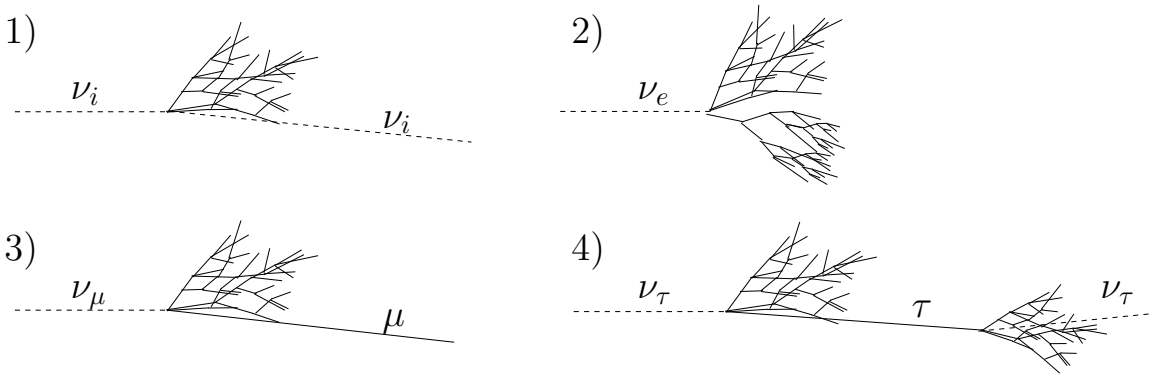

Figure 2.2: *Signatures of the event topologies occurring for different types of neutrino interactions. 1) Neutral current interaction producing only a hadronic shower. 2) Charged current (CC) interaction of a ν_e, initiating an electro-magnetic and a hadronic shower. 3) CC interaction of a ν_μ producing a long range muon. 4) CC interaction of a ν_τ, producing a τ that decays after some distance.*

to diffuse fluxes). On the other hand, individual astrophysical objects emitting sizable neutrino fluxes could show up above the background as an excess of neutrino events from a particular direction. The search for these 'point sources' is the subject of chapter 6 of this thesis. In contrast to diffuse neutrino fluxes, the detection of a point source will probably allow for immediate identification of the (type of) source object by correlating with other (e.g. optical or X-ray) observations.

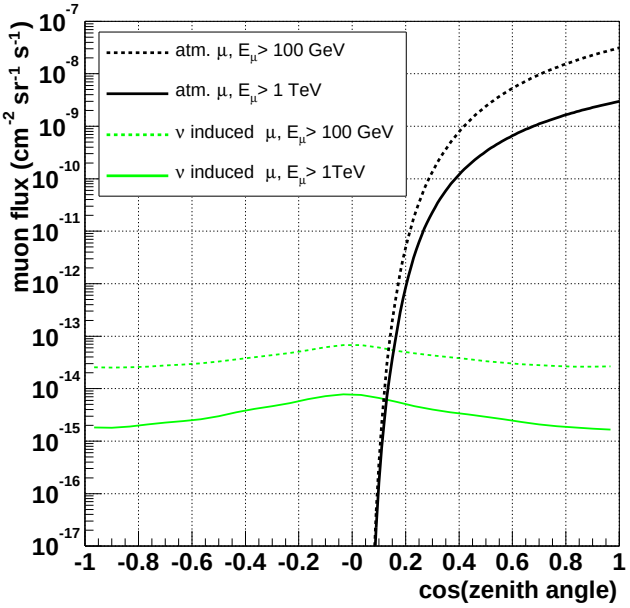

Figure 2.3: *Muon flux at 2.1 km depth due to atmospheric muons (from [39]) and to atmospheric neutrinos for two different thresholds on the muon energy (from [40]).*

2.1.2 Cherenkov radiation

Cherenkov radiation is emitted by particles that travel through a transparent medium with a velocity that exceeds the speed of light in the medium. The radiation is emitted at a characteristic angle with respect to the track. This angle is called the Cherenkov angle, θ_C and is given by

$$\theta_C = \arccos\left(\frac{1}{\beta n}\right), \tag{2.1}$$

where β is the velocity of the particle expressed as a fraction of the speed of light in vacuum, c, and n is the index of refraction of the medium. For highly relativistic particles ($\beta \approx 1$) in water, θ_C is about 42.5°.

The number of Cherenkov photons is given by [41]

$$\frac{dN_\gamma}{dxd\lambda} = \frac{2\pi\alpha}{\lambda^2}\left(1 - \frac{1}{\beta^2 n^2}\right), \tag{2.2}$$

where α is the finestructure constant, λ is the wavelength of the Cherenkov photon. This amounts to 3.5×10^4 photons emitted at wavelengths between 300 and 600 nm per metre of track

2.2 The ANTARES detector

ANTARES is an acronym for 'Astronomy with a Neutrino Telescope and Abyss environmental RESearch'. The ANTARES collaboration is building a neutrino telescope in the Mediterranean Sea, at a depth of 2.4 km. The detector site is located roughly 40 km off the coast of the south of France at a latitude of 42°50 (see figure 2.5). The schematic layout of the detector is shown in figure 2.4.

The basic building blocks of the detector are the Optical Modules (OMs). A schematic view and a photograph of an OM are shown in figure 2.6. Each OM consists of a pressure resistant glass sphere with a diameter of 43 cm, which houses a photomultiplier tube (PMT) and the electronics that provide the high voltage. The PMT is glued to one of the hemispheres with transparent silicone rubber gel. The other hemisphere is painted black and houses a 'penetrator' which provides the electrical connection between the inside and the outside of the OM. The photomultiplier tube selected for the ANTARES detector is the Hamamatsu R7081-20 which has a diameter of 10 inches and has 14 amplification stages. The timing resolution of the PMT is one of the key parameters that determine the angular resolution of the detector. It is determined by the spread in the transit time. This transit time spread (TTS) is about 1.3 ns (RMS) for this PMT. When optimally oriented, the projected area of the photocathode is 440 cm^2, which corresponds roughly to the diameter of 10 inches. A large part of the PMT is enclosed in a cage of high permeability metal (μ-metal), which serves to shield the Earth's magnetic field, thus optimising the uniformity of the PMT response. A detailed description of the ANTARES optical module and the assembly procedure is given in [42].

Three OMs are grouped together to form a 'floor', which is depicted in figure 2.8. The field of view of the OMs is oriented downwards, at an angle of 45 degrees with respect to

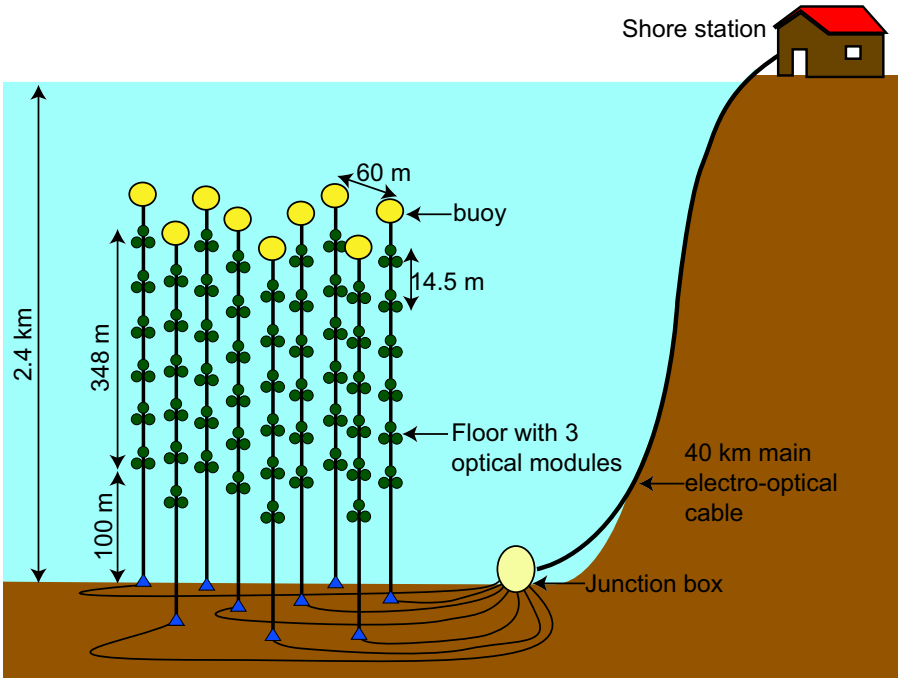

Figure 2.4: *Schematic layout of the ANTARES detector. Three optical modules, containing one PMT each, together with a local control module make up a 'floor'. Each string consists of 25 floors and is connected to the junction box. The data are sent to the shore, where they are processed by a computer farm situated in the shore station.*

the vertical. The OMs are fixed to a titanium structure, called the optical module frame, that provides the mechanical connection to the vertical cable. This structure also houses a container for the electronics, called the Local Control Module (LCM).

Five floors are grouped together to form a sector, which is a stand-alone unit as far as the power distribution and Data AcQuisition (DAQ) systems are concerned. Each sector contains a Master Local Control Module (MLCM), that collects the data produced in the floors of a sector and sends them to shore. A prototype sector has been built and operated in 2003. The obtained results will be discussed in section 2.4.

A full string will consist of five sectors (25 floors). The distance between two adjacent floors is 14.5 m. The bottom 100 m of a string is not instrumented to allow for the development of the Cherenkov cone. Located at the bottom of the string is the bottom string socket (BSS), which houses a dead weight, which keeps the string on the sea bed. To allow strings to be recuperated, they can be released from the BSS by issuing an acoustic command from a ship on the surface. The strings are held upright by a buoy located at the top.

The full detector will consist of 12 strings, which brings the total number of OMs to $3 \times 25 \times 12 = 900$. The position of the strings on the sea bed is shown in figure 2.7. Each string will be connected to a central junction box, which provides the connection to the 40 km long cable to the shore station located in the village of La Seyne-sur-Mer (see figure 2.5). This cable was deployed in October 2001 and the junction box was connected

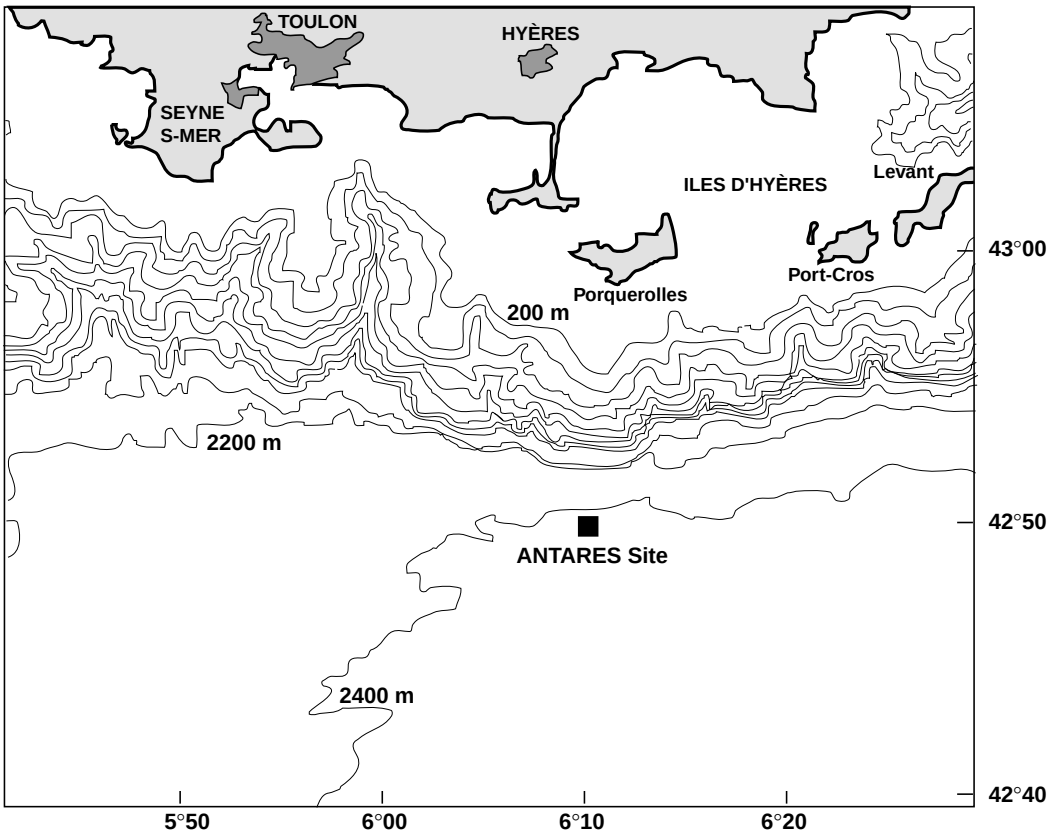

Figure 2.5: *Location of the ANTARES site. The distance to the south coast of France is roughly 40 km.*

to it in December 2002.

2.3 Data acquisition and calibration

As was mentioned earlier, each sector has an independent Data AcQuisition (DAQ) system. This is schematically depicted in figure 2.9. Various aspects of the DAQ system are discussed below.

2.3.1 Clock system

The reconstruction of muon tracks relies on accurate determination of the arrival times of the Cherenkov photons. The signals from the PMTs are time-stamped by the local electronics. For this, a (20 MHz) master clock signal is generated on the shore station and is distributed through an optical fibre network to local (slave) clocks in the LCMs.

Offsets between the local clocks are induced by differences in the optical path lengths involved in the distribution of the clock signal. In order to measure this optical path length, a calibration signal can be sent to an LCM which is then returned via the same optical path. From the delays between the sent and returned signals, the relative offsets

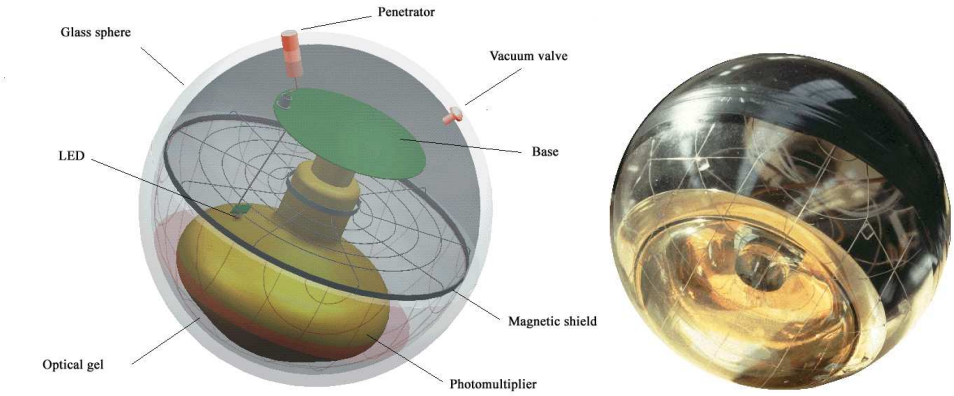

Figure 2.6: *Schematic view and a photograph of the optical module.*

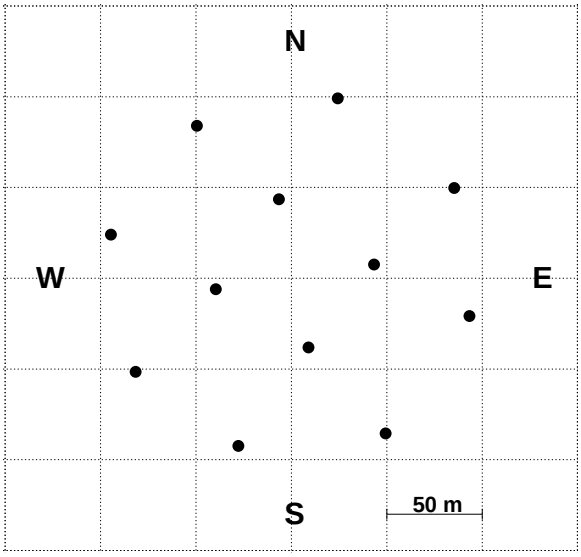

Figure 2.7: *Positions of the strings on the seabed.*

of the clocks in the LCMs are determined.

In order to correlate the data with other observations (e.g. from satellites detecting gamma rays bursts), an absolute timing accuracy of the order of a millisecond is required. This is realised by linking the master clock to the Global Positioning System (GPS).

2.3.2 Hit digitisation

A front-end chip, called the ARS (Analogue Ring Sampler) [43] is used to digitise the analogue PMT signal. The digitisation is triggered when the voltage crosses a certain threshold (typically the equivalent of 0.3 photo-electrons).

The ARS produces 'hits' by time-stamping the analogue signal and by integrating the current on the anode over a programmable time interval (25-80 ns). This yields an estimate of the charge, which can be related to the number of photo-electrons (p.e.). The time-stamp is provided by the local clock of the LCM. Sub-nanosecond precision is achieved by a time-to-voltage converter (TVC) that is used to interpolate between two subsequent clock pulses. The voltage provided by the TVC is digitised with an eight-bit

Figure 2.8: *Drawing of the optical module frame showing the three optical module spheres and the cylindrical container for the electronics. The (glass) cylinder at the top houses the optical beacon (see section 2.3.4). A hydrophone is visible on the left-bottom of the picture.*

analogue-to-digital converter. The maximal attainable timing resolution of the ARS is therefore $(20\text{MHz})^{-1} \times 256^{-1} \approx 0.2$ ns.

The ARS can sample a complete pulse on the PMT anode. To minimise the bandwidth requirements, this option is only triggered for pulses with large amplitudes or when the signal resembles a double pulse. The ARS decides autonomously whether one of these criteria is met. The pulses are sampled with a programmable frequency (up to 1 GHz). In this thesis, we assume that this 'waveform mode' is permanently disabled.

The digitisation procedure induces dead-time on the ARS. In order to reduce the effect of this dead time, each PMT is read out by two ARSs, which alternately digitise the analogue pulses.

2.3.3 Data transport and processing

The time and charge information of each hit is sent to the shore. This scheme eliminates the need for an off-shore trigger, but it requires a high bandwidth data link from the detector to the shore as the expected average count rate of about 70 kHz per PMT results

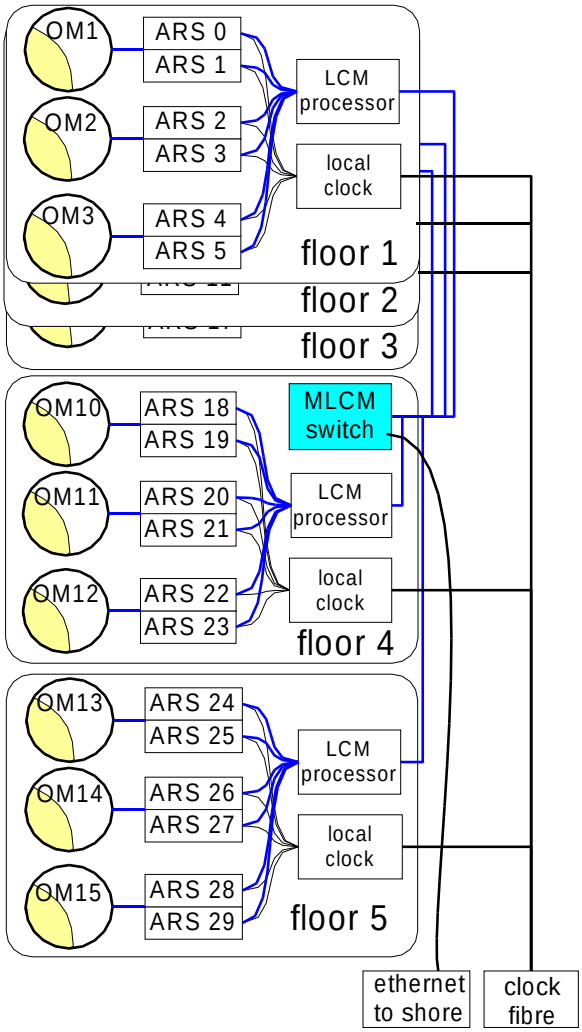

Figure 2.9: *Schematic drawing of the DAQ system of a sector. The signal path from the OMs to shore (and vice versa) is indicated. The analogue signals of the PMTs are digitised by the ARS chips, processed in the LCM and transmitted to shore via the MLCM. Also indicated is the clock system, which distributes a clock signal from the master clock on shore to the local (slave) clocks in the LCMs. The local clocks provide the time to the ARSs. The numbering scheme of the floors, OMs and ARSs will be used in section 2.4.*

in a data rate of about 625 Mb/s for each detector string.

The data produced by the ARS chips are formatted by the processor in the LCM and are then sent to the MLCM. From there, the data are transmitted to shore via a 1 Gb optical Ethernet link. On shore, the data are processed using a computer farm. Finally, the events found are written to disk for off-line analysis.

2.3.4 Calibration

Timing calibration

As explained in section 2.3.1, the relative delays between the slave clocks can be measured internally by the clock system. This measurement does not take into account the transit time of the PMT, which depends on the high voltage put on the PMT and which may change during the operation of the detector. The transit time can be measured by flashing a LED located inside the optical module (see figure 2.6) which illuminates the back of the photocathode. Since both the LED trigger and the resulting PMT signal are recorded by the ARS, the transit time can be determined directly.

In addition to the clock system and the LED calibration, there are two systems that

are intended for calibration of the whole system. For this, four floors per string will be equipped with an 'optical beacon'. This device consists of a set of pulsed LEDs which illuminate a number of OMs on neighbouring strings. The analysis of the resulting hit times provides the overall calibration of the PMT and the clock system. In addition there will be a similar system which employs a powerful pulsed laser located at the bottom of a string to illuminate a large part of the detector.

Position calibration

Since the optical modules are mounted on flexible strings, their positions and orientations are influenced by currents in the sea water and must therefore be monitored. The orientation of each optical module frame is measured by a compass and a tiltmeter located inside the LCM container. In addition, one in five floors will be equipped with a hydrophone which records acoustic signals from transmitters located at the bottom of the strings. Measurements of the propagation times of these signals can be used to determine the position of the hydrophones. Together, the measurements from the tiltmeters, compasses and the acoustic system provide a measurement of the relative position of the OMs with an accuracy of a few centimetres.

The absolute geographical position of the detector will be determined with an accuracy of a few metres during string deployment. The absolute orientation of the detector must be measured with an accuracy smaller than 0.1° (i.e. smaller than the expected pointing accuracy of the detector). This will be accomplished by a set of additional transponders. Their positions are measured with respect to the detector and with respect to a ship at the surface. The absolute position of the ship is determined using an on-board GPS system.

2.4 Sector line

In this section, the first results obtained with a prototype sector line are presented. Because the sector is the basic building block of a full string, the construction, deployment and operation of the sector line have been important tests of the hardware and operational methods. The first data were obtained while the sector line was located in a dark room in the laboratory. As will be shown in the next section, these data could be used to verify the timing accuracy of the detector. The sector line was then deployed at the ANTARES site in December 2002. The connection to the already deployed junction box, which provides the connection to the shore station via the main electro-optical cable, was made on March 17, 2003. Since then data were taken almost continuously until the recovery of the line on July 10, 2003, allowing a study of the optical background at the ANTARES site.

The DAQ and clock systems of the sector line are identical to those designed for the final detector. They were discussed in section 2.3. The convention we use in this section for numbering the floors, OMs and ARSs is given in figure 2.9.

2.5 Sector line dark room results

Figure 2.10: *Photograph of the sector line while it was located in the dark room. The OMs were covered with flower pots. The PMTs could be illuminated simultaneously by a light from a (common) laser that was distributed to the bottom of each flower pot through fibres of identical length.*

In order to verify the functioning of the PMTs and the DAQ system and to determine the timing accuracy, the sector line was tested in the laboratory prior to deployment. The

OMs were illuminated by a pulsed laser with a pulse width of about 100 ps. The light from the laser was distributed to the OMs through optical fibres of equal length, thus ensuring the simultaneous arrival of light at each OM. In order to avoid indirect illumination, the sensitive surfaces of the OMs were shielded by plastic pots, as is shown in figure 2.10. A diffuser at the bottom of the pots, ensured uniform illumination of a large fraction of the photocathode. Data were taken using the standard DAQ and clock systems. Below we describe how these data are used to calibrate the timing system and to determine the overall timing accuracy.

2.5.1 TVC calibration

The digitised hit times produced by the ARS consist of two components. The first component is the value of the 20 MHz clock, which is synchronised to the on-shore master clock. The second component consists of a one-byte value that is obtained by the digitisation of a time-to-voltage converter (TVC). The TVC value corresponds to an interpolation of the time between two consecutive clock ticks.

In order to minimise dead-time, each ARS chip is equipped with two TVCs. Each TVC must be calibrated individually. This calibration is performed using histograms of the output value U of the TVCs. An example of such a histogram is shown in figure 2.11a. As can be seen, only part of the full dynamic range of the TVCs is used. The minimal and maximal values of U differ per TVC, but the design ensures that each TVC maps a time domain of a full clock period, which was 50 ns during the test. The relation between TVC value U and hit time t is given by

$$t = \frac{(U - U_0)}{(U_{50} - U_0)} \times 50 \text{ ns} + C \tag{2.3}$$

where U_0 and U_{50} are the minimal and maximal values of the TVC respectively and C is an arbitrary constant.

Although the TVC output in figure 2.11 shows non-statistical fluctuations that are related to the digitisation process, the distribution is uniform on a scale of several bins. This is expected as the input signals of the TVC are uncorrelated with respect to the clock. The uniformity of the TVC output is illustrated in figure 2.11b, which shows the cumulative distribution, which is normalised to the known time interval of 50 ns. This distribution is well described by a straight line fit. From the line fit, the values of U_0 and U_{50} are obtained using equation 2.3. The deviation between the straight line fit and the cumulative distribution of the TVC values is shown in figure 2.11c. It shows that the slight non-linearity of the TVC induces errors of the order of 0.1 ns.

2.5.2 Time offsets

The clock signal is distributed to each floor using optical fibres of different length, which results in time offsets between the local clocks in the various floors (typically 120 ns between two adjacent floors). Furthermore there are differences in the delays associated with the transit time of the PMTs and the electronics. The relative offset of each ARS chip and the timing resolution can be determined using the laser calibration system.

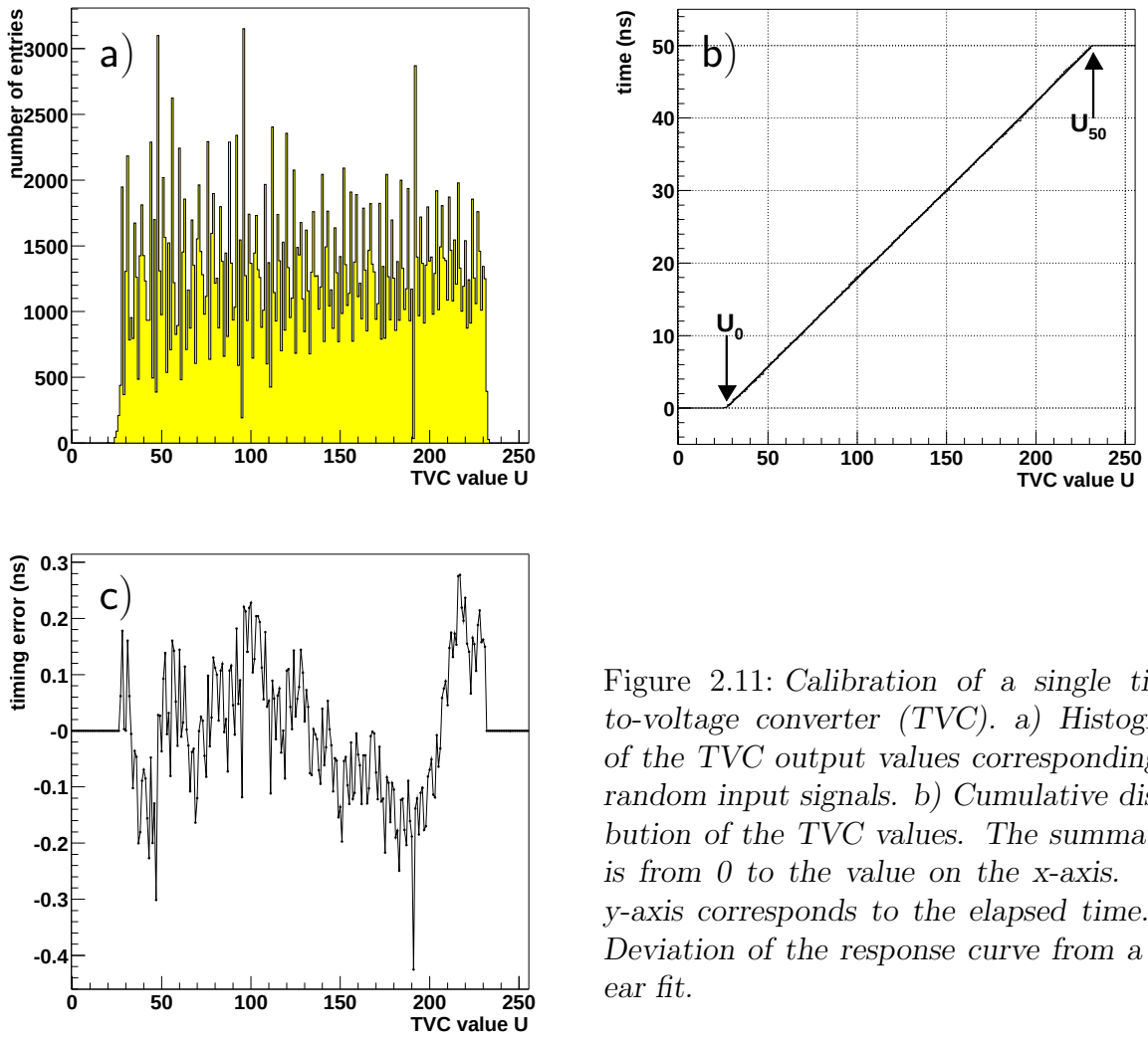

Figure 2.11: *Calibration of a single time-to-voltage converter (TVC). a) Histogram of the TVC output values corresponding to random input signals. b) Cumulative distribution of the TVC values. The summation is from 0 to the value on the x-axis. The y-axis corresponds to the elapsed time. c) Deviation of the response curve from a linear fit.*

In order to determine the relative offsets, the laser was flashed at a typical rate of 250 Hz. The distribution of the time differences between all pairs of hits occurring in a 13 ms time window on two ARS chips on different PMTs is shown in figure 2.12. In this plot, ARSs 1 and 6 are used, which are located on adjacent floors. The central peak ($\Delta t \approx 0$ ms) is caused by pairs of hits from the same laser flash. The other peaks are formed by pairs of hits that are caused by different laser flashes. The observed time difference between the peaks (4 ms) corresponds to the rate of the laser flashes (250 Hz). The offset between the two ARSs was obtained from the (fitted) mean of the central peak. In figure 2.13 the offsets of the ARSs with respect to a reference ARS (no. 0) are shown. As expected, the differences in the fibre lengths result in offsets of about 120 ns between adjacent floors. The differences in fibre length have also been measured using the internal calibration mechanism of the clock system (see section 2.3.1). The offsets that remain after correction for these delays are shown in figure 2.13b. They are of the order of a few nanoseconds. The strong correlation between offsets of ARSs connected to the same PMT suggests that these offsets could be largely due to differences in the transit time of

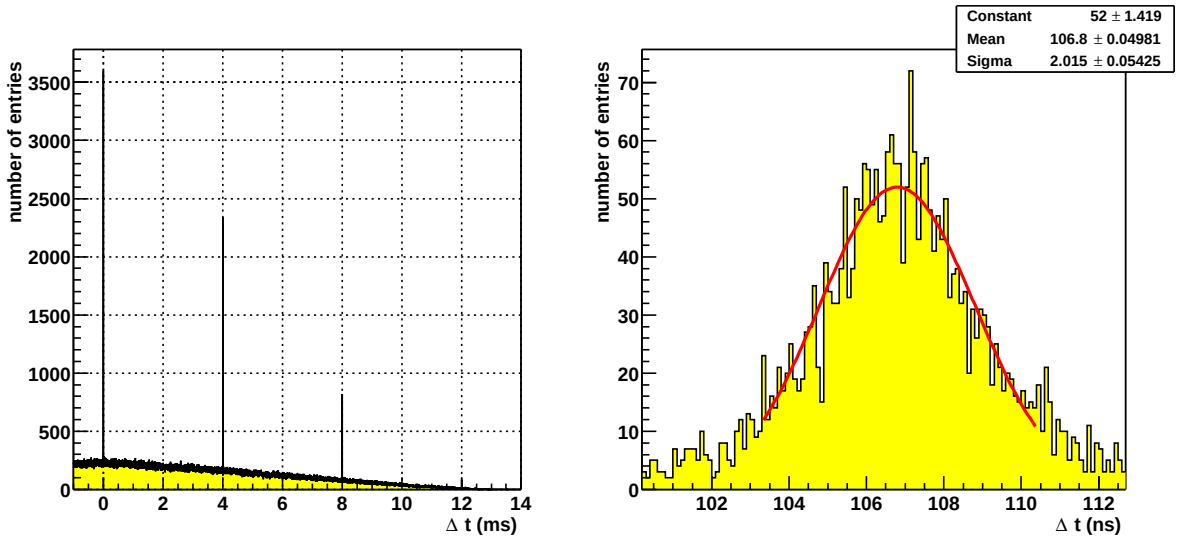

Figure 2.12: *Distribution of the time differences between hits as recorded before calibration. The right plot shows a close up of the peak at $\Delta t \approx 0$ ms and the fitted Gaussian function.*

the PMTs. Note that no data point is present for ARS 25; for unknown reasons, this chip has never functioned after the sector line was built.

2.5.3 Time resolution

Besides the time offsets in the system, the overall time resolution of a single ARS (including the PMT) can also be determined from the distributions of the time difference between pairs of ARSs. In this case, the width of the distributions is used. If the underlying response functions are Gaussian and uncorrelated, the width of such a distribution is a quadratic sum of the widths of the response functions. The resolution obtained with a particular ARS, σ_i, can then be estimated from the measured widths of the distributions of the time differences with two other ARSs which are labelled j and k:

$$\sigma_i^2 = \frac{1}{2}(\sigma_{ij}^2 + \sigma_{ik}^2 - \sigma_{jk}^2), \tag{2.4}$$

where σ_{ij} is the width of the distribution of the time differences between ARSs i and j. Equation 2.3 has been applied for several combinations of j and k. In the ideal case, the value of σ_i^2 should be independent of the choice of j and k. A small dependence has, however, been observed. The reason for this is that the response of the ARSs is not perfectly Gaussian. The spread in the obtained σ_i is interpreted as the uncertainty on the determination of the time resolution.

The time resolutions of the ARSs are shown in figure 2.14 for two different laser intensities. Unfortunately, no quantitative measurements of the laser intensity were made. The time resolution obtained with the low laser intensity is in reasonable agreement with the known TTS of 1.3 ns. The higher laser intensity yields a better time resolution,

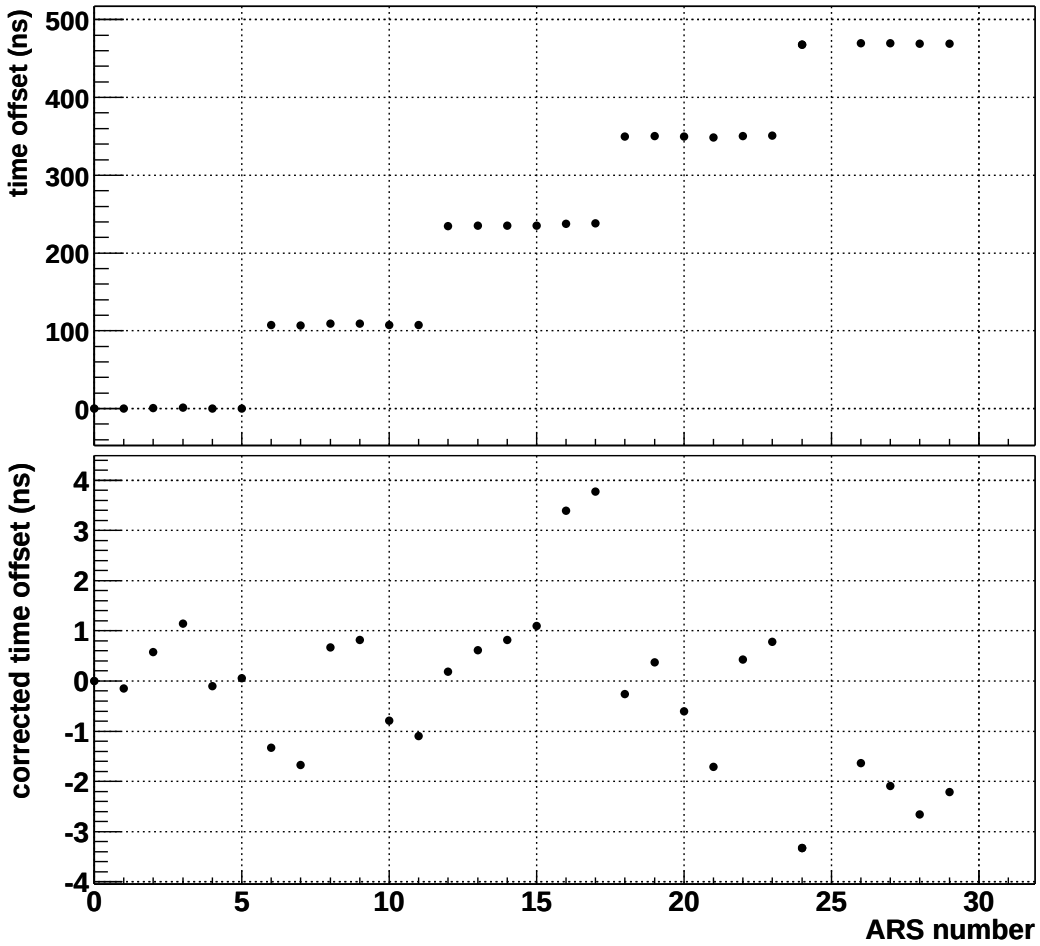

Figure 2.13: *Top: Time offset before calibration. Bottom: Time offset after correction for time delays of the local clocks determined with the clock system.*

which is expected because the TTS is decreased when multiple photons are detected simultaneously. This is because the transit time is effectively determined by the photo-electron with the smallest transit time. The spread in the arrival time of the first photo-electron decreases if the total number of photo-electrons increases. ARS 24 exhibits a much worse time resolution than all the others. The reason for this is not understood, but is likely to be related to the failure of ARS 25, which is connected to the same PMT.

It can be concluded that the time resolution achieved with the sector line in the dark room is in agreement with the 1.3 ns that was expected and which is used in the simulations in this thesis. In chapter 5 it will be shown that such a time resolution is sufficient to reconstruct the directions of muons with an accuracy of $\sim 0.2^{\circ}$.

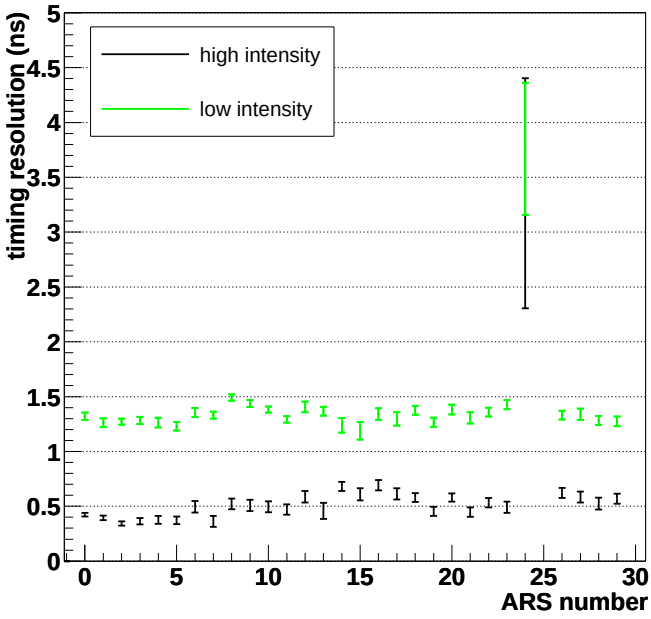

Figure 2.14: *Time resolution of the ARS chips in the sector line. Results are shown for two different values of the intensity of the laser used to produce the time correlated hits.*

2.6 Results from the deployed sector line

It was planned to measure atmospheric muons with the deployed prototype sector line. However, the accurate determination of the relative photon arrival times proved to be impossible due to a technical problem with the distribution of the reference clock signal. After recovery of the line, the cause of the problem was found to lie in a defect in the string cable. When the cable is immersed, the combined effect of the defect and the high pressure causes excessive optical attenuation in the fibre that was used for the distribution of the clock signal. A different cable design will be used in the future to prevent this problem.

The only measurements that were possible while the sector line was deployed were measurements of the intensity of the optical background. A typical time series of the background rate is shown in figure 2.15. The optical background consists of a 'baseline', which gives a continuous contribution to the count rate, and of bursts, which increase the count rate to up to several MHz over time-scales of the order of a second. The baseline is probably formed by a combination of light from decaying radioactive elements (^{40}K) in the sea water and a diffuse bioluminescence background. The 'bursts' are thought to be produced by organisms hitting parts of the detector, which stimulates them to emit light. There are both isolated bursts, seen by a single OM, as well as bursts that are seen by two or more OMs in the triplet. The former could be due to organisms hitting the OM itself, while the latter are probably due to collisions with the vertical cable. Also inter-floor correlations are sometimes observed.

Overall, the data can be summarised by two quantities: the baseline rate, which is defined as the median of the recorded count rate in a 15 minutes interval, and the burst fraction, which is defined as the fraction of time the count rate exceeds the baseline rate by more than 20%. These two quantities were monitored over almost the full data taking period. The results are shown in figure 2.16. Both the baseline and the burst fraction show some long periods of increased activity.

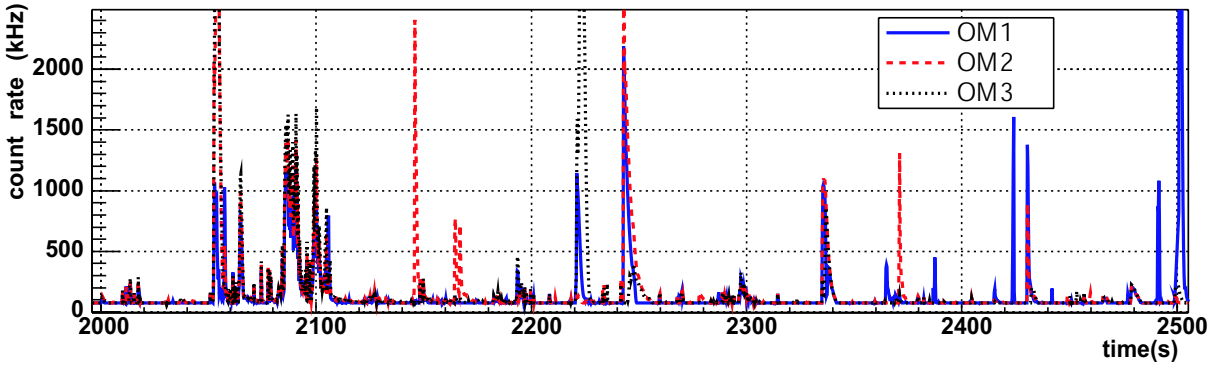

Figure 2.15: *The count rate recorded by the OMs on one of the floors as a function of time.*

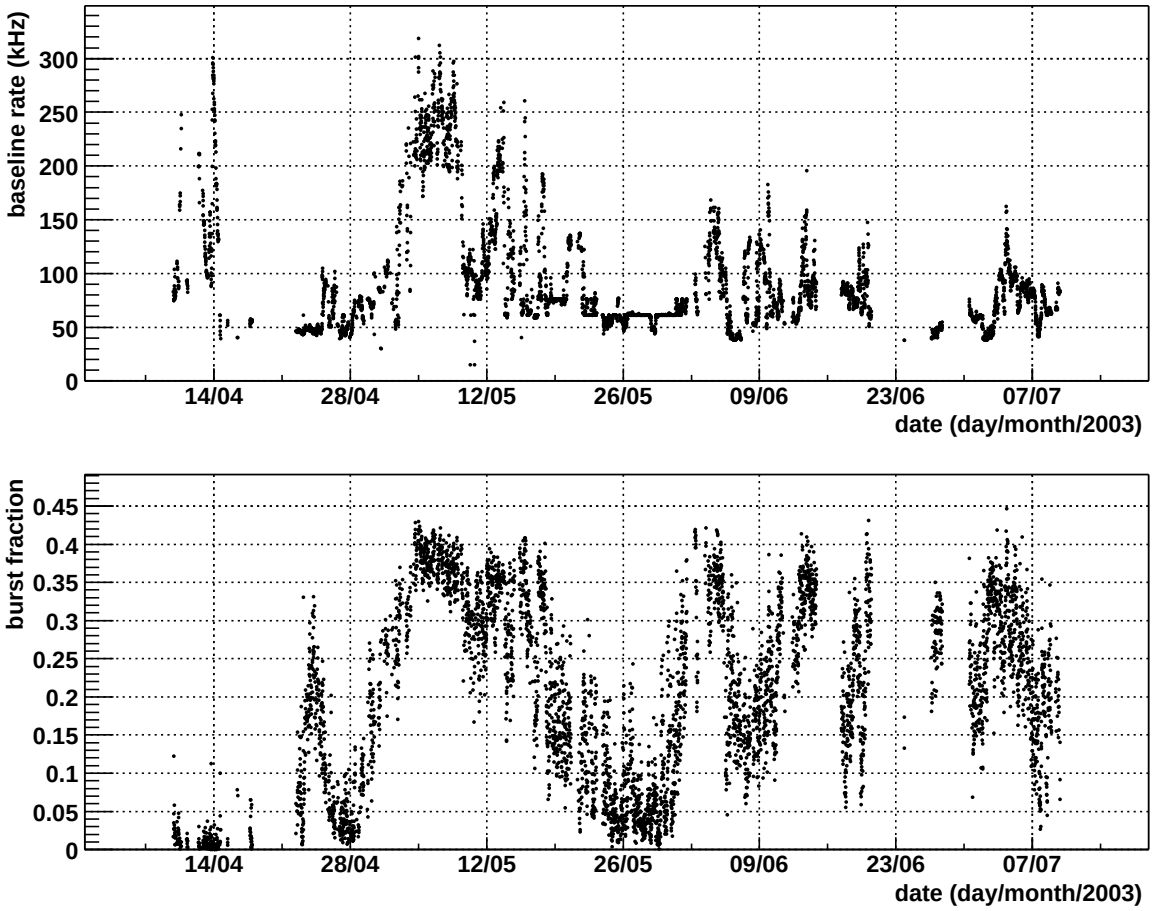

Figure 2.16: *The baseline rate and the burst fraction as a function of time.*

2.7 Epilogue

While it had been foreseen that down-going muons would be reconstructed with the prototype sector line, this was not possible due to technical problems. However, the count rate could be measured, allowing a study of the optical background at the ANTARES site. It turns out that this background is often higher than previously expected. For the simulations in this thesis, a constant background rate of 60kHz was assumed, which now appears to be optimistic for a large fraction of the data-taking time. The implications of the higher background on the physics potential of the detector remain to be studied in detail.

The preceding measurements in the laboratory have shown that the time resolution obtained with the total system is roughly 1.3 ns, in accordance with expectations.

At the moment of writing, it seems likely that the collaboration will decide to fix the problems that have come to light during immersion and to re-deploy the sector line in 2004. It is planned that the full detector will be completed in 2006.

Chapter 3

Physics and detector simulation

In this chapter the tools that are used to simulate the neutrino interactions and the response of the detector are described.

High energy muons can travel up to tens of kilometres in rock or water before they are stopped. Muons from charged current neutrino-nucleon interactions occurring far from the detector can thus still be detected. In order to evaluate the acceptance of the detector, neutrino interactions must therefore be generated in a large volume surrounding the detector (see figure 3.1). On the other hand, the emission of Cherenkov light and the production of secondary particle showers need to be simulated only when the particles are close to the detector. The simulation of Cherenkov light and the development of hadronic or electro-magnetic showers is therefore restricted to a smaller volume, called the 'can'. This can is a cylindrical volume that encompasses the detector with a margin of a few times the attenuation length of light, so that Cherenkov light from particles outside the can does not need to be simulated.

Generating the neutrino interactions and propagating the muons to the can is the purpose of the event generator GENHEN. Aspects of the event generation are discussed in section 3.2. The simulation of the Cherenkov light and the detector response is performed by two detector simulation packages, KM3 and GEASIM, which are described in section 3.3. In section 3.1 it is discussed how the generated events can be weighted with a prediction for a neutrino flux in order to calculate an expected event rate.

3.1 Monte Carlo scheme and event weighting

In this section the event weighting method used in ANTARES is explained by calculating the rate of detectable muon events for an assumed neutrino flux.

The total rate of detected events originating from neutrino interactions occurring in a geometric volume V is given by the following integral:

$$R = \int P_{\oplus}(E, \vec{d})\ \sigma(E)\ \rho(x) N_A\ \frac{d\Phi(E, \vec{d})}{dE d\Omega}\ P^{\mathrm{det}}(\vec{x}, \vec{d}, E)\ d\vec{x} d\Omega dE, \tag{3.1}$$

where the following quantities have been introduced:

$\vec{x}$: the position of the neutrino interaction

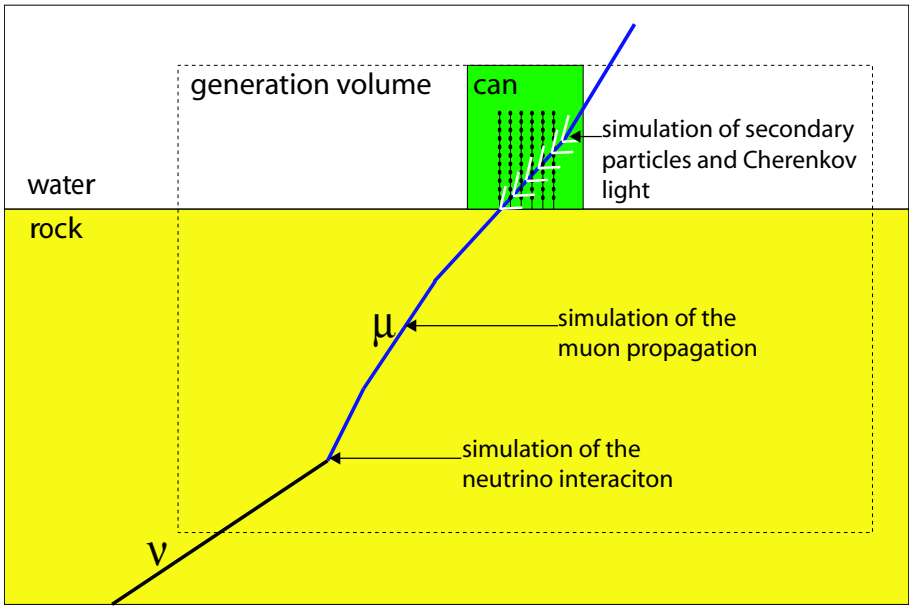

Figure 3.1: *Overview of the simulation scheme: neutrino interactions are generated in a large (tens of kilometres) volume. The resulting muons are propagated to the can; only inside the so-called can, the Cherenkov light and the detector response are simulated.*

$\vec{d}$: the direction of the neutrino

$\frac{d\Phi(E,\vec{d})}{dEd\Omega}$: the differential neutrino flux, i.e. the number of neutrinos per unit energy (E), solid angle (Ω), area and time. This is the flux of neutrinos before they enter the Earth.

$\rho(x)N_A$: the number of target nucleons per unit volume, given by the density ρ times Avogadro's number N_A,

$\sigma(E)$: the total charged current neutrino-nucleon cross-section (see section 3.2.1),

$P_{\oplus}(E,\vec{d})$: the probability of a neutrino of energy E to traverse the Earth without undergoing an interaction (see section 3.2.2) and

$P^{\text{det}}(\vec{x},\vec{d},E)$: the probability to detect and reconstruct the event.

The detection probability $P^{\text{det}}(\vec{x},\vec{d},E)$ depends on the following:

- the energy and direction of the muon produced at the interaction vertex, which are determined by the kinematics of the neutrino interaction (see section 3.2.1)
- the probability that the muon reaches the detector and its direction and energy when it does so (see section 3.2.3)
- the characteristics of the detectable light produced by the muon and the response of the detector (see section 3.3)

- reconstruction and selection algorithms (see chapters 4 and 5).

A detailed evaluation of $P^{\text{det}}(\vec{x}, \vec{d}, E)$ is only feasible by means of a simulation. We will therefore evaluate integrals like equation 3.1 by means of Monte Carlo integration (see e.g. [44]), which means that the integral is approximated by evaluating the integrand at a number of randomly chosen points in the overall phase space. An integral over a function $f(x, y)$ can, for example, be approximated by

$$\int_{x_1}^{x_2} \int_{y_1}^{y_2} f(x,y)dxdy \approx \frac{(x_2 - x_1)(y_2 - y_1)}{N_{\text{gen}}} \sum_{i=1}^{N_{\text{gen}}} f(x_i, y_i), \tag{3.2}$$

where the x_i and y_i are random numbers, uniformly distributed in the intervals $[x_1, x_2]$ and $[y_1, y_2]$ respectively. In the context of simulations, each set of these random numbers is called a (simulated) 'event'. This two-dimensional example generalises in a straightforward way to every dimension.

To calculate the integral of equation 3.1, random variables $\vec{d}_i$, $\vec{x}_i$ and E_i are generated for the neutrino direction, the position of the interaction and the energy of the neutrino respectively. In addition, P_i^{det} is determined for each event; i.e. for each event, the neutrino interaction, muon propagation, detector response and reconstruction are simulated[1]. The value of P_i^{det} is either 1 or 0 depending on whether the event is detected, reconstructed and selected in the final analysis or not.

The direction of the neutrinos is generated uniformly in the cosine of the zenith angle θ in the range $[\theta_{\text{min}}, \theta_{\text{max}}]$ and in the azimuth angle in the range $[0, 2\pi]$. In contrast, the energy of the interacting neutrinos is not generated uniformly in E but according to a simple power law spectrum: $\frac{dN_{\text{gen}}}{dE} \propto E^{-\alpha}$, where α typically has a value of 1.4. This is done in order to ensure that roughly equal numbers of events are simulated for each energy decade. In order to apply equation 3.2 to the integral of equation 3.1, the latter has been rewritten:

$$R = \int P_{\oplus}(E, \vec{d})\ \sigma(E)\ \rho(\vec{x}) N_A\ \frac{d\Phi(E, \vec{d})}{dEd\Omega}\ E^{\alpha}\ d\frac{1}{1-\alpha} E^{1-\alpha}\ d\vec{x} d\cos(\theta) d\phi \tag{3.3}$$

Now, the integral can be evaluated by Monte Carlo integration,

$$R = \frac{\Delta}{N_{\text{gen}}(1-\alpha)} \sum_{i=1}^{N_{\text{gen}}} P_{\oplus}(E_i, \vec{d}_i)\ \sigma(E_i)\ \rho(\vec{x}_i) N_A\ \frac{d\Phi(E, \vec{d})}{dEd\Omega}\ P_i^{\text{det}}\ E_i^{\alpha}, \tag{3.4}$$

where the value for E_i is drawn from a distribution in which $E^{1-\alpha}$ is uniformly distributed (i.e. $\frac{dN}{dE} \propto E^{-\alpha}$). Δ is known as the phase space of the generation:

$$\Delta = 2\pi\ V \times (\cos\theta_{\text{max}} - \cos\theta_{\text{min}}) \times (E_{\text{max}}^{1-\alpha} - E_{\text{min}}^{1-\alpha}). \tag{3.5}$$

To (re)calculate the event rate for any given neutrino flux it suffices to keep track of the 'generation weight' of each event, which is defined as

$$w_i = \Delta \frac{1}{1-\alpha} E_i^{\alpha}\ \sigma(E_i)\ \rho N_A\ P_i^{\text{det}}\ P_{\oplus}(E_i, \vec{d}_i). \tag{3.6}$$

[1] In this simulation many more random numbers are generated (e.g. the kinematic variables of the neutrino interaction). Since these variables are not used explicitly in the event weights, they are omitted here.

The rate of detected events resulting from a flux Φ can then be calculated as follows:

$$R = \frac{1}{N}\sum_{i=1}^{N} w_i \frac{d\Phi(E_i, \vec{d_i})}{dEd\Omega}. \tag{3.7}$$

In the special case where all neutrinos originate from a point-like astrophysical source, the direction of the neutrinos is uniquely determined, but varies with time t due to the rotation of the Earth. In this case the integral in equation 3.1 reduces to an integral over $\vec{x}$ and E. Equation 3.4 then becomes

$$R(t) = \frac{\Delta^\bullet}{N(1-\alpha)} \sum_{i=1}^{N_{\text{gen}}} P_\oplus(E_i, \vec{d_i})\sigma(E_i)\rho(\vec{x_i})N_A P_i^{\text{det}} \frac{d\Phi(E_i, t_i)}{dE} E_i^\alpha, \tag{3.8}$$

where $\frac{d\Phi(E,t)}{dE}$ is the differential flux from the point source, and

$$\Delta^\bullet = V(E_{\text{max}}^{1-\alpha} - E_{\text{min}}^{1-\alpha}). \tag{3.9}$$

A specialised 'point source mode' has been included in the event generation software to simulate events from point sources.

3.2 Event generation

Neutrino induced events are generated using the GENHEN package, which is described in detail in [45]. The purpose of this program is to generate all particles that could generate detectable light. A large number of neutrino interactions (typically a few times 10^{10}) is generated in a cylinder surrounding the detector. This cylinder is typically 25 km in radius and height in order to ensure that all interactions that could lead to a muon in the detector are simulated. This size is determined from the maximal muon range (see section 3.2.3) that is associated with the highest neutrino energy that is generated (typically $E_\nu^{\text{max}} = 10^7$ GeV). The GENHEN program simulates the neutrino interaction and the propagation of the muon to the can. Cuts are made on the muon energy and direction in order to avoid full simulation of events with a negligible probability of producing a muon on the can.

Interactions of neutrinos and anti-neutrinos are generated separately and are weighted with the corresponding fluxes. For models of cosmic neutrinos, the two fluxes are usually assumed to be equal.

3.2.1 Neutrino interactions

In general, two types of neutrino interactions are generated:

Quasi elastic and resonant scattering. Interactions such as $\nu_\mu + n \to \mu^- + p$ (quasi-elastic) and $\nu_\mu + p \to \mu^- + \Delta^{++}$ (resonant) give a small contribution to the total cross-section (about 10% for $E \gtrsim 10$ GeV and less than 1% for $E > 500$GeV). They are simulated with the RESQUE package [46].

Charged current deep inelastic scattering. Charged Current (CC) Deep Inelastic Scattering (DIS) events are generated with the LEPTO [47] package, which provides sampling of the first order double differential charged current cross-section to obtain the characteristics of the outgoing muon and the struck quark. The subsequent hadronisation is modelled by the Lund string model, which is implemented in LEPTO via calls to PYTHIA 5.7 and JETSET 7.4 [48]

Since the DIS process dominates the observed event rate, the corresponding cross-sections are discussed below.

Deep inelastic scattering cross-section

In the simulation, it is assumed that the target consists of an equal amount of protons (p) and neutrons (n). The combination $N \equiv \frac{1}{2}(n+p)$ is referred to as an isoscalar nucleon.

The leading order double differential cross-section of the DIS charged current process $\nu_\mu + N \rightarrow \mu^- + X$ can be expressed as

$$\frac{d^2\sigma}{dxdy} = \frac{2G_F^2 ME}{\pi}\Big(\frac{M_W^2}{Q^2+M_W^2}\Big)^2[xq(x,Q^2)+(1-y)^2 x\bar{q}(x,Q^2)], \tag{3.10}$$

where x, y and Q^2 are the kinematic variables characterising the kinematics of the process (see e.g. [49]): y is the inelasticity $y = (E-E_\mu)/E$, the scaling variable x is defined as $x = Q^2/2M(E-E_\mu)$ and $-Q^2$ is the invariant square of the momentum transfered between the neutrino and the outgoing muon, and $x = Q^2/2M(E-E_\mu)$. Furthermore, G_F is the Fermi coupling constant, M is the mass of the target nucleon, E is the energy of the incident neutrino and M_W is the mass of the W boson. The distribution function $q(x,Q^2)$ contains contributions from the down (d), strange (s) and bottom (b) quarks in the nucleon N, i.e

$$q = \frac{1}{2}(d_p + s_p + b_p + d_n + s_n + b_n), \tag{3.11}$$

where e.g. s_p denotes the density of strange quarks (s) in the proton (p). In the same way, the anti-quark distribution $\bar{q}(x,Q^2)$ can be expressed as

$$\bar{q} = \frac{1}{2}(\bar{u}_p + \bar{c}_p + \bar{u}_n + \bar{c}_n), \tag{3.12}$$

where c refers to the charm quark and where the contribution from top quarks has been neglected.

Under the assumption of isospin symmetry, the quark densities in the neutron are related to those in the proton: $u_n = d_p$, $\bar{u}_n = \bar{d}_p$. It is furthermore assumed that the sea quark distributions in the neutron and proton are equal. As a result, q and $\bar{q}$ can be expressed entirely in terms of quark density functions in the proton:

$$q = \frac{1}{2}(d_p + u_p + 2s_p + 2b_p) \tag{3.13}$$

$$\bar{q} = \frac{1}{2}(\bar{d}_p + \bar{u}_p + 2c_p). \tag{3.14}$$

The cross-section for anti-neutrino scattering is obtained from equation 3.10 after interchanging the above quark and anti-quark distributions q and $\bar{q}$.

Parameterisations of the quark distributions are extracted from fits to data from experiments. Here, the most recent fit obtained by the CTEQ collaboration, called CTEQ6D[2] [50] is used. Figure 3.2 shows the cross-section for neutrinos obtained by integration of (3.10) with the CTEQ6D parameterisations of the quark density function and with the older versions CTEQ5D and CTEQ3D. The latter is in agreement (to the level of $\sim 1\%$) with published values [51], which have been obtained using CTEQ3D and which are also shown in figure 3.2. This figure also shows the cross-section obtained from the LEPTO package using the CTEQ6 parameterisations. This cross-section, which is actually used in the simulation, is smaller than the cross-section obtained from direct integration of equation 3.10. At low energies the difference may be due to a cut on the invariant mass of the hadronic final state which is implemented in LEPTO. At high energies the discrepancy is due to the fact that the cross-section used by LEPTO does not take into account scattering off b quarks. It is not trivial to modify LEPTO to include the contribution from b quarks, since for a large part of the kinematic phase space the reaction is suppressed due to the large mass of the top quark. This effect is taken into account in the direct integration of equation 3.10 by using the 'slow-rescaling' prescription [52], as was done in [51]. The LEPTO package was thus not modified, with an underestimation of the cross-section (up to 10% at $E = 10^8$ GeV) as a result.

At neutrino energies $E \gtrsim 10^8$ GeV there is a significant contribution to the cross-section from scattering off quarks at very small values of x ($x \lesssim 10^{-6}$). In this regime, the quark densities are poorly constrained by measurements and there are dramatic differences between the different versions of the CTEQ routines. This results in a large discrepancy between the CTEQ3 and CTEQ5 results: at $E = 10^{12}$ GeV, the cross-section differs by about an order of magnitude. This difference could be interpreted as a kind of systematic uncertainty on the cross-section due to the unknown behaviour of the quark densities at low x. However, it is expected that the behaviour of the CTEQ3 and CTEQ6 parameterisations is more correct than that of CTEQ5, since in the latter, the quark densities essentially vanish in the low-x regime. As can be seen in the figure, the LEPTO package fails to integrate the cross-section for energies above 10^9GeV.

The CTEQ6 parameterisations of the quark densities have error estimates associated with them which allows for a calculation of the uncertainty of the neutrino-nucleon cross-section stemming from the uncertainty of the quark density functions. This uncertainty turns out to be of the order of a few percent in the energy range $10 - 10^8$ GeV. This is shown in figure 3.2(right).

Composition of the interaction medium

As mentioned above, the interactions are generated for a target nucleus consisting of an equal amount of protons and neutrons. This is a valid assumption if the interaction occurs in the rock ('standard rock' [53] has atomic mass $A = 22$, atomic number $Z = 11$ and density $\rho = 2.65$ g cm^{-3}). However, for water ($A = 18,\ Z = 10,\ \rho = 1.04$ g cm^{-3}) this is

[2] The 6 is a 'version number' and the D refers to the factorisation scheme that was used while performing the fits: in this case the so called DIS-scheme.

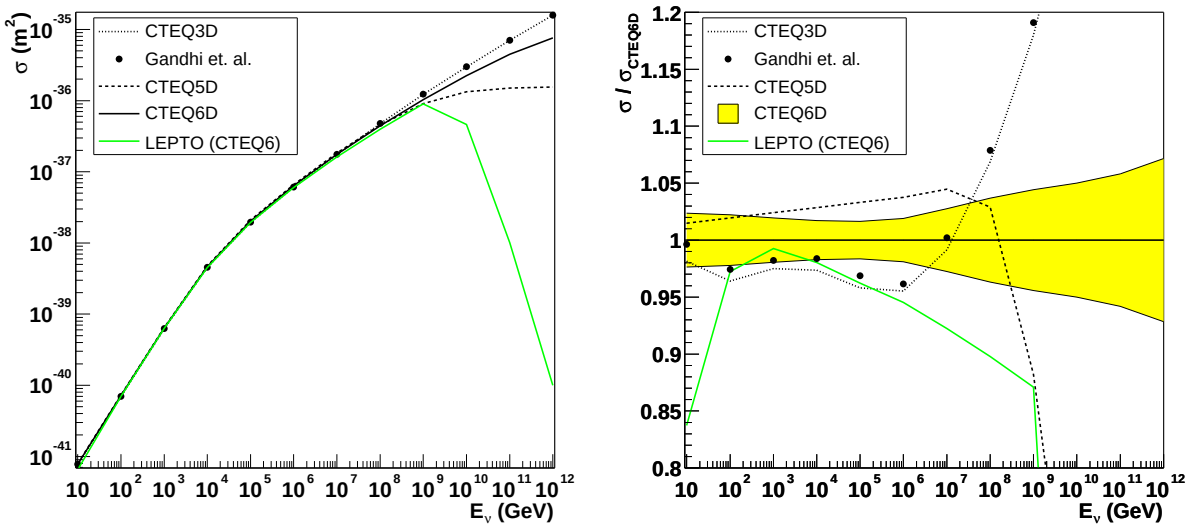

Figure 3.2: *Left: Cross-sections of the charged current DIS process* $\nu_\mu + N \rightarrow \mu^- + X$ *obtained by integration of equation 3.10 using the* CTEQ*3,* CTEQ*5 and* CTEQ*6 parameterisations of the quark density distributions. Also shown are points taken from [51] which were calculated with* CTEQ*3. The cross-section calculated by the* LEPTO *package using* CTEQ*6 is also shown. Right: The same results normalised to the* CTEQ*6 result. The uncertainty on the* CTEQ*6 result due to uncertainty of the quark density functions is indicated by the filled area.*

not the case. The average cross-section for scattering on a water nucleon can be written as

$$\sigma_{\mathrm{H_2O}} = \sigma_N + \frac{1}{18}(\sigma_p - \sigma_n). \tag{3.15}$$

In the low energy DIS regime, $\frac{\sigma_p}{\sigma_n} \approx \frac{1}{2}(2)$ for (anti-)neutrinos and the error is of the order of $\frac{1}{18} \times \frac{2}{3} \approx 4\%$. At high energies the error is smaller, since the difference between σ_n and σ_p decreases as the contribution from sea quarks becomes more important. Hence, the non-isoscalarity of the interaction medium can be neglected.

3.2.2 Neutrino absorption in the Earth

Neutrinos with energies above a TeV have a non-negligible probability to undergo a charged current interaction in the Earth before reaching the vicinity of the detector. The Earth is therefore opaque to very high energy neutrinos.

The amount of matter Σ that the neutrino encounters while traversing the Earth was taken from [51]; it is shown in figure 3.3 as a function of the zenith angle θ. The column density seen by neutrinos with $\theta > 145°$ is enhanced due to the increased density of the Earth's core. The probability that the neutrino survives its journey through the Earth, $P_\oplus$, is given by

$$P_\oplus(E, \theta) = e^{-\Sigma(\theta) N_A \sigma(E)} \tag{3.16}$$

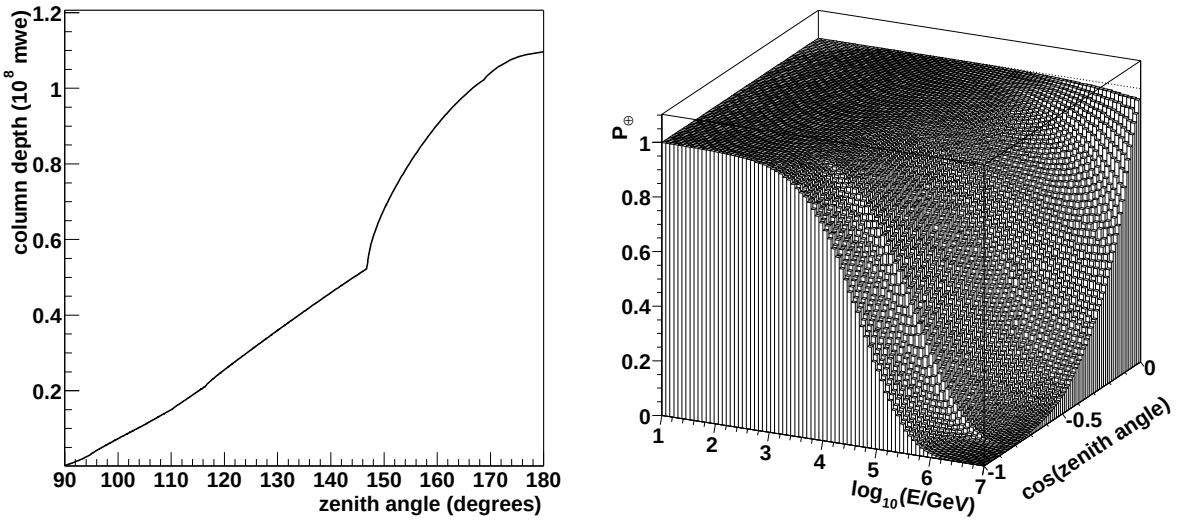

Figure 3.3: *Left: The density of the Earth, integrated over the path of the neutrino as a function of the direction of the neutrino expressed in water equivalent metres. The kink in the figure is caused by the density discontinuity associated with the boundary of the Earth's core. Right: The probability of a neutrino to traverse the Earth without undergoing an interaction as a function of the direction (zenith angle) of the neutrino and its energy.*

and is shown in figure 3.3(right) as a function of the energy and zenith angle of the neutrino. As was mentioned in section 3.1, this probability is taken into account in the calculation of the expected event rate.

Neutral Current (NC) interactions of neutrinos in the Earth will result in a decrease in energy and a deviation from the original direction. At the relevant energies, the NC cross-section is about a factor 2 smaller than the CC cross-section. A rough estimate of the fraction of neutrinos undergoing a NC interaction but not a CC one, yields 15% at most. This effect has been neglected.

3.2.3 Muon propagation

While travelling from the interaction point to the detector, the muon loses energy. Furthermore its direction is affected by multiple Coulomb scattering. The propagation of the muon through rock and sea water must therefore be simulated. For this, the MUSIC [54] package was used, which provides both simulation of the energy loss and of multiple scattering[3]. In the following, the physics processes included in the MUSIC code and the relevant results are described.

[3]There exist other muon propagation codes, like the PROPMU package, which includes multiple scattering, but has inaccuracies in the treatment of the energy loss. This package was used only for the propagation of atmospheric muons from sea level to the detector (see section 3.5.2) because it executes more quickly than MUSIC.

Energy loss

The muon can lose energy via the following processes:

1. **ionisation:** Atoms in the medium are ionised. The energy transfer to the electrons is usually modest, but occasionally the electrons obtain a non-negligible fraction of the muon energy. Such electrons are called 'knock-on electrons' (or δ-rays).

2. **bremsstrahlung:** In the nuclear electric field, the muon radiates off a photon.

3. **pair production:** An e^+e^- pair is produced.

4. **photonuclear interactions:** A virtual photon is exchanged with a nucleus.

The average energy loss per unit length as implemented in the MUSIC software is shown in figure 3.4 for each of these processes. Below about a TeV ionisation is the dominant energy loss mechanism and the energy loss is roughly constant at about 0.3 GeV/m. At high energies, pair production and bremsstrahlung are the dominating processes. For these processes, the energy loss is roughly proportional to the energy of the muon. Distributions of the muon range (i.e. the distance the muon can travel before it is stopped) are shown in figure 3.5 for various values of the initial muon energy.

Angular deviation

Deviations of the direction of the muon are predominantly caused by multiple Coulomb scattering off atomic nuclei. However, the processes responsible for the energy loss described above can also deflect the muon. Both effects are taken into account in MUSIC. As is shown in figure 3.6, for the majority of the events, the scattering angle between the neutrino and the initial muon is about an order of magnitude larger than the angle caused by multiple scattering of the muon itself. In conclusion, multiple scattering gives a small contribution to the angular resolution, but is nevertheless simulated.

3.3 Detector simulation

In this section the simulation of the detector response to particles is described. As explained before, this simulation is only done for particles inside the can volume. The production of Cherenkov light is simulated for the muon itself and secondary particles that may be produced. The propagation of Cherenkov light is also simulated. The two programs used are called KM3 and GEASIM.

The GEASIM package uses GEANT3 [55] to perform full tracking of all particles through the detector volume. For each particle, the arrival time of the Cherenkov light incident on the OMs is calculated analytically. The number of Cherenkov photons is calculated taking into account the attenuation of the light. A drawback of GEASIM is that scattering of the Cherenkov light is not simulated. Furthermore, the full particle tracking results in long execution times especially for the simulation of high energy muons, which produce large secondary showers.

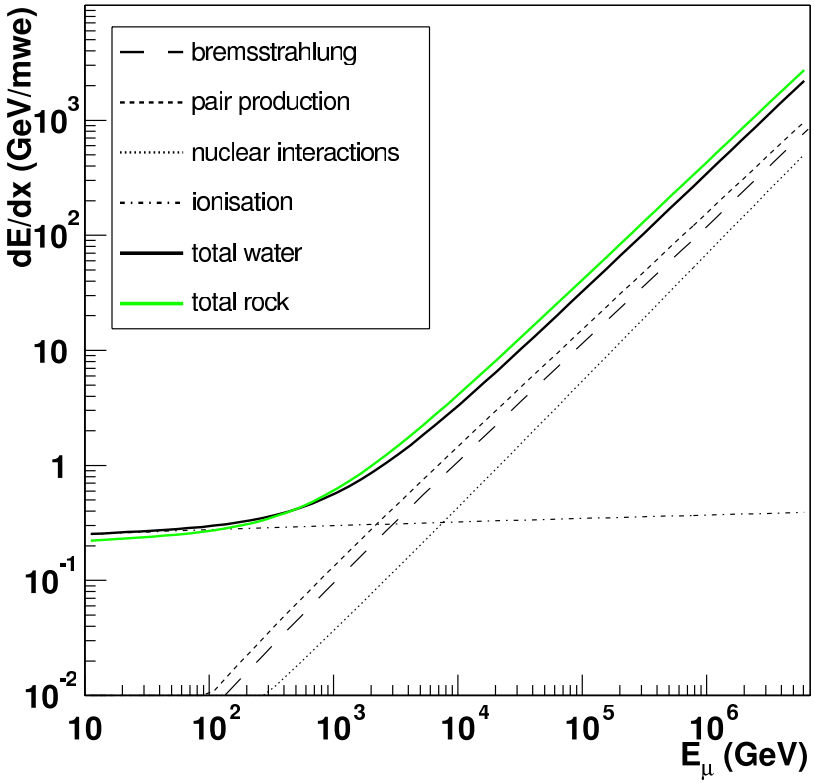

Figure 3.4: *Average energy loss per water equivalent metre for muons in rock and sea water as a function of the muon energy. For the energy loss in water, the contributions of the different processes are shown separately. The data for this figure were taken from the* MUSIC *code.*

The KM3 program uses a modified version of the MUSIC package to propagate the muon through the detector. This propagation is done in one metre steps. If the energy loss of the muon over this distance exceeds a critical value (0.3 GeV), an Electro-Magnetic (EM) shower is initiated at a random position on the path. In order to provide a fast simulation of the shower development and light scattering, the photons are sampled from tables containing the average photon fields produced by the muon or by EM showers. These tables are obtained beforehand from a full simulation (using GEANT3) of a large number of muons and EM showers. In this simulation, the Cherenkov photons are individually tracked through the water, including the effects of light scattering. A drawback of the KM3 package is that there are no facilities to simulate hadronic showers.

In order to obtain a realistic estimate of the angular resolution of the detector, it is important that light scattering is included for the simulation. Therefore, KM3 was used for the simulation of the light produced by the muon and by secondary particles. The hadrons produced in the neutrino interaction have to be simulated in the (relatively rare) case that the interaction takes place near the instrumented volume (i.e. in the can). In this case, the hadronic shower is simulated using GEASIM.

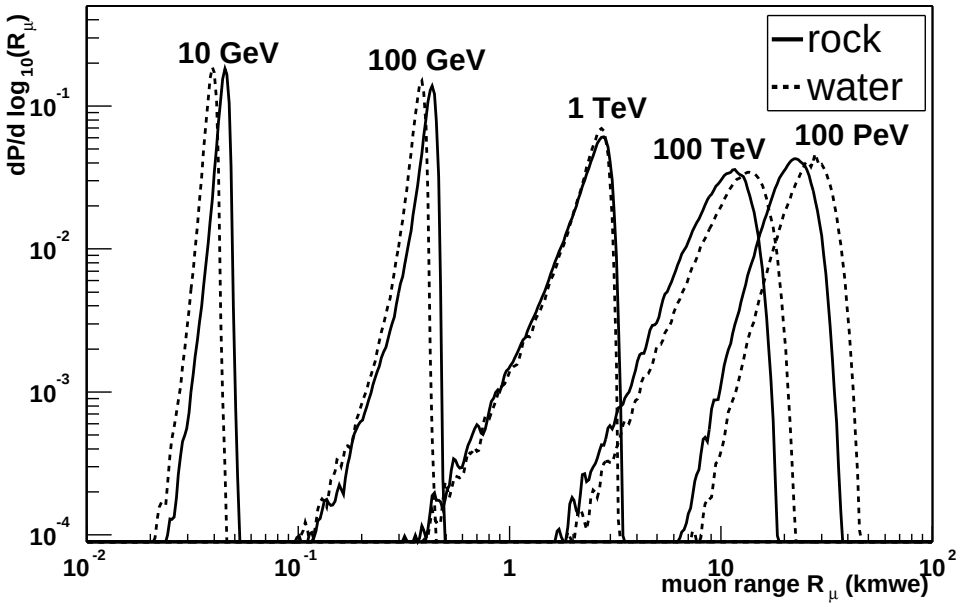

Figure 3.5: *Distribution of the muon range in rock and water for different muon energies expressed in water equivalent km.*

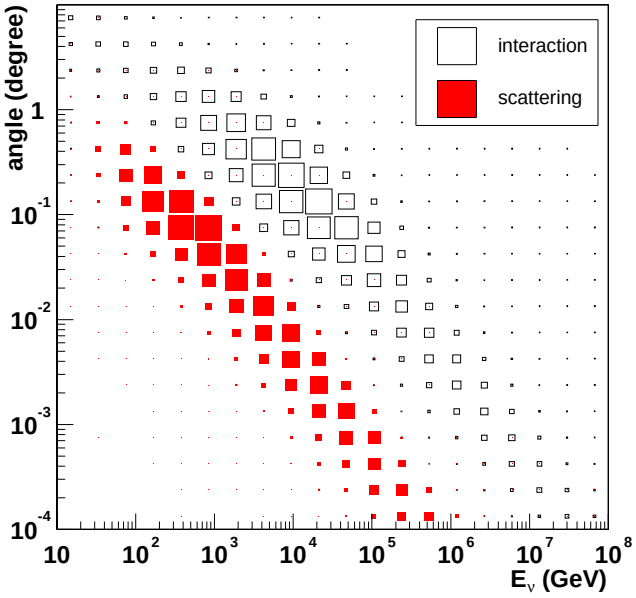

Figure 3.6: *Angle between the neutrino and the produced muon (interaction) and the angle between the muon at the interaction vertex and the muon entering the can, which is due to multiple scattering.*

The simulations of the optical modules, the PMT response and the front-end electronics are identical in both packages. They are described in section 3.3.2. The following section describes the simulation of the generation of the Cherenkov light and its propagation through the sea water as is implemented in KM3.

3.3.1 Cherenkov light

The number of Cherenkov photons as a function of the wavelength is given by equation 2.2 and the angle with respect to the muon track, θ_C is given by equation 2.1. These expressions are used in the simulation of the light produced by the muon itself and the charged particles in the hadronic or electro-magnetic showers. The simulation of the light emitted by charged particles is fairly simple. The propagation of the light to the OM is more complicated and is discussed in the next sections.

Absorption and scattering

The influence of absorption and scattering of light is taken into account by a model that has been tuned to data acquired during measurements at the ANTARES site [56]. In these measurements a short (10 ns) light pulse was used to illuminate an OM which was located at a distance of either 24 or 44 metres from the light source. The absorption and scattering parameters have been determined, respectively, from the relative intensities and the arrival time of the light.

The absorption length could be determined with good accuracy: the errors are typically smaller than 1 m. However, in various measurements taken at different times of the year, different values were obtained. The interpretation is that the medium exhibits genuine variations. Figure 3.7(left) shows the measurements and the model of the wavelength dependence of the absorption length that is used in the simulation. The shape of this distribution was taken from [57], while the normalisation was adjusted to match the measurements. At short distances from the muon track, the average absorption length can be computed by weighting this distribution with the λ^{-2} spectrum of the Cherenkov light, which yields an absorption length of 22 m. At larger distances from the muon the absorption length will effectively increase, up to 55 m, since photons with short absorption lengths have already been absorbed.

Scattering of light can be described by a scattering length (i.e. the mean distance between two scatterings) and a distribution of the angle between the initial and final direction of the photon at each scattering. For the angular distributions, two cases were considered:

- **Scattering off molecules.** This is described by Rayleigh scattering, which has a known distribution of the scattering angle.
- **Scattering off sedimentary particles (and perhaps microscopic organisms).** For this type of scattering, the distribution of the scattering angle has been measured.

The corresponding distributions of the scattering angle are shown in figure 3.8. Both are taken from [58]. The data were fitted using a combination of the two cases: each scattering

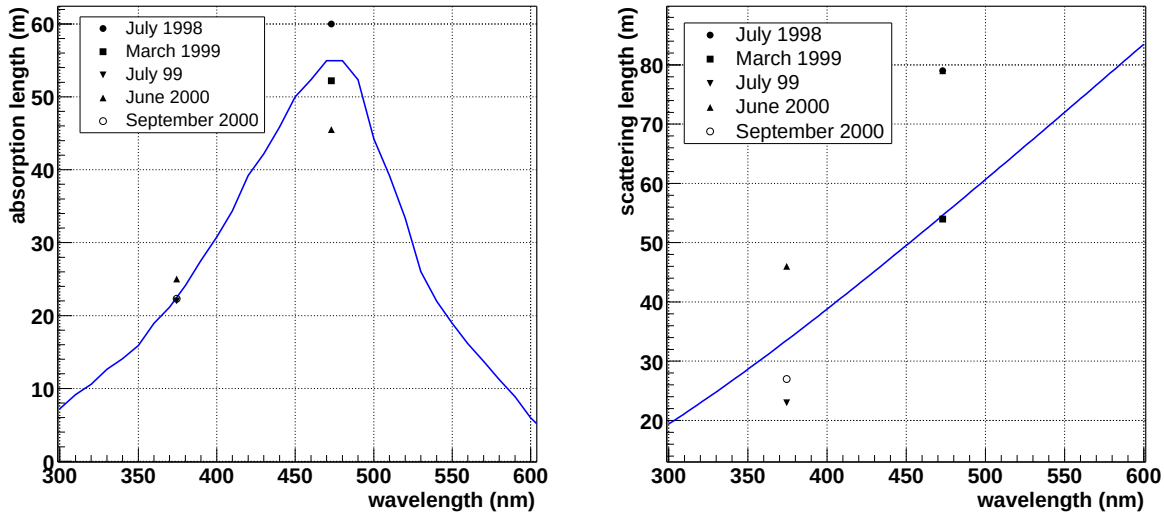

Figure 3.7: *The absorption length (left) and scattering length (right) as used in the simulation as a function of the wavelength. The measurements taken at the ANTARES site are also shown.*

has a probability η of being a Rayleigh scattering and a probability $1-\eta$ of being a 'particle' type scattering. The values for η and the scattering length were fitted simultaneously to the data. Since the particle scattering is strongly peaked in the forward direction, it has relatively little influence on the time distribution of the arriving light. As a result, the contribution of particle scattering could not be accurately determined. The most important effect of the scattering for the reconstruction of muon tracks is the influence of the time delay of the light. This can be expected to be well reproduced. The reason for this is that the scattering parameters have been extracted from the measurements of exactly this quantity.

Light velocity and dispersion

The relevant velocity for the propagation of the Cherenkov light is the group velocity v_g, as was pointed out only relatively recently [59]. The group velocity of light is defined as

$$v_g = \frac{d\omega}{dk} = -\lambda^2 \frac{d\nu}{d\lambda} \tag{3.17}$$

where $\omega = 2\pi\nu$ and $k = 2\pi/\lambda$ (λ and ν are respectively the wavelength and frequency of the light). Using the standard dispersion relation, this can be expressed in terms of the phase velocity $v_p \equiv (c/n)$

$$v_g = v_p \cdot \left(1 + \frac{\lambda}{n}\frac{dn}{d\lambda}\right), \tag{3.18}$$

where n is the index of refraction of the medium.

An empirical model to describe the behaviour of the refractive index in sea water was adopted from [60], with additional correction for the pressure of 1.4×10^{-5} bar^{-1} [61].

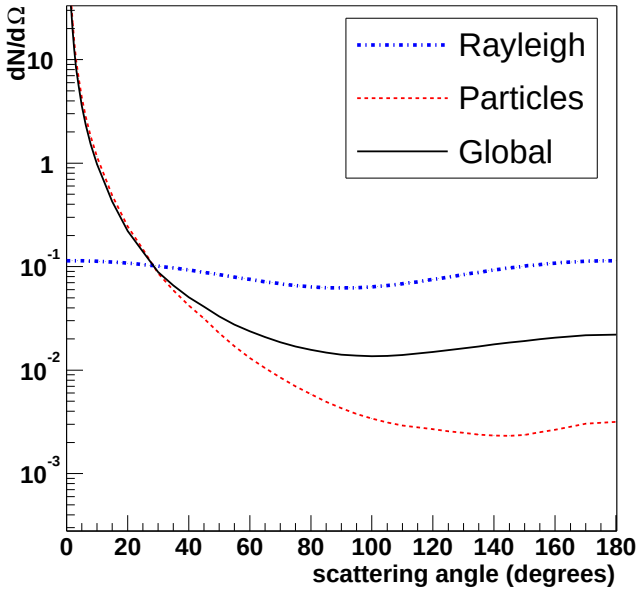

Figure 3.8: *The distribution of the scattering angle for Rayleigh scattering and the scattering off particles (both from [58]). Also shown is the distribution (Global) used in the simulation, which is a weighted average of the two.*

The phase and group velocities from this model are shown in figure 3.9. The velocity has also been measured at the ANTARES site [56]. The model agrees well with the measured value at λ =460 nm, but disagrees at λ = 370 nm. The origin of this discrepancy is not understood.

The wavelength dependence of the speed of light induces a spread in the arrival times of the Cherenkov photons on the PMT. This effect is called dispersion. In the simulation programs (both KM3 and GEASIM), the speed of light is taken to be constant (as the group velocity at 460 nm), but dispersion is taken into account afterwards by sampling tables of the relative delays induced by dispersion. These tables have been obtained in a dedicated study [45], which used the model from [60] with the pressure correction. The distribution of the relative delays as a function of the distance travelled by the light is shown in figure 3.9(right).

It may be noted that the somewhat weaker (compared to the model) wavelength dependence of the group velocity that is suggested by the data would result in less dispersion than the model used in the simulation.

3.3.2 Simulation of the hardware

The response of the optical module to the Cherenkov photons is simulated by taking into account the quantum efficiency of the PMT, the transparency of the glass sphere and the optical gel and the effective area of the photocathode. All these effects are a function of the wavelength. The efficiency of the OM is also dependent on its orientation with respect to the direction of the photons. Figure 3.10(left) shows the quantum efficiency for both the bare PMT and the PMT enclosed in the glass sphere. Figure 3.10(right) shows the angular dependence of the efficiency of the total optical module[4].

[4]By convention, an angle of incidence of 180° means the photon hits the PMT head-on, while 0° means it hits the (insensitive) rear of the OM.

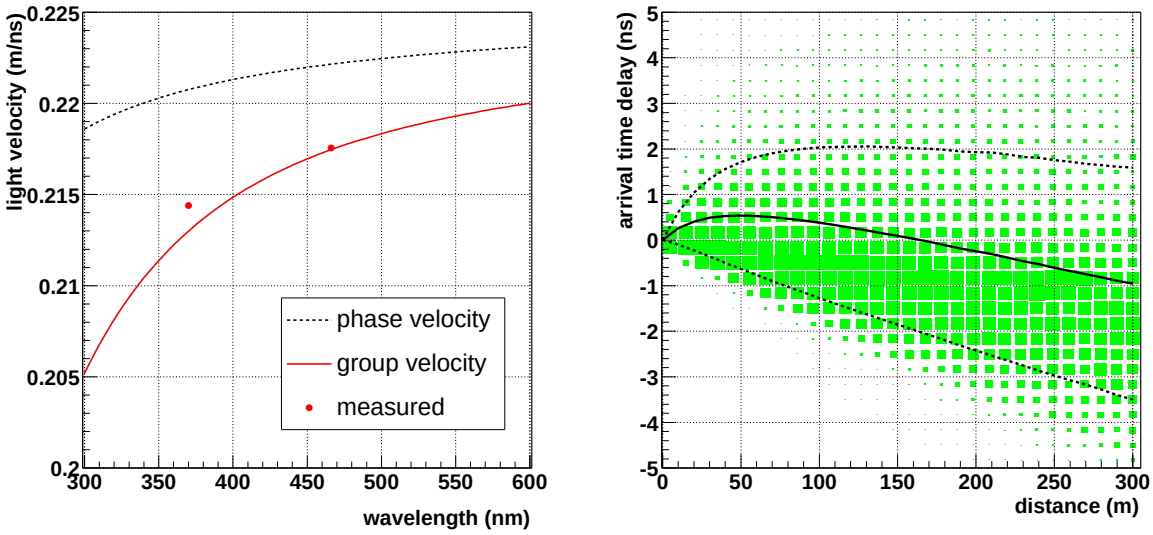

Figure 3.9: *Left: Phase velocity of light according to the model of Quan and Fry and the group velocity derived from it. Also indicated are direct measurements at the ANTARES site. The statistical uncertainty on the measurements is smaller than the size of the dots. Right: Distribution of the delay in arrival time due to dispersion for hits from dispersed light (with respect to hits travelling at the group velocity at 460 nm) as a function of the distance travelled by the light. The lines indicate the central value and the RMS.*

The front-end ARS chip integrates the analogue signal from the PMT over a typical time window of 25 ns. This is simulated by summing the number of detected photons in that window. After the integration, the ARS cannot take data for about 250 ns. A second ARS, connected to the same PMT, digitises signals arriving afterwards. The time resolution for single photo-electron signals is 1.3 ns (see section 2.5.3) and decreases for higher amplitudes. To simulate this the hit times are smeared using a Gaussian function with a width $\sigma = 1.3 \text{ ns}/\sqrt{N_\gamma}$, where N_γ is the number of simultaneously detected photons.

The amplitude measurement is simulated by smearing the integrated number of photons with an empirical function. This function results in a (roughly Gaussian) smearing of about 30%. The dynamic range of the charge integration corresponds with a signal of about 20 photo-electrons. This effect is not included in the simulation.

3.4 Light detection

Using the detector simulation discussed in the previous section, some important characteristics of the detected light can be evaluated.

The first quantity of interest is the number of photons that is detected by an OM. This is shown in figure 3.11 as a function of the distance travelled by the photon for different values of the muon energy E_μ. As expected, the number of detected photons increases approximately linearly with the muon energy in the energy range above 1 TeV. At $E_\mu \simeq 1$ TeV, the contribution of the light from the muon accounts for about 50% of the total light

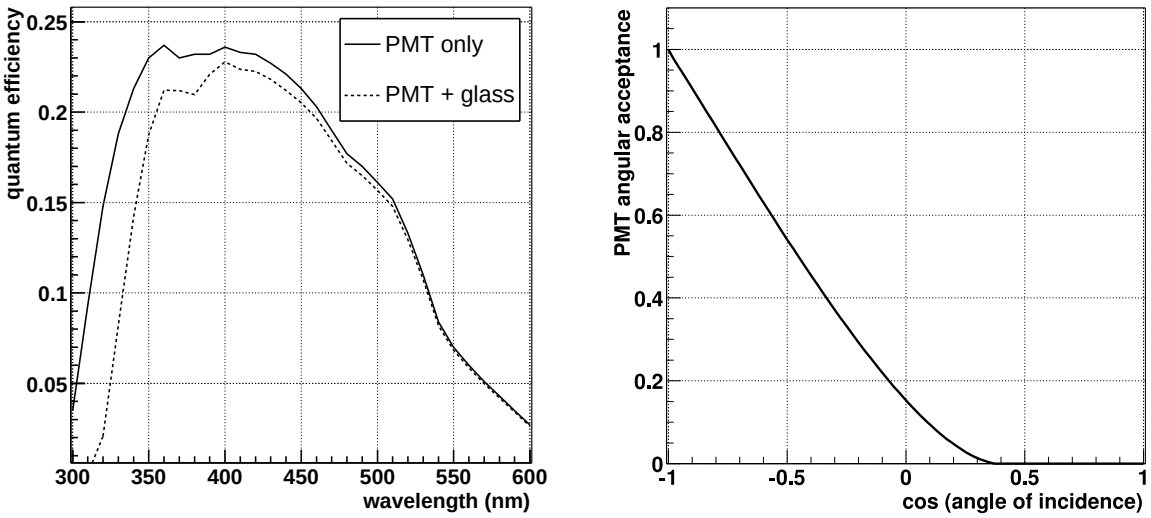

Figure 3.10: *Left: The quantum efficiency as a function of the wavelength for the bare PMT and for the PMT enclosed in the glass sphere. Right: The dependence of the acceptance on the angle of incidence of the photon on the optical module.*

production. The number of observed photons can be approximated by

$$N(b) = N_{1m}\frac{1}{b}e^{-b/\lambda_{\text{eff}}^{\text{abs}}}, \tag{3.19}$$

where b is the photon path length and $\lambda_{\text{eff}}^{\text{abs}}$ is the effective absorption length. A reasonable agreement with the distribution due to the muon alone is found for a value of $\lambda_{\text{eff}}^{\text{abs}} = 38$ m. The number of detected photons due to the muon alone 1 metre away from the muon track N_{1m} is about 100. Equation 3.19 is plotted in figure 3.11 and is in good agreement with the full simulation.

The time information obtained from the PMT signals is of crucial importance for the reconstruction of muons. The arrival time of the photons is expressed relative to the expected arrival time t^{th} that can be calculated from the parameters of the muon track, as will be explained in section 4.1. The distribution of the resulting time residuals $r = t - t^{th}$ is shown in figure 3.12 for a muon with an energy of 1 TeV. The contributions from the muon itself and the secondary electrons are shown separately for both scattered and unscattered photons. Photons originating from the muon and arriving at the OM without scattering carry the most precise timing information: their arrival time is only perturbed by dispersion and the TTS of the PMT and hence the residual distribution is sharply peaked at $r = 0$. Photons that originate from secondary electrons or that have scattered, are often delayed with respect to this time. However, also for these photons the distribution peaks at $r \approx 0$, which means that such photons can still be used in the reconstruction process. The distribution for background photons corresponds to a background rate of 60 kHz (see section 3.5.1).

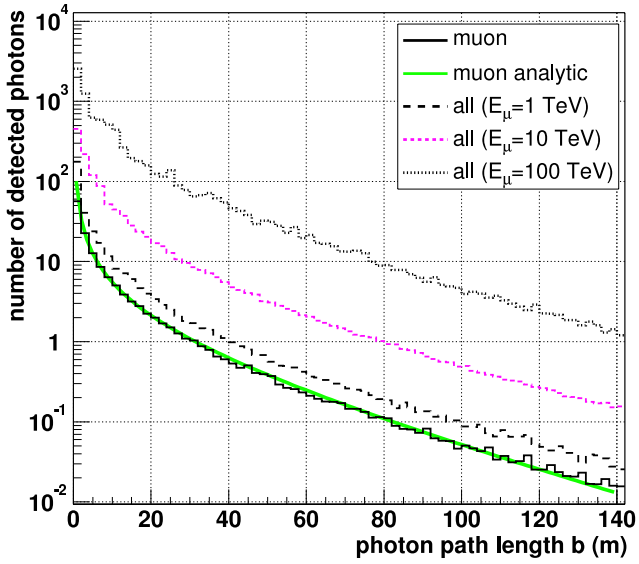

Figure 3.11: *Number of photons detected by an optimally oriented OM as a function of the photon path length for different muon energies. The contribution from Cherenkov light produced by the muon alone is shown separately. The result of equation 3.19 is also shown (muon analytic).*

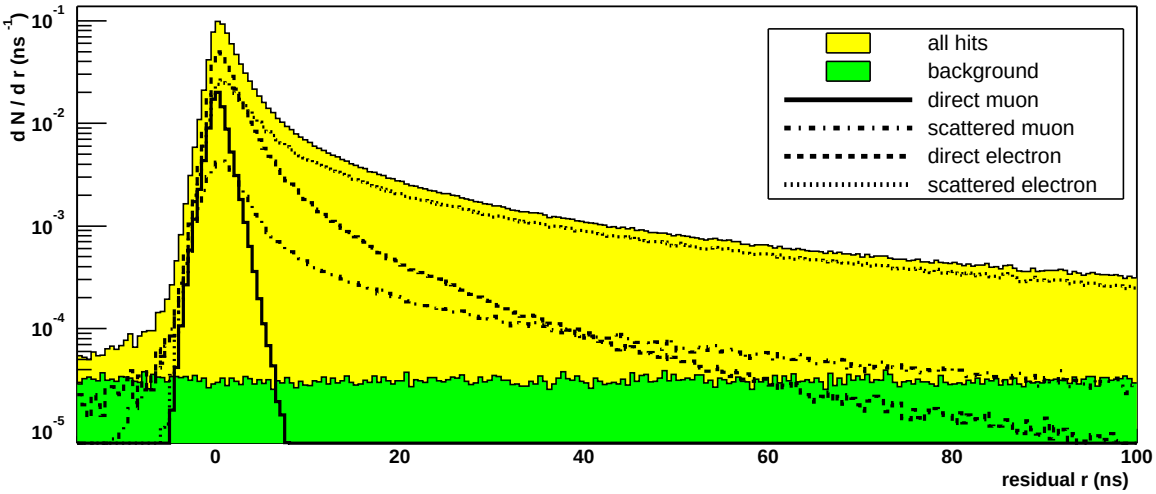

Figure 3.12: *Distribution the time residuals for photon arrival times relative to the direct muon signal. Contributions are shown for scattered and unscattered photons originating from the muon itself and from secondary electrons and positrons. All hits occurring within a distance of 100 m from the track are included in this figure.*

3.4.1 Effect of the front-end electronics

As explained in section 3.3.2 the PMT signal is integrated over a period of 25 ns. Due to the integration, arrival times of photons separated by less than 25 ns can not be observed. Instead, these signals are combined to give hits with larger amplitudes. The time of the resulting hit corresponds to the time of the first photon.

The effect of the electronics on the hit times is illustrated in figure 3.13(left), which shows the hit time residuals. Due to the charge integration, the region between the main

peak and 25 ns is depleted. An increase in the amount of detected photons can be seen at residuals just above 25 ns. Note also, that for large amplitude hits, the main peak is shifted slightly to the left. This is because the time of the hit corresponds to the time of the first photon, which arrives, on average, earlier if the number of photons is large.

The number of hits of a given amplitude as a function of the photon path length is shown in figure 3.13(right). When the OM is close to the track, the average number of photo-electrons is significantly larger than one (see figure 3.11). Hence the hits will predominantly consist of large amplitude hits. At distances larger than 15 m, most hits are due to single photo-electrons.

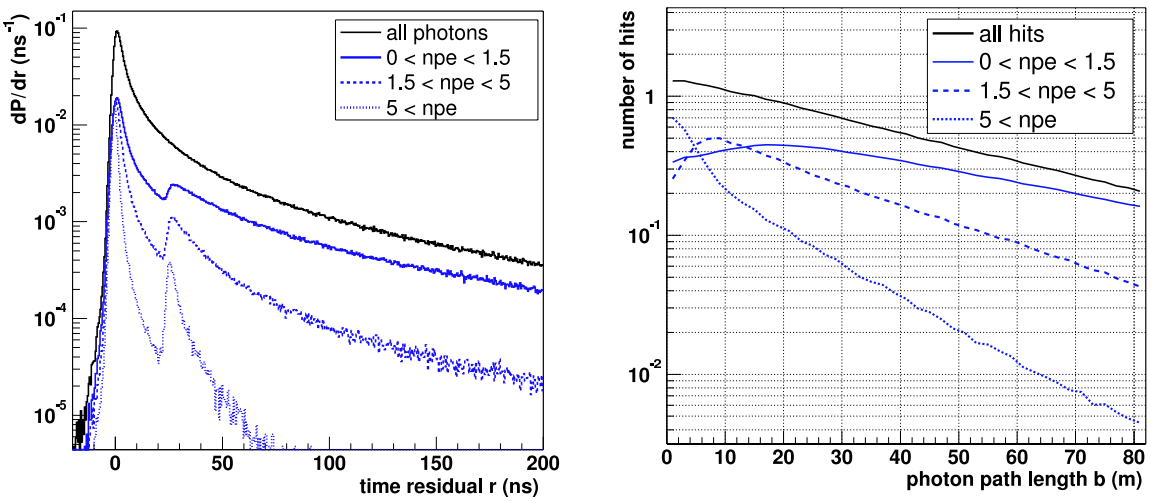

Figure 3.13: *Left: Distribution of the hit times relative to the expected arrival time for three ranges in the hit amplitudes. For comparison, the original distribution of the arrival times without simulation of the electronics is reproduced from figure 3.12 (top curve, labeled 'all photons'). Right: Average number of hits detected as a function of the photon path length for different hit amplitudes.*

3.5 Background

3.5.1 Background photons

In addition to the light from the muon and its secondaries, background light due to β-decay of ^{40}K and bioluminescence will be detected (see section 2.6). This background is simulated by adding hits to the simulated physics events. The time window for the generation of background hits ranges from 1500 ns before the time of the first signal hit to 1500 ns after the time of the last signal hit. The assumed background rate is 60 kHz per PMT. As was shown in section 2.6, this value corresponds to the background rate measured at the ANTARES site, but only during periods of low optical activity. For the periods with increased bioluminescence, the performance of the detector will be degraded

compared to the simulations presented here. Quantification of the impact of the elevated background rates should be the subject of future studies.

Besides complicating the reconstruction of genuine events, random background hits can also form patterns that mimic the signal produced by muons. Such pure background events could be reconstructed as up-going muons. The full impact of this background is currently under study and is not included in this analysis. Due to its combinatoric nature, this type of background can be reduced by selecting events with a large number of hits compatible with the muon track. Hence it is expected that this background will predominantly influence physics studies involving low energy ($\lesssim 100$ GeV) muons.

3.5.2 Atmospheric muons

Energetic down-going muons produced by interactions of cosmic rays with the Earth's atmosphere can reach the detector. Even though PMTs face downwards, many of these muons produce detectable light. The vast majority of these events can be rejected by selecting only up-going tracks as neutrino candidates. The remaining background stems from down-going muons that are wrongly reconstructed as up-going. Particularly dangerous, in this respect, are bundles of muons that are produced in the same air shower. The atmospheric muon background is simulated using the HEMAS package [62], which performs a full simulation of the atmospheric shower, starting from the interaction of the primary nucleus and resulting in muons at sea level. The muons are then propagated to the detector using the PROPMU package [53].

There are several limitations in the simulation of atmospheric muons. The high rate of atmospheric muons, implies that, with the limited computing power and storage space available, only several hours of this background could be fully simulated. Also, the zenith angle of the primary particles is limited to the range between 0 and 60° by the HEMAS package. Moreover, this simulation was performed with a somewhat different detector geometry (14 strings of 30 floors with 12 m floor spacing). A small sample using the new detector geometry was used to verify that no dramatic changes occur due to the difference in detector geometry. In particular, the distributions of the variables used in the event selection (see chapter 5) were checked to be compatible. New simulations, using the correct detector geometry and the more widely used CORSIKA package [63] for the shower simulation, are currently in production, but were not completed in time to be incorporated in this analysis.

3.5.3 Atmospheric neutrinos

Neutrinos that are produced in air showers initiated by cosmic rays, form a direct background to cosmic neutrinos. They can only be distinguished by their energy spectrum, which is known to be steep for atmospheric neutrinos but may be much flatter for cosmic neutrinos.

A distinction is made between neutrinos produced by the decay of pions and kaons, which dominate the flux at energies below 10^5 GeV and neutrinos produced by the decay of charmed mesons, which may dominate above that energy. For historical reasons, the flux of the former is called the conventional flux, while the latter are referred to as 'prompt'

neutrinos.

The conventional spectrum of atmospheric neutrinos has been calculated by various groups, e.g. FLUKA[64], Bartol [40] and HKKM[65]. The calculations rely on measurements of the energy spectrum and composition of cosmic rays and on models of the hadronic interactions producing the charged pions and kaons that decay into neutrinos. Differences in these assumptions lead to differences of the order of 20% in the predicted neutrino fluxes, which can be taken as a measure of the systematic uncertainty of the atmospheric neutrino flux.

Calculations of the prompt neutrino flux depend on models of the production cross section of charmed mesons in proton-nucleon collisions. This cross-section is poorly constrained by experiment. A review of prompt neutrino production is given in [66], where fluxes are presented for different models of charmed particle production: Recombination Quark Parton Model (RQPM), perturbative QCD (pQCD), and Quark Gluon String Model (QGSM). For each model, the ingredients of the calculation (e.g. the parameterisation used to represent the flux of primary cosmic rays) are varied, yielding a range of fluxes. In figure 3.14 the range of allowed prompt neutrino fluxes is shown for each of the charm production models. This illustrates that, in contrast to the models for the conventional neutrino flux, the uncertainty on the prompt neutrino flux is very large. The models of the prompt neutrino flux differ by two orders of magnitude.

Since atmospheric neutrinos form a background for the physics analysis, we have chosen to use the models that give the highest flux for both the conventional and prompt neutrino flux, namely the 'Bartol' flux [40], combined with the maximal prediction for the RQPM model for the prompt neutrinos.

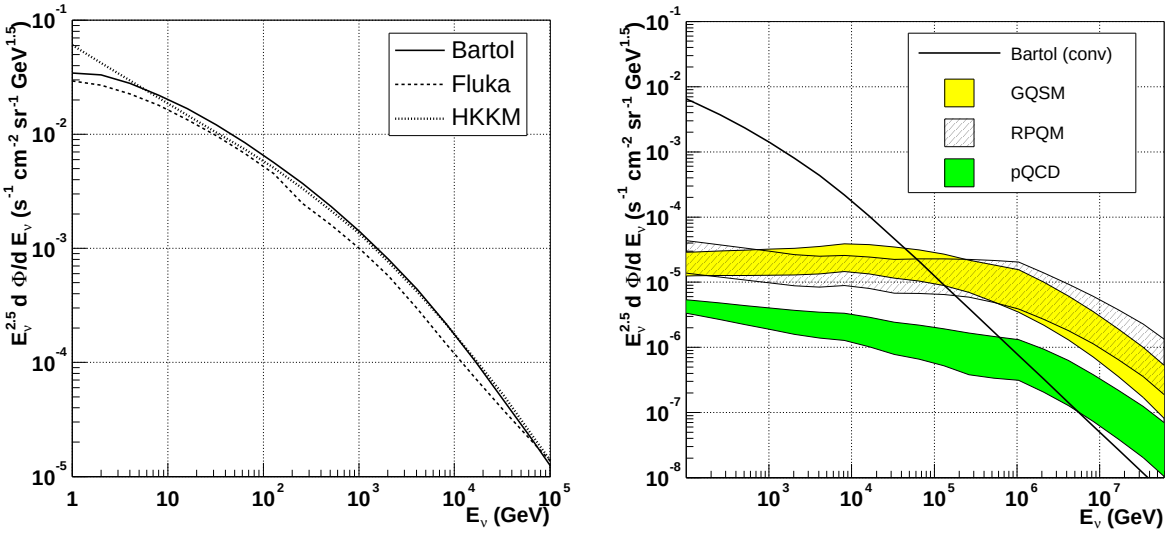

Figure 3.14: *Models of atmospheric neutrino fluxes. Left: three models for the conventional atmospheric neutrino flux. Right: The Bartol model and three models for prompt neutrino fluxes taken from [66]. The results have been integrated over all directions.*

The dependence of the atmospheric neutrino flux on the zenith angle is shown in fig-

ure 3.15. At energies below 100 TeV, the neutrino flux is enhanced near the horizon, because horizontal CRs interact high in the atmosphere, where the density is low. Therefore, the resulting mesons have more chance to decay before interacting [7]. At energies where the prompt neutrino flux dominates, there is basically no angular dependence, since the charmed mesons promptly decay before interacting (hence the name prompt neutrinos).

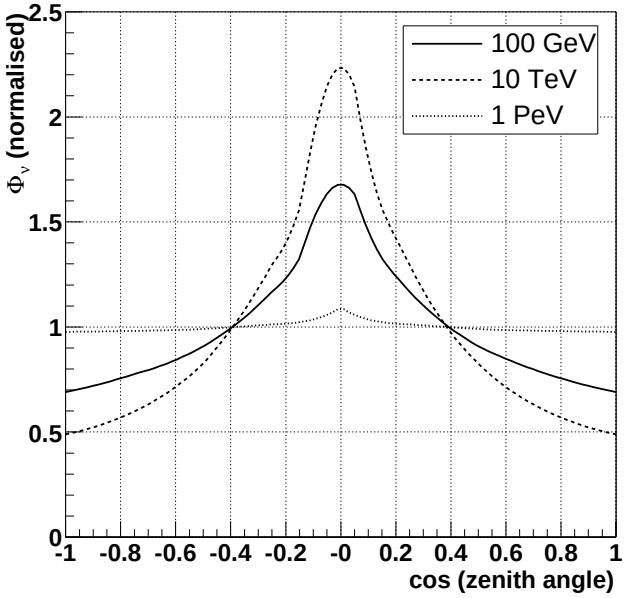

Figure 3.15: *The dependence of the atmospheric neutrino flux on the zenith angle of the neutrino for different values of the neutrino energy. The model used is from Bartol [40] + (maximal) RPQM [66].*

In this thesis, only muon neutrinos are taken into account. Atmospheric electron neutrinos that are reconstructed as up-going muons could contribute to the background. However, the flux of atmospheric electron neutrinos is heavily suppressed at high energies (e.g. at 1 TeV, $\Phi_{\nu_\mu}/\Phi_{\nu_e} \approx 20$). The reason is that the muons that produce the electron neutrinos (via decay) lose a large fraction of their energy in the atmosphere before decaying.

Furthermore, the effects of neutrino oscillations have been neglected. This can be expected to be a good approximation at high energies: above energies of a few hundred GeV, the oscillation length is already larger than the diameter of the Earth. The effect of oscillations of atmospheric neutrinos on the number of selected events will be quantified in section 5.2.4.

Chapter 4

Muon Track Reconstruction

In this chapter, the algorithms used to estimate the direction, position and energy of the muon from the arrival times and amplitudes of the hits are discussed. The accuracy of the reconstruction of the muon direction determines the pointing accuracy of the detector and is therefore a crucial parameter for searches for point sources of neutrinos.

The reconstruction algorithm consists of four consecutive fitting procedures. The last procedure produces the most accurate result, but requires a priori estimates of the muon track parameters that should be close to the true values. The purpose of the first stages in the chain of fitting procedures is to provide this starting point.

In section 4.1, the variables used to descibe the muon track and its relation to the OMs are introduced. The subsequent sections describe the four track fitting methods. In section 4.6, it will be described how these methods are combined to form the full reconstruction algorithm. The performance of the full algorithm is discussed in section 4.7. The energy of the muon is determined by a separate procedure, which will be discussed in section 4.8.

4.1 Track description and relation to the OM

The muon trajectory can be characterised by the direction $\vec{d} \equiv (d_x, d_y, d_z)$ and the position $\vec{p} \equiv (p_x, p_y, p_z)$ of the muon at some fixed time t_0. At energies above the detection threshold (10 GeV or so) the muon is relativistic. Hence, the speed of the muon is taken to be equal to the speed of light in vacuum. The direction can be parameterised in terms of the azimuth and zenith angles θ and ϕ: $\vec{d} = (\sin\theta\cos\phi, \sin\theta\sin\phi, \cos\theta)$. There are thus five independent parameters that are estimated by the reconstruction algorithm. For a given track (i.e. a given $\vec{d}$ and $\vec{p}$) and an OM at position $\vec{q}$, who's field of view is oriented in the direction $\vec{w}$, the relevant properties of a Cherenkov photon emitted from the muon track are:

- the expected (*th*eoretical) arrival time of the photon (t^{th}),
- the expected photon path length (b) and
- the expected cosine of the angle of incidence of the photon on the OM (a), i.e. the angle between the direction of the photon and the pointing direction of the PMT.

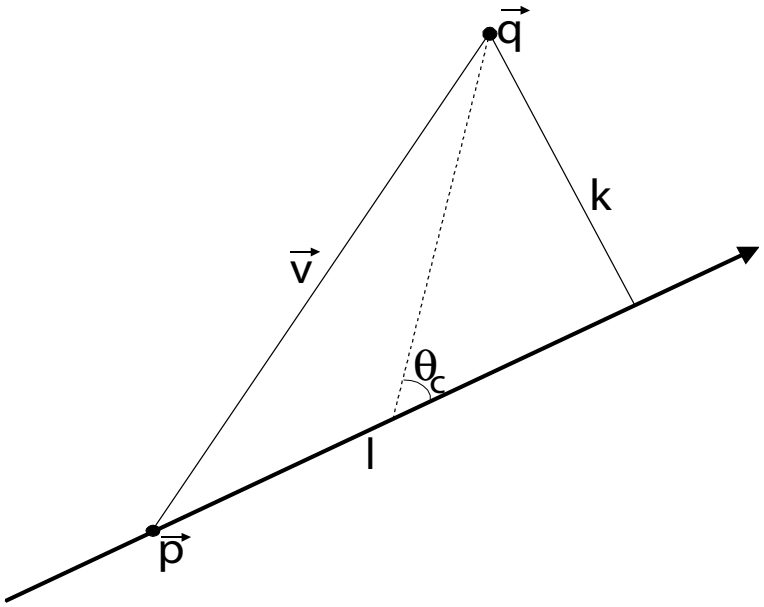

Figure 4.1: *Description of the geometry of the detection of the Cherenkov light. The muon goes through point $\vec{p}$ in the direction $\vec{d}$. The Cherenkov light is emitted at an angle θ_C with respect to the muon track and is detected by an OM located in point $\vec{q}$. The dashed line indicates the path of the light.*

These three quantities completely[1] characterise the position and orientation of the OM relative to the track. They are calculated under the assumption that the light is emitted under the Cherenkov angle w.r.t. the muon and travels in a straight line to the OM. The true arrival time, path length and angle of incidence may differ from these values, since photons are also emitted from secondary electrons and their path is influenced by scattering. The expected time of arrival t^{th} is used in all reconstruction algorithms. The quantities a and b will be used to predict the number of detected photons in sections 4.4 and 4.8.

In order to calculate t^{th}, we first define (see figure 4.1)

$$\vec{v} = \vec{q} - \vec{p}. \tag{4.1}$$

The components of $\vec{v}$ parallel and perpendicular to the muon direction are $l = \vec{v} \cdot \vec{d}$ and $k = \sqrt{\vec{v}^2 - l^2}$ respectively. The arrival time of the light in $\vec{q}$ is then given by

$$t^{th} = t_0 + \frac{1}{c}\left(l - \frac{k}{\tan\theta_c}\right) + \frac{1}{v_g}\left(\frac{k}{\sin\theta_c}\right), \tag{4.2}$$

where v_g is the group velocity of light, for which we take the value at 460 nm. The second term is the time it takes for the muon to reach the point where the detected light is

[1]The position of the OM w.r.t. the track has two degrees of freedom, since the situation is symmetric for rotations around $\vec{d}$. The orientation of the OM gives only one degree of freedom, since the response of the OM is (assumed to be) invariant under rotations around $\vec{w}$.

emitted, while the third term is the time it takes the light to travel from that point to $\vec{q}$. The length of the photon path is given by

$$b = \frac{k}{\sin\theta_C}. \tag{4.3}$$

The cosine of the angle of incidence of the photon on the OM is given by

$$a = \left[\vec{v} - \vec{d}\left(l - \frac{k}{\tan\theta_C}\right)\right] \cdot \vec{w}, \tag{4.4}$$

where $\vec{w}$ is the pointing direction of the OM. For a head-on collision of a photon with the photocathode $a = -1$, whereas $a = 1$ means the photon hits the insensitive rear of the OM.

4.2 Linear prefit

The first stage in the track reconstruction procedure is the 'linear prefit'. This is a linear fit through the positions of the hits, with the hit time as independent variable. The position associated with the ith hit is denoted by (x_i, y_i, z_i). In order to obtain a linear relation between the hit positions and the track parameters, it is assumed that the hits occur on points that are located on the muon track. This is expected to be a reasonable approximation if the length of the muon track in the detector is much larger than the attenuation length of the light. Under this approximation, the following relation holds:

$$\mathbf{y} = \mathbf{H\Theta}, \tag{4.5}$$

where $\mathbf{y}$ is a vector containing the hit positions, $\mathbf{y} = [x_1, y_1, ..., z_n]$, $\mathbf{\Theta}$ is a vector containing the track parameters: $\mathbf{\Theta} = [p_x, d_x, p_y, d_y, p_z, d_z]^{\mathrm{T}}$. These two vectors are related by a matrix containing the hit times:

$$\mathbf{H} = \begin{bmatrix} 1 & ct_1 & 0 & 0 & 0 & 0 \\ 0 & 0 & 1 & ct_1 & 0 & 0 \\ 0 & 0 & 0 & 0 & 1 & ct_1 \\ 1 & ct_2 & 0 & 0 & 0 & 0 \\ 0 & 0 & 1 & ct_2 & 0 & 0 \\ \vdots & \vdots & \vdots & \vdots & \vdots & \vdots \\ 0 & 0 & 0 & 0 & 1 & ct_n \end{bmatrix}. \tag{4.6}$$

The error estimates on the hit positions are stored in the covariance matrix $\mathbf{V}$, the inverse of which is called $\mathbf{F}$. Uncertainties on the hit times are neglected.

The estimate of the track parameters, $\hat{\mathbf{\Theta}}$, is given by those parameters that minimise the χ^2:

$$\chi^2 = [\mathbf{y} - \mathbf{H}\hat{\mathbf{\Theta}}]^{\mathrm{T}}\mathbf{V}^{-1}[\mathbf{y} - \mathbf{H}\hat{\mathbf{\Theta}}]. \tag{4.7}$$

This yields

$$\hat{\mathbf{\Theta}} = [\mathbf{H}^{\mathrm{T}}\mathbf{V}^{-1}\mathbf{H}]^{-1}\mathbf{H}^{\mathrm{T}}\mathbf{V}^{-1}\mathbf{y}. \tag{4.8}$$

It is now assumed that the covariance matrix is diagonal (i.e. that all errors are uncorrelated) and that the uncertainties on the x, y and z components of the position of an individual hit are equal. In this case, $\mathbf{V}$ and $\mathbf{V}^{-1}$ are diagonal and equation 4.8 can be expressed as

$$\hat{\mathbf{\Theta}} = \frac{1}{\sum_i f_i \sum_i f_i c^2 t_i^2 - (\sum_i f_i c t)^2} \begin{bmatrix} \sum_i f_i c^2 t_i^2 \sum_i f_i x_i - \sum_i f_i c t_i \sum_i f_i c t_i x_i \\ \sum_i f_i \sum_i f_i c t_i x_i - \sum_i f_i c t_i \sum_i f_i x_i \\ \sum_i f_i c^2 t_i^2 \sum_i f_i y_i - \sum_i f_i c t_i \sum_i f_i c t_i y_i \\ \sum_i f_i \sum_i f_i c t_i y_i - \sum_i f_i c t_i \sum_i f_i y_i \\ \sum_i f_i c^2 t_i^2 \sum_i f_i z_i - \sum_i f_i c t_i \sum_i f_i c t_i z_i \\ \sum_i f_i \sum_i f_i c t_i z_i - \sum_i f_i c t_i \sum_i f_i z_i \end{bmatrix}, \quad (4.9)$$

where f_i^{-1} is the uncertainty on the position of hit i, and t_i is the time of that hit.

4.2.1 Hit positions

In the previous section it was not specified how the positions associated with the hits are determined. The standard method [67, 68] is simply to use the positions of the OMs on which the hits occur. However, the assumption used in equation 4.5 is that the hit positions are located on the muon track, which is not the case if the OM positions are used. In order to improve the track estimate, a different approach was taken. Here, we try to determine, for each hit, a position which is most likely to be located on the track. If a hit occurs on a given OM, it can be expected that the track passes some distance in front of that OM. This distance is estimated from the amplitude of the hit.

Using simulated events, the spatial distribution of the point of closest approach of the hit to the track is determined as a function of the amplitude of the hit. Figure 4.2a shows this distribution for hits with an amplitude between 0.5 and 1.5 photo-electron (p.e.). The maximum of this distribution is located along the pointing direction of the PMT. The position of the maximum can therefore be characterised by a distance from the OM. The approximate spherical symmetry of the distribution implies that the uncertainties on the x, y and z-coordinates of the positions are almost uncorrelated and equally large. They are assumed to be equal to the RMS of the distribution.

Figure 4.2b shows the average distance between the muon track and the PMT, as well as its uncertainty, as a function of the hit amplitude. As expected, hits with high amplitudes are likely to have passed the PMT at close distance, while for low amplitude hits, the position of closest approach is much more uncertain and, on average, further away from the PMT.

4.2.2 Constraining the muon velocity

When using equation 4.9 to estimate the direction of the muon, its velocity, c $\sqrt{d_x^2 + d_y^2 + d_z^2}$, is left free. An attempt was made to improve the estimates of the track parameters by constraining the velocity of the muon to the speed of light in vacuum (c) using the technique of Lagrangian multipliers. The analytic calculation, which was made under the same assumptions about the covariance matrix that were made in the previous section, shows that the inclusion of this constraint does indeed normalise the velocity to c, but

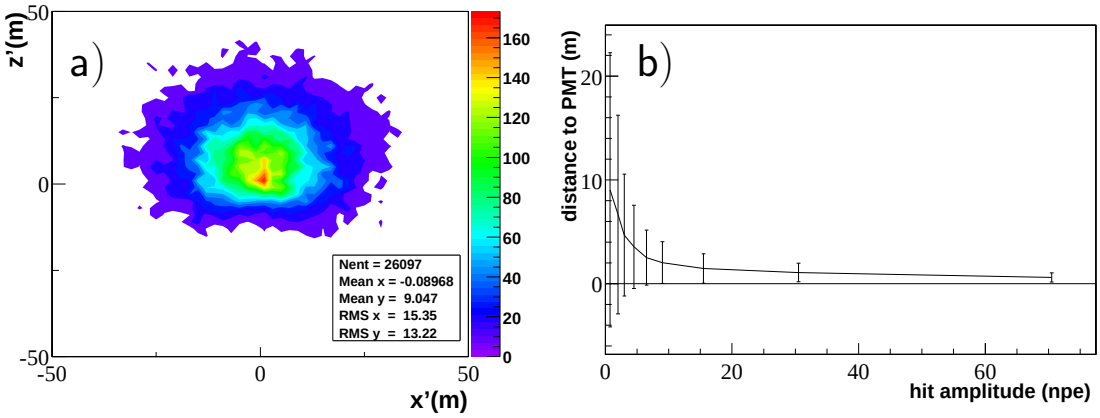

Figure 4.2: *a) The distribution of the points of closest approach of the muon to a PMT in a coordinate system where the positive z'-axis points along the orientation $\vec{w}$ of the PMT and where the x'-axis is perpendicular to both the z'-axis and the vertical. The distribution shown is for hits with an amplitude between 0.5 and 1.5 p.e. b) The average distance of the point of closest approach of the muon track to the OM as a function of hit amplitude. The error bars indicate the spread of this position.*

that the estimated direction of the muon is not affected by this constraint. It is therefore easier to use equation 4.9 and to set the velocity afterwards.

4.2.3 Performance

Throughout this chapter, the performance of the reconstruction algorithms will be summarised by the distribution of the reconstruction error, α_μ, which is defined as the angle between the true direction of the muon and the direction of the reconstructed track. Simulated through-going muons are used with an E_μ^{-1} energy spectrum in the range between 100 GeV and 100 TeV. In order to evaluate the performance of the individual fitting routines, the fits will be performed using hits that occur on OMs within a distance of 150 m from the true muon track and that have time residuals between -150 and 150 ns as calculated using the true muon track.

The distribution of α_μ is shown in figure 4.3 for the results of the linear prefit with the improved estimation of the hit positions. For comparison, the performance is also shown for the standard method for determination of the hit positions. Compared to the standard version, a small improvement is achieved: the number of tracks which are reconstructed with an error on the direction smaller than 10° (5°) is increased by about 15% (30%).

4.3 Maximum likelihood fit

Two of the fit procedures used rely on the principle of Maximum Likelihood (ML). For each possible set of track parameters, the probability to obtain the observed events can

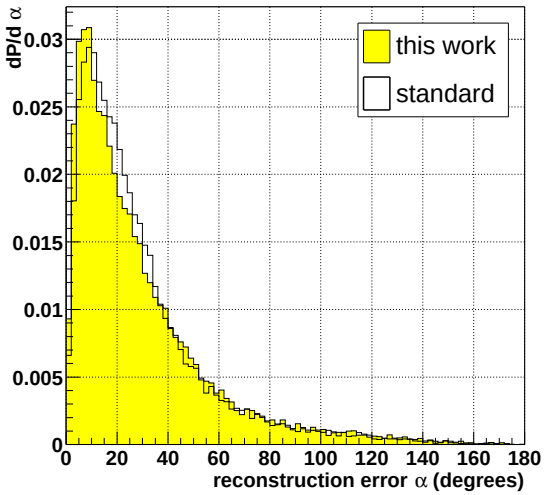

Figure 4.3: *Distribution of the error of the reconstructed muon direction for the improved and original versions of the linear prefit.*

be calculated. This probability is called the likelihood of the event. The likelihoods that are used here, only take into account the probability of the time of the hits. In case of uncorrelated hits, the likelihood of the event can be written as the product of the likelihood of the individual hits:

$$P(\text{event}|\text{track}) \equiv P(\text{hits}|\vec{p},\vec{d}) = \prod_i P(t_i|t_i^{th}, a_i, b_i, A_i), \tag{4.10}$$

where t_i is the time of hit i, A_i the hit amplitude and t_i^{th}, a_i and b_i were introduced in section 4.1. The ML estimate of the track is defined by the set of track parameters for which the value of the likelihood function is maximal.

Since a full search of the five dimensional parameter space is prohibitively time consuming, standard numerical tools [69] are used to find the maximum of the likelihood function[2]. These tools iteratively approximate the maximum by using information on the gradient of the likelihood function. If the likelihood function has multiple maxima, the maximisation algorithm will, in general, not find the global maximum, but converge on a local maximum. The efficiency for finding the global maximum is therefore related to the shape (i.e. the gradient) of the likelihood function and to the quality of the starting point that is used for the fit.

4.3.1 Original PDF

In the simplest case, the a, A and b dependence in equation 4.10 are neglected and the likelihood is expressed solely in terms of the probability density of the residuals $r_i = t_i - t_i^{th}$. The Probability Density Function (PDF) that is described in this section was developed for the first reconstruction algorithm used in ANTARES [68, 70]. This 'original' PDF is shown in figure 4.4. When comparing this with figure 3.12, it is clear that background hits are not taken into account in this PDF. Instead, a non-physical tail is present for residuals $r < -5$ ns. This tail was included in order to provide a gradient in the likelihood function for negative r, which helps the maximisation routine to converge.

[2] In practice, the maximum of L is found by minimising $-\log(L)$

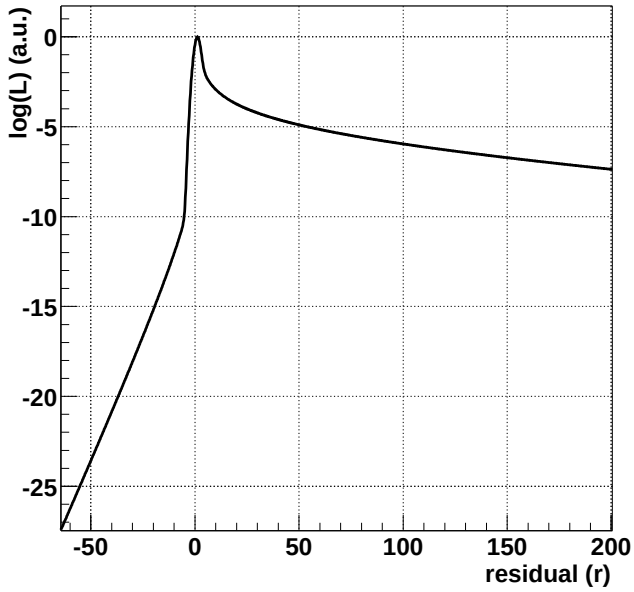

Figure 4.4: *The 'original' PDF of the hit residuals.*

4.3.2 Performance

The performance of the ML estimator has been evaluated in the same way as was done for the linear prefit. Distributions of α_μ obtained with the original PDF are shown in figure 4.5. To evaluate the dependence on the quality of the track estimate that is used as a starting point for the maximisation procedure, the fit has been performed using the true muon track and random tracks that make an angle α_0 of 1°, 10°, and 45° with the true muon track. As expected, the quality of the fit result is degraded when the value of α_0 is increased.

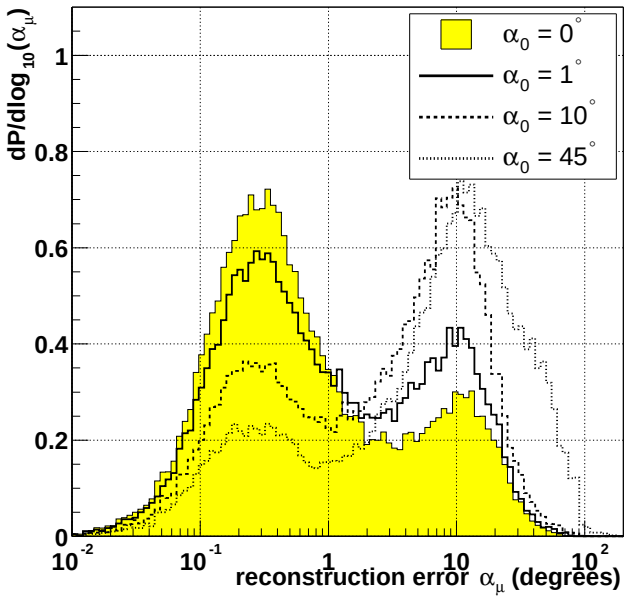

Figure 4.5: *Distribution of the reconstruction error on the direction of the muon obtained from the ML fit with the 'original' PDF. The fits have been started with track parameters that were taken at different angles α_0 from the true muon track.*

4.4 Maximum likelihood fit with improved PDF

As was already mentioned, the original PDF introduced in the previous section does not include background hits. As a result, background hits, especially those with negative residuals, can degrade the performance of the track reconstruction. In this section, a new PDF is presented in which background hits are taken into account.

4.4.1 PDF with background

The background hits are uniformly distributed in time. As a consequence, the PDF of the hit residuals $P(r)$ can only be normalised if the duration of the event is specified. It is assumed that an event consists of all hits with residuals between $-T/2$ and $T/2$. The event duration T is assumed to be large enough to contain all signal hits.

The PDF has contributions from background hits and from signal hits. The PDF of the signal depends on the amplitude of the hit A: $P^{\text{sig}}(r|A)$.

The relative contributions from these two types of hits are determined by the expected number of signal and background hits, which are determined from the hit amplitude, and the parameters a and b:

$$P(r_i|a_i, b_i, A_i) = \frac{1}{N^T(a_i, b_i, A_i)}[P^{\text{sig}}(r_i|A_i)N^{\text{sig}}(a_i, b_i, A_i) + R^{\text{bg}}(A_i)], \tag{4.11}$$

where $R^{\text{bg}}(A_i)$ is the background rate[3] for hits with amplitude A_i and $N^{\text{sig}}(a_i, b_i, A_i)$ is the expected number of signal hits as a function of the hit amplitude and a and b. Finally $N^T(a_i, b_i, A_i)$ is the total expected number of hits of amplitude A_i in the event (of duration T), which is given by

$$N^T(a_i, b_i, A_i) = N^{\text{sig}}(a_i, b_i, A_i) + R^{\text{bg}}(A_i)T. \tag{4.12}$$

The factor $1/N^T(a_i, b_i, A_i)$ ensures that $\int_{-T/2}^{T/2} P(r)dr = 1$ if $\int_{-T/2}^{T/2} P^{\text{sig}}(r_i)dr = 1$. The PDF is thus normalised for all values of A, a and b, provided T is known. The relative contributions of the signal and background terms in equation 4.11 are independent of the event duration T. However, if the value of T is incorrect (i.e. if the fit is performed with hits from a larger time window than what is assumed in equation 4.11), the normalisation of the PDF will depend on a and b and thus on the track parameters, which is undesirable. The knowledge of T is thus needed in the reconstruction.

4.4.2 Parameterisation of the PDF

In order to use standard software tools [69] to maximise the likelihood function, it is convenient to parameterise the likelihood function with a continuous, differentiable function. The parameterisation is obtained by fitting a set of histograms obtained from Monte Carlo simulations of muons traversing the detector. For this, the muons have an energy between 100 GeV and 100 TeV and have a spectrum $\frac{dN}{dE} \propto E^{-1}$ (an E^{-1} spectrum, for short). The

[3] Equation (4.11) looks more symmetric for signal and background when $R^{\text{bg}}(A_i)$ is substituted by $N^{bg}P^{bg}$, with $N^{bg} = R^{\text{bg}}T$ and $P^{bg} = 1/T$.

bin	$A_{\min}$	$A_{\max}$	c_1(ns)	c_2(ns)	$\mathcal{A}$(ns^{-1})	τ(ns)	σ(ns)	$\mathcal{C}$(ns^{-1})	η(ns)	ρ(ns)
1	0	1.5	1.55	10.8	0.06	0.72	2.65	0.32	294	13.7
2	1.5	2.5	1.30	9.17	0.11	0.41	2.35	0.27	120	11.9
3	2.5	5	1.58	2.91	0.18	0.11	2.07	0.08	82.7	-1.41
4	5	10	1.35	3.07	0.25	-0.19	1.77	0.04	55.2	-1.74
5	10	∞	0.80	3.04	0.33	-0.51	1.44	0.02	49.5	-2.01

Table 4.1: *Values used in the parameterisation of the PDF of the hit residuals (see equation 4.13).*

obtained distributions, and the parameterisations obtained from them, correspond to a (weighted) average over this energy range.

The likelihood function was parameterised separately for hits of different amplitudes. In order to obtain enough statistics, the hits were classified into 5 amplitude bins (with boundaries 0, 1.5, 2.5, 5, 10 and ∞ p.e.).

Time dependence

Figure 4.6 shows the PDF of the time residuals of the signal hits for the different amplitude bins, $P^{\text{sig}}(r|A_i)$, as obtained from the simulation. These distributions have been parameterised using the following functional form:

$$\frac{dP^{\text{sig}}}{dr} = \begin{cases} \mathcal{A}\, e^{\frac{-(r-\tau)^2}{2\sigma^2}} & \text{if } r < c_1 \\ \mathcal{B}\,(\alpha r^3 + \beta r^2 + \gamma r + 1) & \text{if } c_1 < r < c_2 \\ \mathcal{C}\,\frac{e^{-r/\eta}}{r+\rho} & \text{if } r > c_2. \end{cases} \tag{4.13}$$

The peak of the distribution is fitted with a Gaussian function, while the tail has been approximated by the function $\frac{e^{-r/\eta}}{r+\rho}$. These two functions are joined together by a 3rd degree polynomial function. The coefficients of this polynomial are fixed by imposing that the function is continuous and differentiable at the points $r = c_1$ and $r = c_2$. The values of c_1 and c_2 have been left free in the fit. The parameterisations thus obtained are also shown in figure 4.6. The peaks at $r = 25$ ns that result from the integration of the PMT signal (see section 3.3.2) have not been incorporated in the parameterisation of the PDF. This was done in order to keep the parameterisation as simple as possible and to reduce the possibility of local minima in the likelihood function. The values of the parameters obtained with the fits are shown in table 4.1. It can be seen that, with increasing hit amplitude, the position of the peak shifts to smaller values of the time residual, while its width decreases.

Number of signal and background hits

As explained in section 4.4.1, the expected number of signal hits N^{sig} of a given amplitude, is estimated from the parameters a and b. For simplicity, it was assumed that this dependence can be factorised:

$$N^{\text{sig}}(a,b) = N^{\text{sig}}(b) \times f(a), \tag{4.14}$$

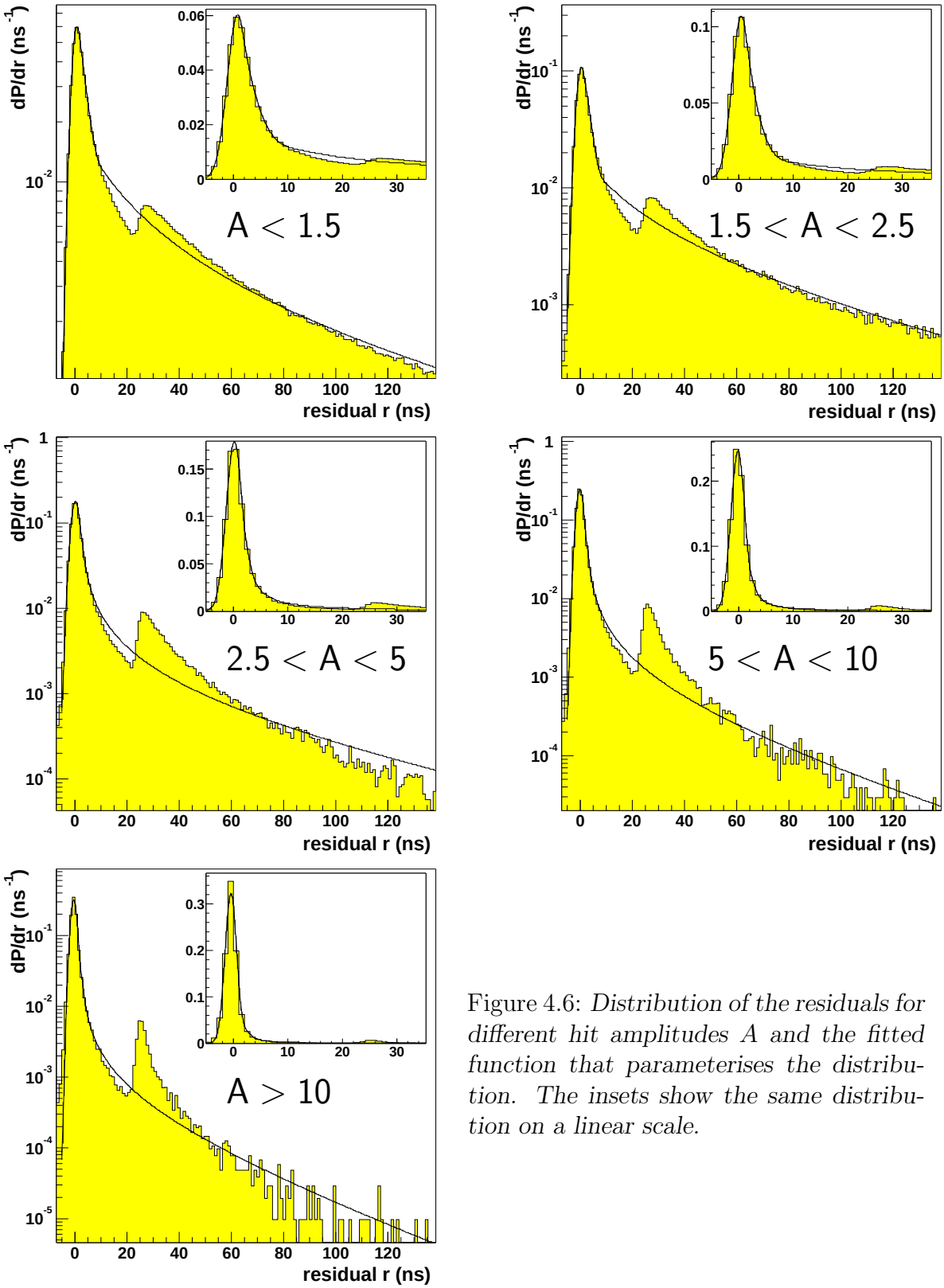

Figure 4.6: *Distribution of the residuals for different hit amplitudes A and the fitted function that parameterises the distribution. The insets show the same distribution on a linear scale.*

where $N^{\text{sig}}(b)$ is the expected number of signal hits as a function of the distance and $f(a)$ describes the dependence on the angle of incidence of the photon on the PMT. The first has been parameterised by the following function:

$$N^{\text{sig}}(b) = \frac{(b+\upsilon)e^{\zeta+\xi b}}{b^{\psi}+\chi}, \tag{4.15}$$

where the values of $\upsilon, \zeta, \xi, \psi$ and χ have been determined by a fit to the simulated events. This function is an extension of the simple function introduced in section 3.4, which does not take into account the readout electronics. The additional factor $(b+\upsilon)$ and the additional parameters ψ and χ allow to incorporate the effects of the simulation of the electronics for all amplitudes. The function $f(a)$ resembles the angular acceptance function of the PMT that was shown in figure 3.10. It is parameterised by a 4th order polynomial. The parameterisations of the functions $N^{\text{sig}}(b)$ and $f(a)$ are obtained from simulations. The results of the simulations are shown in figure 4.7 together with the obtained parameterisations.

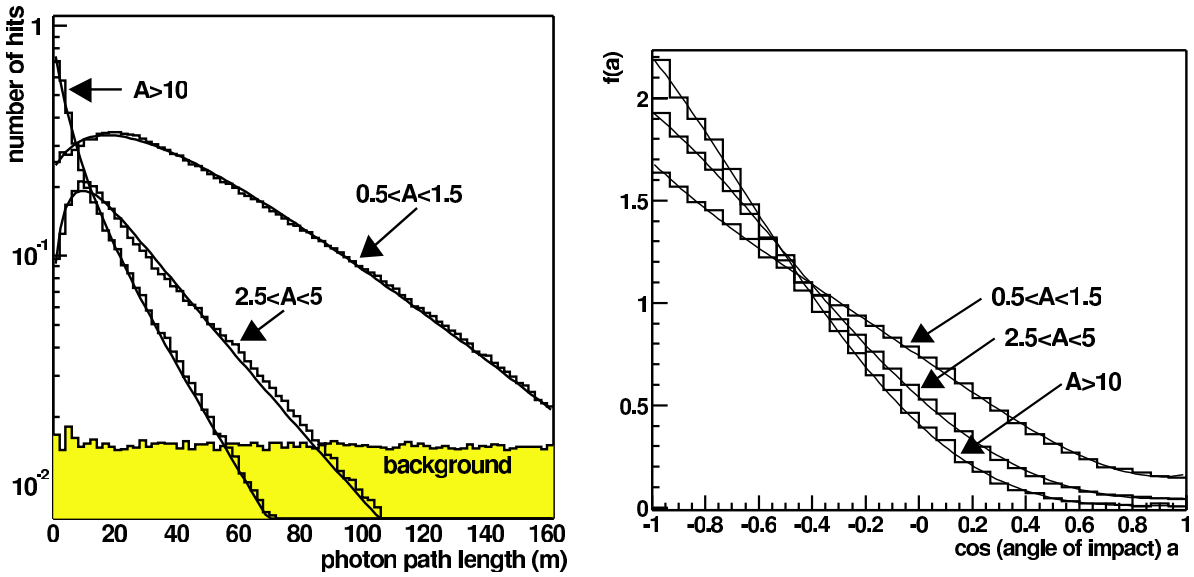

Figure 4.7: *Left: Number of expected hits as a function of the distance travelled by the photon for different hit amplitudes. The number of background hits detected in a 250 ns time window is also shown. Right: Dependence of the number of hits on the angle of incidence of a photon, emitted under θ_C for different hit amplitudes. The smooth curves are the parameterisations (see text). For clarity, curves are only shown for three of the five amplitude bins.*

The rate of background hits, $R^{\text{bg}}(A)$ is independent of both a and b, but it does depend on the amplitude A of the hit. The optical background consists mostly of single photo-electron hits. Due to the resolution of the amplitude measurement of about 30%, the measured amplitude of single p.e. hits will not be precisely 1 p.e. Hits with a measured amplitude below 2 p.e. are assumed to be single photo-electron hits; the background

rate used for these hits in equation 4.11 is $R^{\mathrm{bg}}(1) = 60$ kHz. Background hits with amplitudes above 2 p.e. are assumed to be caused by multiple background photons that, by coincidence, are detected within the 25 ns integration time of the ARS. The expected rate $R(A)$ of background hits with amplitude $A > 2$ p.e. is computed by multiplying the single p.e. rate $R(1)$ with the chance probability of detecting $A-1$ additional background photons within the 25 ns integration time:

$$R^{\mathrm{bg}}(A) = R^{bg}(1) \times (25 \text{ ns} \times R^{bg}(1))^{A-1}. \tag{4.16}$$

4.4.3 Performance

The performance of the ML fit with the improved PDF has been evaluated in the same way as the ML fit with the original PDF (section 4.3.1). As a starting point of the fit, tracks were used that were taken at different angles α_0 from the true track. The results are shown in figure 4.8. When the fit is started close to the true track ($\alpha_0 = 0°$ or $1°$), the reconstruction error is small (typically $0.3°$). A large improvement is observed compared to the original likelihood fit (see figure 4.5). For larger values of α_0, however, the correct solution is less likely to be found. Instead, a local maximum in the likelihood function is found, which is close to the starting point. In some events, the gradient of the likelihood function at the starting point is too small for the maximisation algorithm to start.

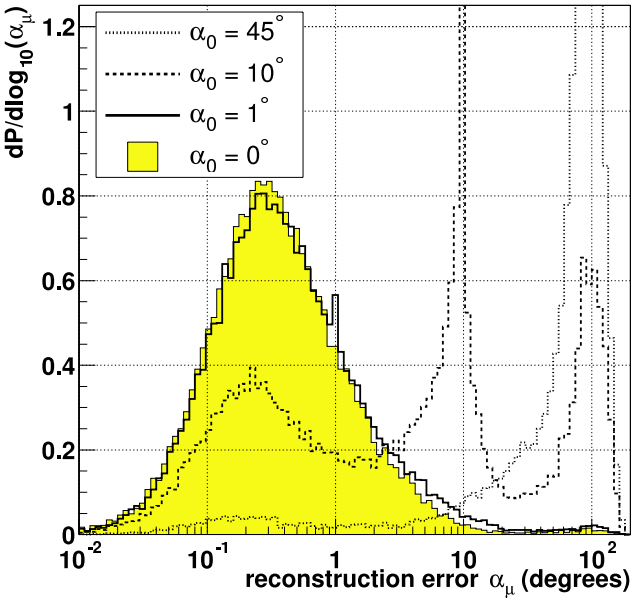

Figure 4.8: *Distribution of the reconstruction error α_μ obtained from the ML fit with the improved PDF. The fits have been started with track parameters that were taken at different angles α_0 from the true muon track.*

The strong sensitivity on the quality of the starting points can be understood by the weak dependence of the PDF on large time residuals. If the starting point is bad, the gradient of the likelihood function will be very small or may be dominated by only a small number of (background) hits, which happen to have a small residual with respect to the track used as a starting point. In such cases a local maximum can be found. In conclusion, the ML estimate with the improved PDF presented in this section leads to

accurate track reconstruction, provided a good starting point for the fit is given.

4.5 M-estimator

In the previous section, it was found that the ML estimate is very sensitive to the quality of the track estimate that is used as a starting point. The same is true for the ML estimate using the original PDF discussed in section 4.3. This has been known in ANTARES for a long time and it was the reason to use the linear prefit in previous fitting algorithms. In addition, the non-physical tail of the original PDF was added in order to improve the efficiency for finding the correct maximum in the likelihood function.

There seems to be a trade-off between the accuracy of the reconstruction and the efficiency of finding the global maximum of the likelihood function. The latter is expected to be large if the derivative of the fitted function is non-zero for large residuals r. In this section, we therefore abandon the notion that the fit function is only meant to describe the data. Instead the behaviour for large r should be such that there is a favourable trade-off between an accurate description of the data and the efficiency of finding the global maximum.

In the literature [71], estimators that work by maximising some function g (in our case $g(r)$), are known as M-estimators. In a sense, the maximum likelihood estimator is a special case of an M-estimator ($g(r) = P(r)$), as is the least squares estimator ($g(r) = -r^2$)). Other, more ad hoc, forms of g are often used for so-called robust estimation, i.e. estimation which is insensitive to large fluctuations in a small number of data points. The data points with large fluctuations are usually called 'outliers'. In the case of track fitting in ANTARES, a robust fit is already available, namely the improved ML estimator, which incorporates the outliers (i.e. the background hits) in the PDF. Nevertheless, by choosing an M-estimator that behaves suitably for large residuals, it can be expected that a reasonable track estimate can be obtained without the requirement of an accurate starting point. It has been found that the following function gives good results:

$$g(r) = -2\sqrt{1 + r^2/2} + 2. \tag{4.17}$$

The resulting M-estimator is called 'L1-L2' [72]. For large values of r, this function is linear in r, while for small r it is quadratic.

The performance of the M-estimator was found to improve when the hit amplitude of the hits is used as a weighting factor for the time residuals. Furthermore, a term was added, which contains the angular response function $f_{\text{ang}}(a)$ of the optical module (see section 3.3.2). The function that is finally maximised to obtain a track estimate is given by

$$G = \sum_i \kappa(-2\sqrt{1 + A_i r_i^2/2}) - (1 - \kappa) f_{\text{ang}}(a_i). \tag{4.18}$$

The relative weights of the two terms are determined by the parameter κ, which was optimised using Monte Carlo events. The value used here is $\kappa = 0.05$. The small value of κ does not mean that the second term is dominant in the fit, since the influence of the two terms depends on their derivatives w.r.t. the track parameters.

4.5.1 Performance

The performance of the M-estimator fit is shown in figure 4.9. Again, starting values were taken at different angles from the true track. In contrast to the maximum likelihood fits, the result of the M-estimator is hardly influenced by the choice of the starting values. Only when started at 45° from the true track, the performance is somewhat degraded. As expected, the M-estimator is considerably less accurate than the ML methods, but most of the events are reconstructed with an accuracy of a few degrees, which is much more accurate than the result of the linear prefit shown in figure 4.3. The performance is adequate as a starting point for the ML fit.

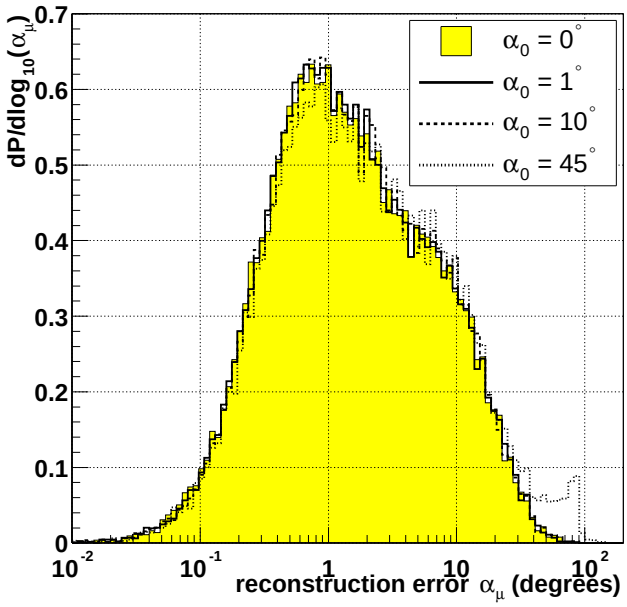

Figure 4.9: *Distribution of the reconstruction error obtained from the M-estimator. The fit was started with tracks that were generated at different angles α_0 from the true muon track.*

It should be noted, however, that the hits used to obtain the results in figure 4.9 are selected using information about the direction of the true track (see section 4.2.3). If no good starting point is available for the fit, the signal hits cannot be selected in this way and the performance will, in general, be degraded.

4.6 Combining the fitting algorithms

In sections 4.2 to 4.5, four different fitting procedures were discussed. This section describes how they are combined into the final reconstruction program and how the hits are selected that are used for each of the procedures. The full reconstruction algorithm may be summarised as follows:

1. **Pre-selection of hits:** In the simulated events, background hits are generated in an arbitrary time window around the event. In order to make the algorithm insensitive to the amount of background simulated, a rough, first selection is made. All hits are selected for which $|\Delta t| \leq \frac{d}{v_g} + 100$ ns, where Δt is the time difference between a hit

and the hit with the largest amplitude in the sample and d is the distance between the OMs of the two hits. Hits with larger time differences cannot be related to the same muon, unless they have a residual larger than the 'safety factor' of 100 ns. Since the hit with the largest amplitude is virtually always a signal hit, almost no signal hits are rejected.

2. **Linear prefit:** The first fit is the linear prefit described in section 4.2. Although not very accurate, it has the advantage that it requires no starting point. It is therefore suited as a first step. The linear prefit is made with a sub-sample of the hits. Only hits in local coincidences and hits with amplitudes larger than 3.0 p.e. are used. A local coincidence is defined as a combination of 2 or more hits on one floor within 25 ns.

3. **M-estimator fit:** The insensitivity to the quality of the starting point of the M-estimator fit (see section 4.5) makes it a natural choice for the next step. The hits used for this fit are selected on the basis of the result of the prefit. In order to be selected, a hit must have a time residual w.r.t. the t^{th} calculated from the parameters obtained with the linear prefit between -150 and 150 ns and a distance from the fitted track of less than 100 m. Hits with an amplitude larger than 2.3 p.e. are always selected.

4. **Maximum likelihood fit with original PDF:** The next step is the ML fit with the original PDF discussed in section 4.3. This fit is performed with hits that are selected based on the result of the M-estimator fit. This time, hits are selected with residuals between $-0.5 \times$ R and R, where R is the root mean square of the residuals used for the M-estimator fit. Hits that are part of a coincidence, or that have an amplitude larger than 2.5 p.e. are also selected. The asymmetry in the selection interval reflects the fact that the original PDF is asymmetric

5. **Repetition of steps 3 and 4 with different starting points:** It was found that the efficiency of the algorithm is improved by repeating steps 3 and 4 with a number of starting points that differ from the prefit. The result with the best likelihood per degree of freedom, as obtained in step 4, is kept. Four of the additional starting points are obtained by rotating the prefit track by an angle of 25°. The origin of the rotation is the point on the track that is closest to the centre of gravity of the hits. Four more starting points are obtained by translating the track ± 50 m in the direction $\vec{d} \times \hat{z}$ and ± 50 m in the $\hat{z}$ (i.e. upward) direction. In total, steps 3 and 4 are thus done 9 times. Some additional information about the procedure is kept. The number of starting points that result in track estimates which are compatible with the preferred result (i.e. which give the same track direction to within 1°), will be used in the event selection (section 4.7.1). This number is called N_{comp}. In case the likelihood of one of the results is very good, the remaining starting points are skipped for execution speed.

6. **Maximum likelihood fit with improved PDF:** Finally, the preferred result obtained in step 5 is used as a starting point for the ML fit with the improved PDF. The hit selection is also based on this result: hits are selected with residuals between

-250 and 250 ns and with amplitudes larger than 2.5 p.e. or in local coincidences. Since background is taken into account in the PDF, the presence of background hits in the sample does not jeopardise the reconstruction accuracy. This is reflected in the large time window used for the hit selection. As explained in section 4.4.1, the event duration is an input parameter for the final fit; with this selection T=500 ns.

Clearly, the overall algorithm contains many parameters, especially for the hit-selection criteria. While a full optimisation of these parameters was not feasible, the algorithm presented here has been found to perform well over a broad energy range. Nevertheless, further tuning of the algorithm may further improve the performance.

4.7 Performance of the full algorithm

In this section the performance of the full reconstruction algorithm is presented. Figure 4.10 shows the result of each of the fitting algorithms when they are used in sequence as described above. The increasing accuracy of the subsequent algorithms is apparent from this figure. Of all reconstructed muon tracks, 1.1% are reconstructed within 1° from the true track by the linear prefit (see table 4.2). This number is improved by the repetitive application of the M-estimator and the original ML fit to 38% and 57% respectively. The number is not increased much by the final fit (59%). The accuracy of the events, however, is improved: about 20% more events are reconstructed with an error smaller than 0.1°. The overall shift of the peak corresponds with a $\sim$ 20% overall improvement of the angular resolution.

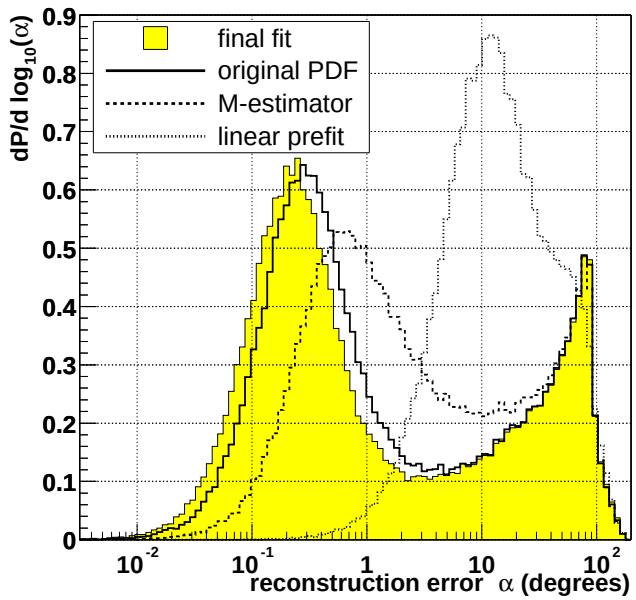

Figure 4.10: *Performance of the different fitting algorithms when used sequentially in the reconstruction program.*

While it is of minor importance for neutrino astronomy, the error on the position of the reconstructed muon track is shown in figure 4.11 for completeness. Most tracks are reconstructed within 1 m from the true track. As expected, there is a strong correlation

α_μ	0.1°	0.3°	1°	3°	10°
final fit	12.0	39.1	59.2	65.6	71.9
original PDF	7.85	32.1	56.9	65.2	71.8
M-estimator	2.03	12.5	38.4	56.9	69.6
linear prefit	0.01	0.10	1.10	7.99	39.4

Table 4.2: *Percentage of the events reconstructed within an angle α_μ w.r.t. the true track by the different fitting algorithms that together make up the full reconstruction algorithm.*

between the angular error and the error on the position. This is demonstrated in figure 4.11 by the distribution of the positional error for events where the muon is reconstructed with a directional error smaller than 1°.

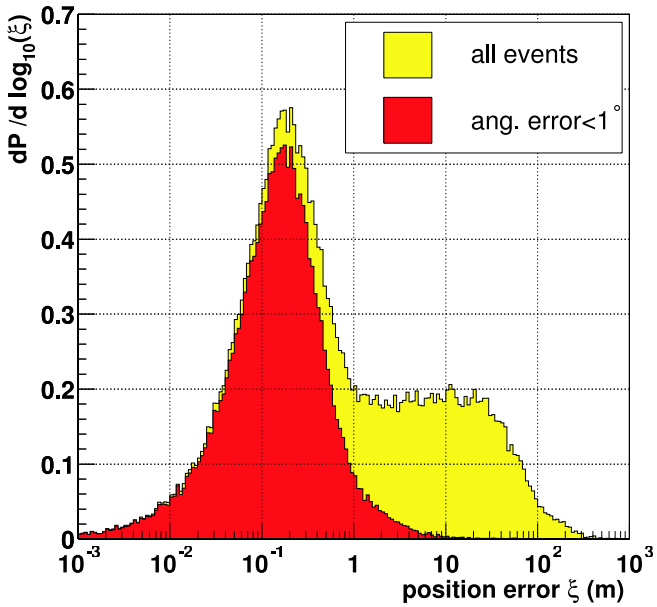

Figure 4.11: *Error on the position of the muon track, defined as the minimal distance between the true and the reconstructed muon tracks, for all reconstructed muons and for muons that are reconstructed with an angular error smaller than 1°.*

4.7.1 Handles on the reconstruction quality

The philosophy adopted in the reconstruction algorithm is to reconstruct as many events as possible without trying to reduce the number of badly reconstructed events by intermediate selection criteria. Rather, selection criteria can be applied afterwards, depending on the demands of the various physics analyses. As a consequence, many events are reconstructed with large errors. In this section, two variables are introduced which can be used to reject badly reconstructed events.

An obvious way to discriminate good and bad events is a cut on the value of the likelihood function at the fitted maximum[4]. As is shown in figure 4.12, there is an overall

[4]For brevity, we treat the likelihood as a dimensionless number; strictly speaking it has units ns^{-N}, with N the number of hits used in the fit.

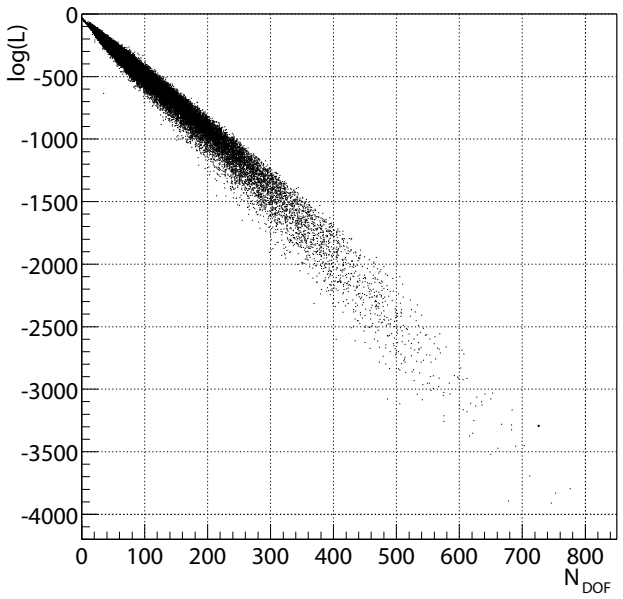

Figure 4.12: *Scatter plot of the value of the likelihood function at the fitted maximum and the number of degrees of freedom of the fit.*

linear relationship between $\log(L)$ and the number of degrees of freedom N_{DOF} in the fit. The latter is given by the number of hits used in the fit minus the number of fitted parameters, which is five. Therefore, the variable $\log(L)/N_{\mathrm{DOF}}$ is used to select the well reconstructed events. Figure 4.13 demonstrates that, as expected, $\log(L)/N_{\mathrm{DOF}}$ has a high value for well reconstructed events (in this case with directional errors smaller than 1°) and a low value for badly (in this case with errors larger than 45°) reconstructed events.

A second parameter is obtained from information about the multiple starting points that are used for the M-estimator and the subsequent ML estimator. It is the number of tracks compatible with the preferred track N_{comp} (see section 4.6). As is shown in figure 4.14, $N_{\mathrm{comp}} = 1$ for the majority of the badly reconstructed events, while it can be as large as 9 for well reconstructed events; in that case all of the starting points have resulted in the same track.

We have shown here that these two variables can be used to select well reconstructed muons from badly reconstructed up-going muons. In chapter 5 the same parameters will be used to reject the background of wrongly reconstructed atmospheric muons, which form a more dangerous background than up-going muons.

4.7.2 Error estimates

Besides estimates of the track direction, error estimates are provided by the reconstruction program. In general the $1(2)\sigma$ confidence intervals consist of the part of parameter space where $\log(L) - \log(L^{max}) < 1/2$ (2), where L^{max} is the maximum value the likelihood function obtained with the fit. Under the assumption that the likelihood function near the fitted maximum follows a multivariate Gaussian distribution, the error covariance matrix $\mathbf{V}$ can be obtained from the second derivatives of the likelihood function at the

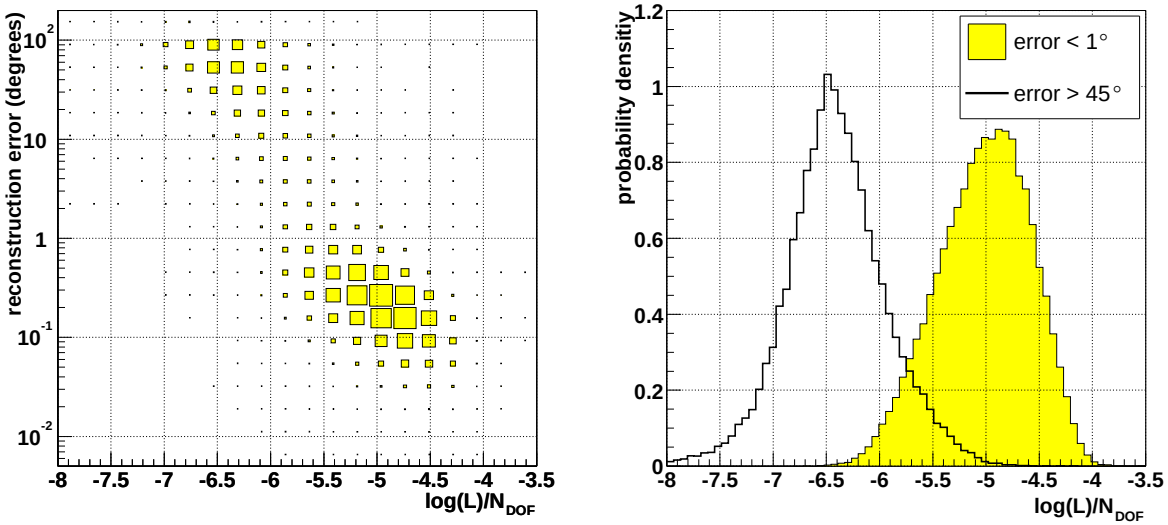

Figure 4.13: *Left: Reconstruction error vs. the value of the likelihood per degree of freedom* $\log(L)/N_{\mathrm{DOF}}$. *Right: The distribution of* $\log(L)/N_{\mathrm{DOF}}$ *for well reconstructed events (error* $< 1°$*) and for badly reconstructed events (error* $> 45°$*).*

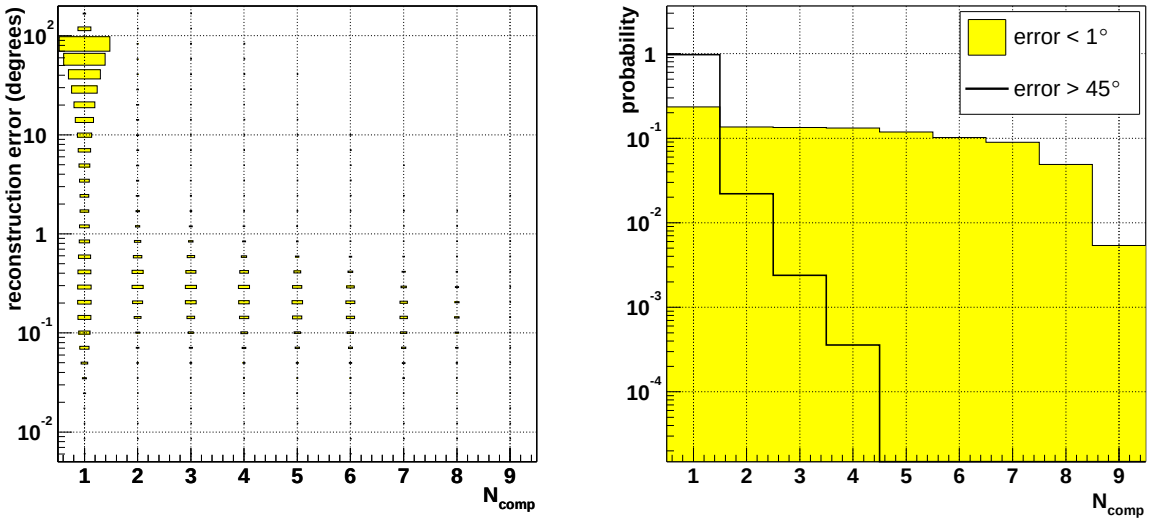

Figure 4.14: *Left: Reconstruction error vs. the value of* N_{comp}. *Right: The distribution of* N_{comp} *for well reconstructed events (error* $< 1°$*) and for badly reconstructed events (error* $> 45°$*).*

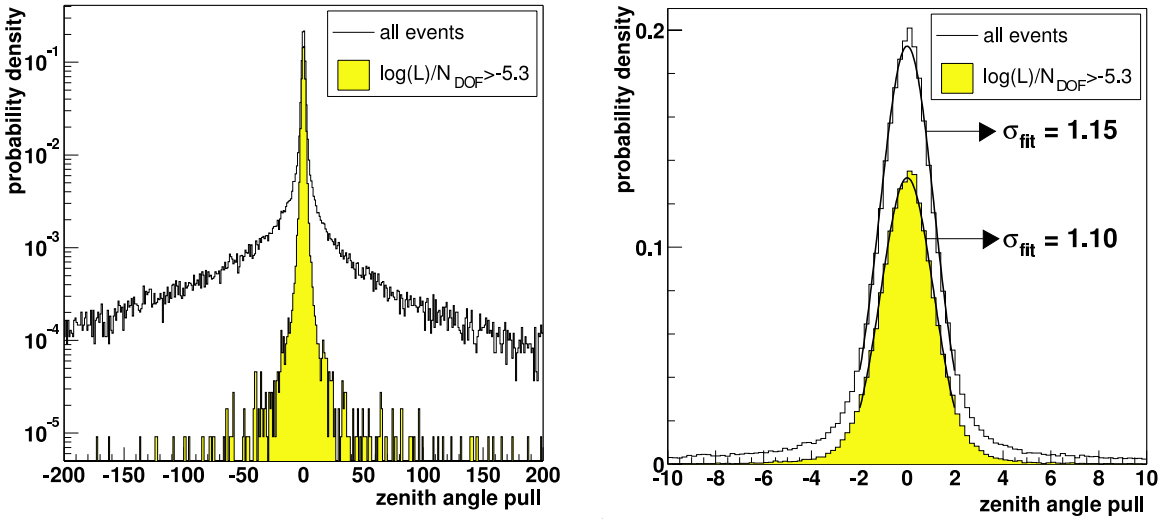

Figure 4.15: *Pull distribution for the zenith angle. The right plot is a close up of the central peak. Distributions are shown for all events and for selected events. The normalisation of the latter distribution reflects the selection efficiency.*

fitted maximum:

$$[\mathbf{V}^{-1}]_{ij} = -\frac{\partial^2 \log(L)}{\partial x_i \partial x_j} \tag{4.19}$$

where $\mathbf{x}$ is the vector of track parameters : $\mathbf{x} = (p_x, p_y, p_z, \theta, \phi)$. In particular, we will use the estimated error on the zenith and azimuth angles: $\hat{\sigma}_\theta$ and $\hat{\sigma}_\phi$ respectively.

The ratio of the true error on a variable and the error estimate is referred to as the pull. The expectation value of the pull is zero, since the estimate of the parameters are symmetrically distributed around the true value. The properties of ML estimators ensure that, in the limit of an infinite amount of data, the estimates are normally distributed around the true values. This means that the pull distribution should be Gaussian with a width $\sigma = 1$.

The distribution of the zenith angle pull (i.e. $(\hat{\theta} - \theta)/\hat{\sigma}_\theta$) is shown in figure 4.15. While the distribution is strongly peaked at zero, large tails are present, consisting of events with unreliable error estimates. These can occur when the reconstruction algorithm has converged to a local maximum. Therefore, the pull distribution is also shown for events with $\log(L)/N_{\mathrm{DOF}} > -5.3$. This selection improves the pull distribution significantly, which means that a large number of the events with incorrect error estimates are rejected. After this quality cut, the pull distribution is approximately Gaussian (although tails are still present). When fitted in the interval (-2, 2), the σ of the pull distribution is 1.10, which is in reasonable agreement with the expected value of 1. The pull distribution for the azimuth angle is shown in figure 4.16. The same features as the pull distribution of the zenith angle can be distinguished.

The estimate of the error on the direction of the reconstructed muon track, $\hat{\alpha}_\mu$, is

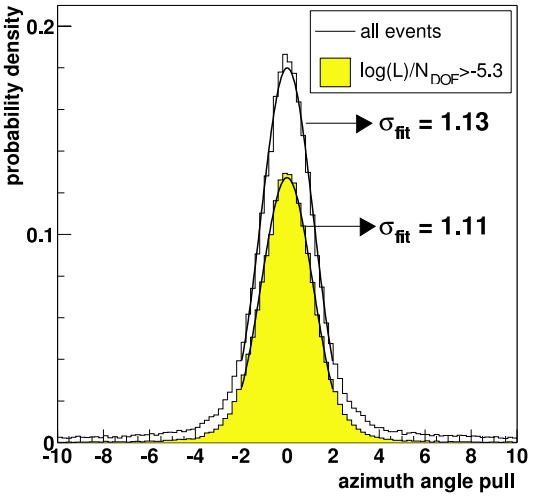

Figure 4.16: *Pull distribution for the azimuth angle for all events and for selected events.*

obtained from $\hat{\sigma}_\theta$ and $\hat{\sigma}_\phi$ as follows:

$$\hat{\alpha_\mu} = \sqrt{\sin^2(\hat{\theta})\hat{\sigma}_\phi^2 + \hat{\sigma}_\theta^2}. \tag{4.20}$$

The distribution of the quantity $\alpha_\mu/\hat{\alpha_\mu}$ is shown in figure 4.17. In the case of uncorrelated Gaussian errors, the distribution of this quantity should be proportional to $\alpha_\mu/\hat{\alpha_\mu} e^{-(\alpha_\mu/\hat{\alpha_\mu})^2}$. The distribution is described reasonably well by this function, although the tail is more pronounced, which is not surprising since tails are also present in the pull distributions for θ and ϕ.

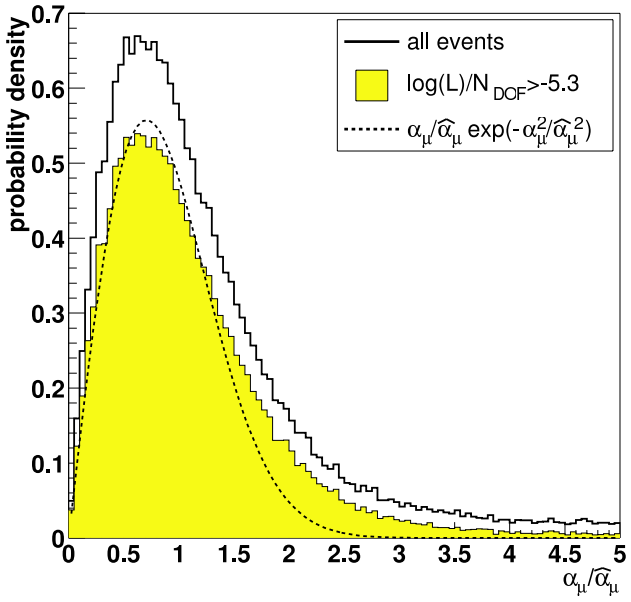

Figure 4.17: *Distribution of $\alpha_\mu/\hat{\alpha_\mu}$ for all events and for events with a high value of the likelihood. Also shown is the theoretical expectation for this distribution in case the errors are uncorrelated and Gaussian. The normalisation of this function is chosen so that it coincides with the solid histogram.*

4.8 Energy reconstruction

The algorithm used for the estimation of the energy is explained in detail in [38] and will be summarised here. As discussed in section 5, the muon energy loss due to pair production and bremsstrahlung increases strongly with energy. The amount of light emitted by the electro-magnetic cascades resulting from these processes can be used as a measure for the muon energy loss and thus for the muon energy.

The average energy lost by the muon per unit track length is estimated from the sum of the amplitudes of the hits (A^{tot}). Only hits with an amplitude larger than 2.5 p.e. are taken into account, since they originate predominantly from electro-magnetic cascades.

The information on the track direction and position that is provided by the previously described track reconstruction algorithm is used to estimate the acceptance of the detector, which is used to correct the estimate of $\frac{dE}{dx}$:

$$\left\langle \frac{dE}{dx} \right\rangle = A^{\text{tot}} l_{\mu}^{-1} \left(\frac{1}{N_{\text{PMTs}}} \sum_{i=1}^{\text{PMTs}} \frac{f_{\text{ang}}(a_i)}{b_i} e^{-b_i/\lambda^{\text{abs}}} \right)^{-1}, \tag{4.21}$$

where b_i is the distance traveled by a photon when it travels from the reconstructed track to the PMT, $f_{\text{ang}}(a)$ is the acceptance of the OM, which depends on the angle of incidence of the photon (see figure 3.10). The absorption length, λ^{abs}, is taken at a fixed wavelength of 475 nm (see figure 3.7). Finally l_{μ} is the 'observable track length', which is defined as the length of the muon track that lies within a cylinder around the instrumented volume. The dimensions of the cylinder are defined by the dimensions of the instrumented volume extended by a distance of 2 $\times \lambda^{\text{abs}}$.

Figure 4.18(left) shows the estimated $\frac{dE}{dx}$ as a function of the muon energy. The figure resembles the curves of the average muon energy loss shown in figure 3.4. From the estimate of $\frac{dE}{dx}$, the muon energy is determined using an empirical function, which is also shown in the figure. This function does not extend below $E_{\mu} = 100$ GeV. For muons below this energy $\frac{dE}{dx}$ is almost independent of the muon energy. If the estimate of $\frac{dE}{dx}$ is smaller than the value corresponding to $E_{\mu} = 100$ GeV, the muon energy is not reconstructed. A scatter plot of the reconstructed muon energy as a function of the true muon energy is shown in figure 4.18(right). In section 5.2.4 we will say a bit more about the performance of the energy reconstruction.

4.9 Outlook and conclusion

Although the reconstruction algorithm that was presented in this chapter performs well, there is still room for further improvement. A better starting point for the final fit would improve the final results. The method of choosing starting points for the fit could be improved if the positions of the local maxima in the likelihood function are better understood. Furthermore, there are other possibilities for the function $g(r)$ used by the M-estimator, some of which may perform better than the present one. The pointing accuracy can be improved by making the PDF of the time residual of the signal hits dependent on the distance traveled by the photon. The PDF will be peaked if the distance is small, but will be smeared for larger distances due to light scattering and dispersion. Finally,

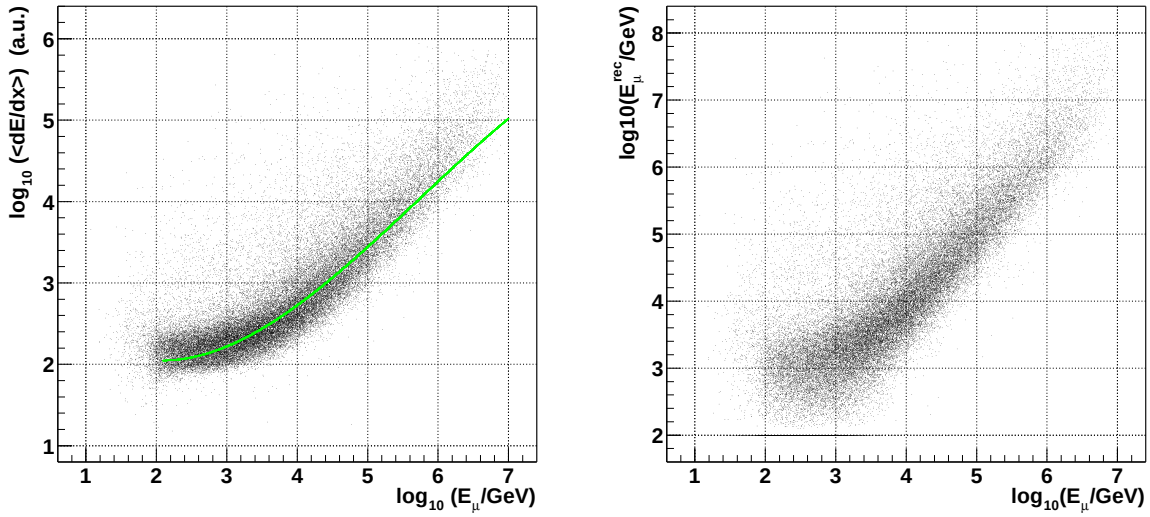

Figure 4.18: *Left: Estimate of* $\frac{dE}{dx}$ *(up to an arbitrary constant) as a function of the simulated muon energy. The empirical function which is used to convert the estimate of* $\frac{dE}{dx}$ *to the estimate of the muon energy is shown as the grey line. Right: Reconstructed muon energy as a function of the true muon energy. The data in the figures corresponds to events where the muon direction was reconstructed within* 1° *from the true direction.*

the energy of the muon could be taken into account, since the PDF of the signal hits broadens with energy (due to the larger contribution of hits from secondary electrons), but also because the relative contribution of background hits depends on the energy.

To conclude, we mention that the track reconstruction algorithm that was described here has been used for various studies of the expected physics potential of ANTARES [38, 73, 74, 75] and of possible future km^3-scale neutrino telescopes [76].

Chapter 5

Background rejection and detector performance

An important potential background for neutrino astronomy is formed by atmospheric muons that are reconstructed as upward-going. In this chapter, selection criteria are presented that serve to reject this background to an acceptable level. The remaining background consists of atmospheric neutrinos and is largely irreducible since both signal and background consist of upward-going neutrinos, which are only distinguishable by their energy spectrum.

After the event selection criteria have been established, the resulting detector acceptance and angular resolution will be presented in section 5.2.

5.1 Event selection

In chapter 6, the sensitivity of ANTARES to detect point sources of cosmic neutrinos will be studied. The method that will be used for this does not require a-priori optimisation of the signal to background ratio, but is expected to be near optimal when the efficiency for signal events is high. Thus, the event selection criteria presented in the present chapter do not serve to optimise the signal to background ratio. Instead, they are primarily used to reject the background from atmospheric muons to a level where it is negligible compared to the background from atmospheric neutrinos.

5.1.1 Signal and background

For a point source search, the signal consists of neutrino events with an accurately reconstructed direction. In order to estimate the selection efficiency for useful signal events, we define a 'well reconstructed event', somewhat arbitrarily[1], as an event that is reconstructed with a direction within 1° of the true neutrino direction. The energy spectrum of signal neutrinos is assumed to be proportional to E^{-2}.

The atmospheric neutrino background is simulated using the models of the atmo-

[1]The value of 1° can, for example, be compared to the optimal bin size of $\sim 1^\circ$ that will be found in section 6.2.

sample	A	B
number of generated primaries	3.6×10^9	150×10^6
equivalent data-taking time	8 hours	7.4 days
minimal primary energy per nucleon	1 TeV	200 TeV
minimal muon multiplicity @ detector	1	2
events reaching detector	7.9×10^6	6.8×10^6
reconstructed events	330×10^3	865×10^3
reconstructed as upward-going	54×10^3	82×10^3

Table 5.1: *Characteristics of the two samples of simulated atmospheric muons.*

spheric neutrino flux discussed in section 3.5.3. The method to simulate the atmospheric muon background was discussed in section 3.5.2. As was mentioned there, only a limited number of atmospheric muons could be simulated. For this study, two different samples of simulated atmospheric muons were used. The characteristics of the event samples are summarised in table 5.1. The first sample, sample A, is a full (minimum bias) simulation corresponding to eight hours of data taking. This sample will be used to estimate the contribution of the atmospheric muon flux to the background. Sample B consists of multi-muon events, where only high-energy (> 200 TeV) primary nuclei have been simulated. Such events may be expected to give the largest contribution to the background. Due to the relatively low flux of high energy CR, sample B represents a longer period of data taking: about 7.4 days. In section 5.1.3, sample B will be used to cross-check the results obtained with sample A.

5.1.2 Selection criteria

As a first step, the following three selection criteria are applied:

cut 1: The muon must be reconstructed as upward-going: $\hat{\theta} > 90^\circ$.

cut 2: The energy of the event must be reconstructed.

cut 3: The estimate of the error on the muon direction must be smaller than 1°: $\hat{\alpha}_\mu < 1^\circ$.

The first of these cuts is needed to reject the background from (well reconstructed) down-going muons. The latter two criteria cause an inefficiency of 6.5%, while the background is reduced by a factor 6.6.

While these selection criteria already reject a large fraction of the background, about 25000 atmospheric muon events per day remain. They are rejected using two variables that were introduced in section 4.7.1: the log-likelihood per degree of freedom $\log(L)/N_{\mathrm{DOF}}$ and the number of compatible solutions, N_{comp}, found by the reconstruction program. Figure 5.1(left) shows the distribution of $\log(\mathrm{L})/N_{\mathrm{DOF}}$ for signal and background events for different values of N_{comp}. For high values of N_{comp}, the cut on $\log(L)/N_{\mathrm{DOF}}$ can be placed at a somewhat lower value. This is accomplished by cutting on a dedicated variable Λ, which combines N_{comp} and $\log(L)/N_{\mathrm{DOF}}$:

$$\Lambda \equiv \frac{\log(\mathrm{L})}{N_{\mathrm{DOF}}} + 0.1(N_{\mathrm{comp}} - 1). \tag{5.1}$$

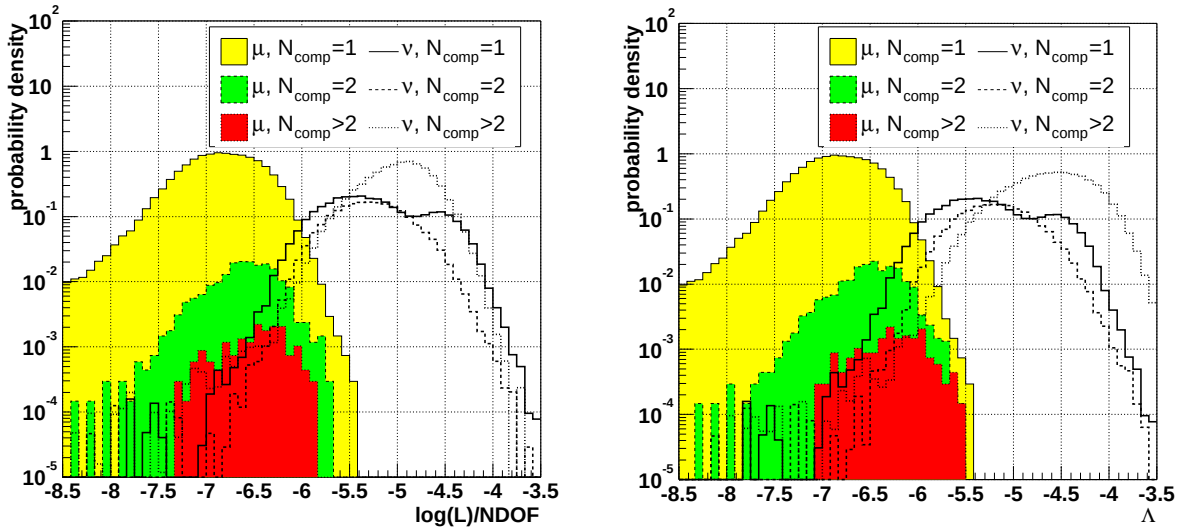

Figure 5.1: *Left: Distribution of* $\log(L)/NDOF$ *for different values of* N_{comp} *for signal and background events. Right: Distributions of the variable* Λ *for different values of* N_{comp} *for signal and background events. Sample B was used for this figure because of the higher statistics available for large values of* Λ*.*

In figure 5.1(right), the distribution of Λ is shown for different values of N_{comp}. Comparison with figure 5.1(left) shows that the distributions differ only slightly. Nevertheless, the overall separation of signal and background is somewhat better when using Λ as discriminating variable.

Figure 5.2 shows the number of background events that remain after a cut on Λ as a function of the value of the cut. For $\Lambda \gtrsim -5.6$, the dominant background is formed by atmospheric neutrinos. However, the contribution of the atmospheric muon background in this region can not be accurately determined because of the low statistics in the event sample: the simulated sample of atmospheric muons is equivalent to only 8 hours of data taking. In order to estimate the number of atmospheric muon events passing the cut, the distribution in figure 5.2 is extrapolated using an exponential function that was fitted to the tail. In this way, we estimate that roughly one event per day with $\Lambda > -5.3$ is produced by atmospheric muons that are reconstructed as upward-going. This number can be compared to the 10.0 events produced by atmospheric neutrinos. Thus, for a cut at $\Lambda = -5.3$, it is a reasonable approximation to neglect the contribution of atmospheric muons to the total background; especially because this contribution is of the same order of magnitude as the systematic uncertainty on the atmospheric neutrino flux (see section 3.5.3). The last selection cut was thus chosen to be:

cut 4: The variable $\Lambda > -5.3$.

The effect of the various selection criteria on the signal and background is summarised in table 5.2. The final signal selection efficiency is 73.6%, while the atmospheric muon background is reduced by more than a factor 10^5.

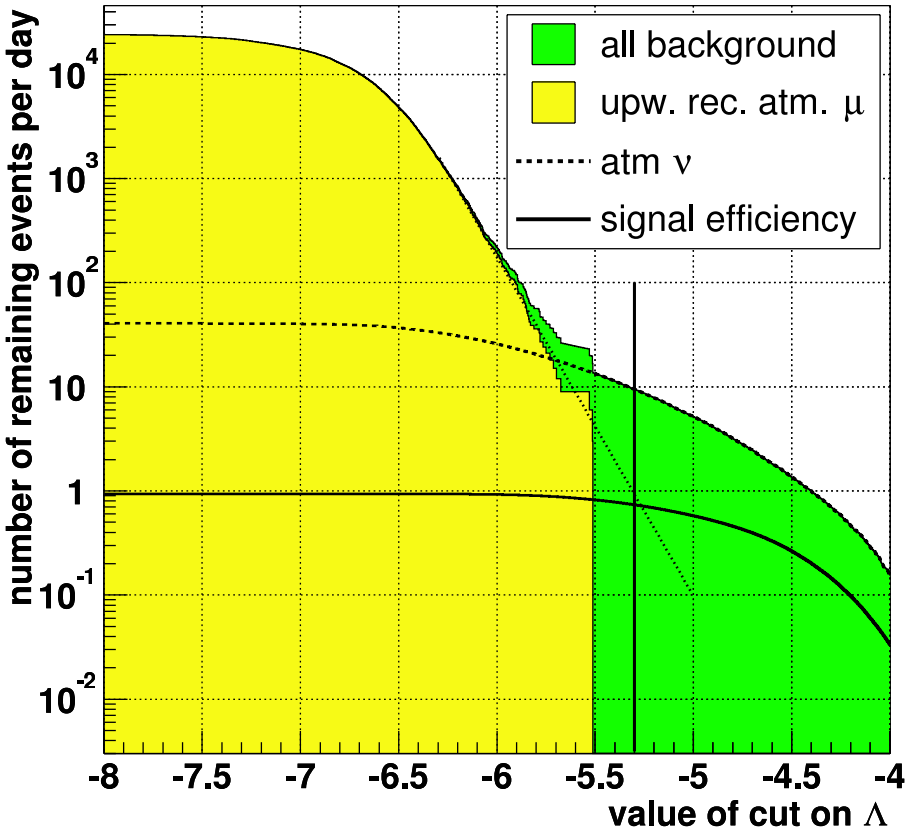

Figure 5.2: *Number of background events left as a function of the cut value for* Λ*. The background consists of atmospheric neutrinos and atmospheric (multi-)muons passing selection criteria 1, 2 and 3 (see text). The efficiency for signal events is also shown. The vertical line indicates the value where the cut was placed.*

no.	cut	μ^{atm}/day	ν^{atm}/day	ϵ_{sig}
1	upward rec.	163152	109.4	$\equiv$100%
2	$\hat{E}_\mu$	44748	51.05	95.8%
3	$\hat{\alpha_\mu} < 1$	24591	40.66	93.5 %
4	$\Lambda > -5.3$	$\sim$1	10.0	73.6 %

Table 5.2: *Number of remaining background events and signal efficiency after successive application of the various selection criteria.*

5.1.3 Cross-check with high energy multi-muons

As was already mentioned, sample B consist of a sub-set of all muon events; namely multi-muon events with a high primary energy above 200 TeV/nucleus. Such events make up roughly 10% of all atmospheric muon events that pass selection criteria 1, 2 and 3 discussed in the previous section.

As can be seen in figure 5.3, higher values of Λ occur more frequently in this type of event: they make up roughly 20% of the events with $\Lambda > -6$ (for higher values of Λ, this fraction cannot be determined accurately due to the lack of statistics in sample A.)

Like sample A, sample B contains no events that pass the selection criterion $\Lambda > -5.3$. Extrapolation of the distribution of Λ yields an estimate of about 0.1 event/day resulting from events of the type simulated in this sample[2]. Since this type of event is responsible for only $\sim$ 20% of the total rate, this estimate is in rough agreement with the result obtained using sample A (1 event per day).

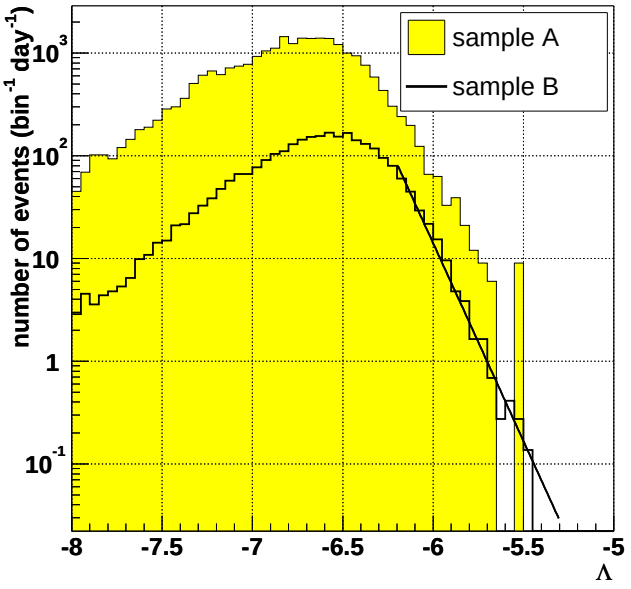

Figure 5.3: *Distributions of Λ for minimum bias atmospheric muon events (sample A) and for multi-muon events with primary energy above 200 TeV/nucleon (sample B). The line is a fit, which is used to extrapolate the distribution.*

Perhaps more important than the number of selected atmospheric muons, is the observation (from figure 5.2) that an additional reduction of this background by a factor of 10 could be achieved at the cost of an additional decrease of the efficiency of (only) 20%. This is also confirmed by the analysis of sample B.

5.2 Detector performance

In this section, the detector acceptance and angular resolution obtained after applying the selection criteria presented in the previous section are discussed.

[2]Alternatively, the observation that no events pass the selection cuts, can be used to set a 90% CL upper limit of 2.3 events in 7.4 days and hence 0.31 events per day.

5.2.1 Effective area for muons

The sensitivity of the detector to a flux of muons can be represented as an effective area, which is defined as the ratio between the rate of detected events $R_{\text{det}}(E_\nu, \theta, \phi)$ and the muon flux $\Phi_\mu(E_\nu, \theta, \phi)$:

$$A_\mu^{\text{eff}}(E_\nu, \theta, \phi) \equiv \frac{R_{\text{det}}(E_\nu, \theta, \phi)}{\Phi_\mu(E_\nu, \theta, \phi)} \tag{5.2}$$

A few remarks about this definition are in order:

- R_{det} in (5.2) is the rate of detected events, but the definition of a 'detected event' depends on the situation. One may, for example determine the effective area for all events that are reconstructed or for all events that are selected to be used in a particular analysis. The value of the effective area thus depends on the stringency of the selection criteria. The same is true for the neutrino effective area (section 5.2.2) and the angular resolution (section 5.2.3).

- At energies below about 1 TeV, a significant number of the interactions occur inside the detector volume. For these energies, the number of detected events is not uniquely determined by the muon flux. There is an additional dependence on the flux of neutrinos that produces the muon flux. For this reason, the muon effective area is preferably presented as a function of the neutrino energy.

The effective area for muons, averaged over all upward directions, is shown in figure 5.4. For high energies, the muon effective area exceeds the geometrical detector area (defined as the average projection of a cylinder which fits tightly around all OMs). At these energies, muons that pass the detector at some distance can be reconstructed and contribute to the effective area.

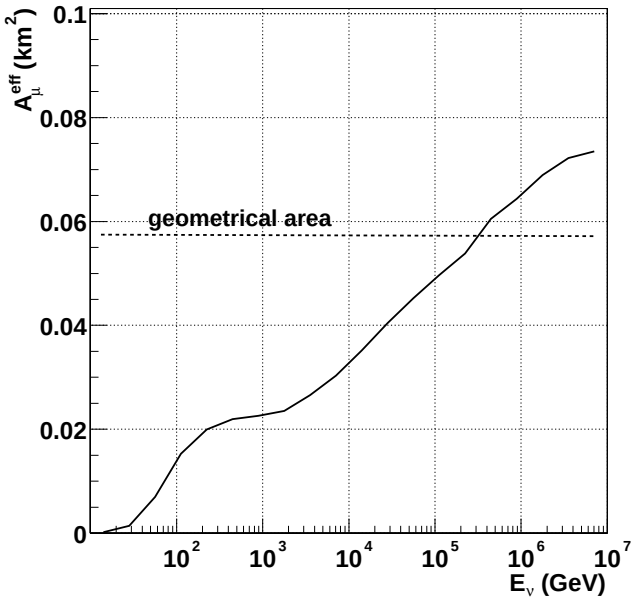

Figure 5.4: *The effective area for muons, averaged over all upward directions. The average geometrical surface of the detector is also shown.*

5.2.2 Effective area for neutrinos

The effective area for neutrinos can be used to calculate directly the event rate due to a flux of neutrinos $\Phi_\nu(E_\nu, \theta, \phi)$. It is defined as

$$A_\nu^{\text{eff}}(E_\nu, \theta, \phi) \equiv \frac{R_{\text{det}}(E_\nu, \theta, \phi)}{\Phi_\nu(E_\nu, \theta, \phi)}, \tag{5.3}$$

where $\Phi_\nu(E_\nu, \theta, \phi)$ is defined as the flux of neutrinos before they enter the Earth. In addition to the detection efficiency, the neutrino effective area takes into account the interaction probability, the probability that the neutrino survives its journey through the Earth and the energy loss of the muons. Like the muon effective area, the value of the neutrino effective area depends on the event selection criteria.

The angle averaged effective area for neutrinos is shown in figure 5.5 as a function of the neutrino energy. The effective area for three distinct values of the zenith angle is also shown. The strong energy dependence is mostly due to the rise of the cross-section of the neutrino interaction (see section 3.2.1). For vertically upward-going neutrinos, the effective area is suppressed at high energies due to the absorption in the Earth.

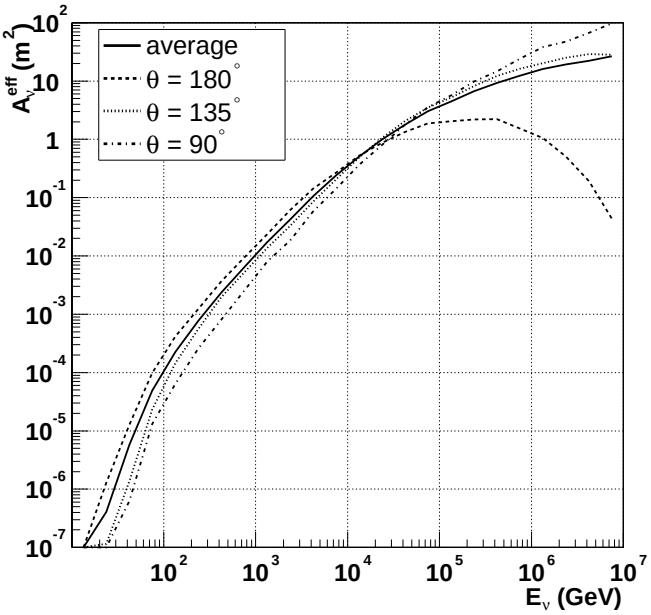

Figure 5.5: *The effective area for neutrinos as a function of the neutrino energy for three different zenith angles θ and the angle-averaged effective area.*

5.2.3 Angular resolution

The angular resolution of the detector depends on the neutrino for two reasons. The scattering angle between the neutrino and the produced muon depends on the neutrino energy (see figure 3.6). Furthermore, high energy muons are usually better reconstructed than low energy ones due to the increased production of Cherenkov light. The distribution of the reconstruction error α_μ is shown in figure 5.6 for a neutrino spectrum proportional to E^{-2}. Also shown is the distribution of the error on the neutrino direction α_ν, which is the angle between the neutrino and the reconstructed muon.

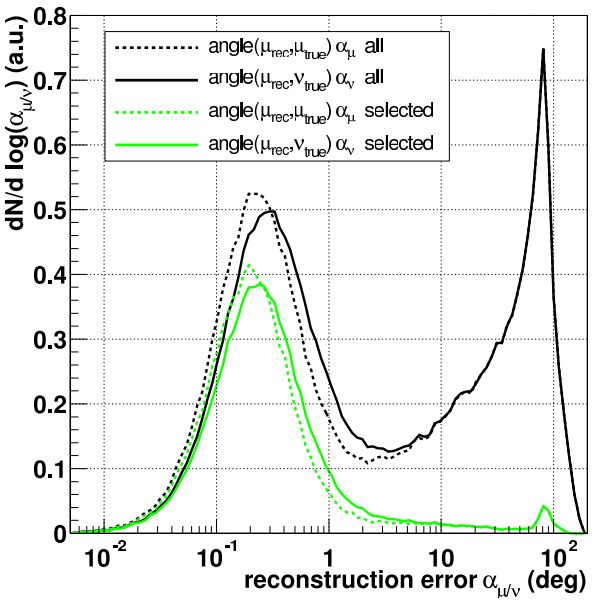

Figure 5.6: *Reconstruction error for an E^{-2} spectrum of neutrinos for all reconstructed events and for selected events. The resolution on the muon direction and the neutrino direction are shown.*

To characterise the overall pointing accuracy of the detector, the median of the reconstruction error is used. The resolution thus obtained is shown in figure 5.7 for both the muon and the neutrino. Below about 10 TeV the resolution on the neutrino direction is dominated by the angle between the neutrino and the muon in the interaction, while above that energy it is limited by the accuracy of the muon reconstruction. At the highest energies, the angular resolution is smaller than 0.2°. For the events produced by a neutrino flux with an energy spectrum proportional to E^{-2}, the median resolution on the neutrino direction is 0.24°.

5.2.4 Response curves

The distribution of the energy of the neutrinos that produce detectable events depends on the energy spectrum. In figure 5.8, the distribution of the neutrino energy is shown for the selected events assuming different neutrino spectra. For an energy spectrum proportional to E_ν^{-2}, the most important energy range is around a few tens of TeV, whereas most of the selected atmospheric neutrino events are due to neutrinos with energies of a few hundred GeV. Also shown in figure 5.8 is the fraction of atmospheric muon-neutrino events remaining after including the effect of neutrino oscillations. In this figure, two-flavour vacuum oscillations with maximal mixing and $\Delta m^2 = 2.5 \times 10^{-3}$ eV^2 have been assumed. The effect of neutrino oscillations on the total number of selected atmospheric neutrino events is roughly 3% and has therefore been neglected in the analysis. The effect of neutrino oscillations on the signal flux was discussed in section 1.2.4.

The distribution of the energy of the muon when entering the detector and of the reconstructed muon energy is shown in figure 5.9 for various neutrino spectra. The muon energy is typically a factor 5 lower than the energy of the parent neutrino, which is mainly due to the muon energy loss during propagation to the detector. The reconstructed energy of the muons is seen to be reasonably accurate for high energy events, as can be expected

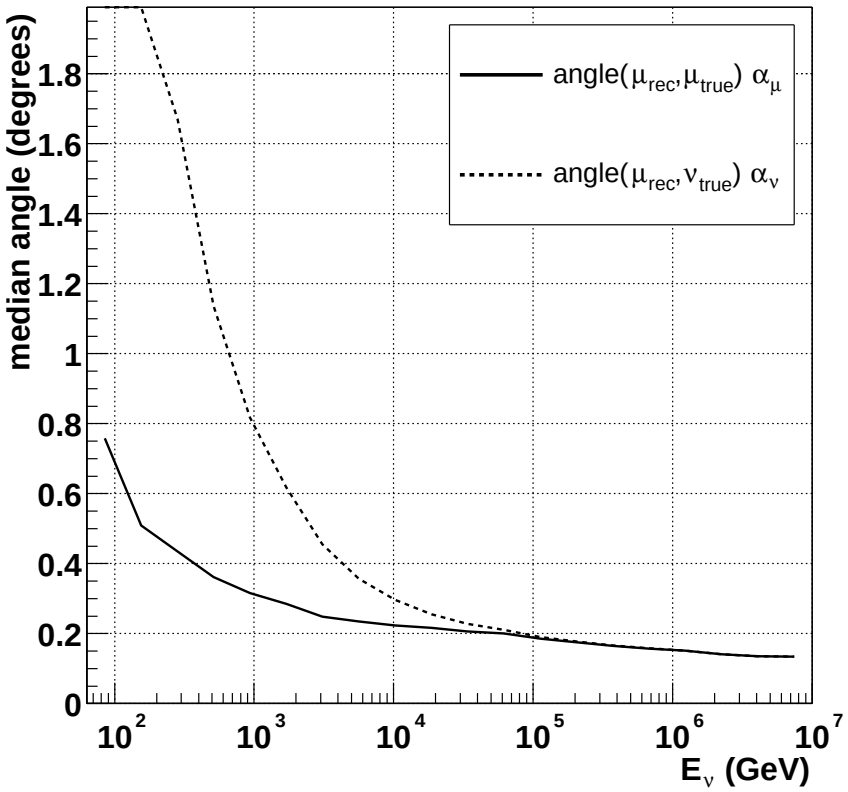

Figure 5.7: *The angular resolution of the detector as a function of the neutrino energy. The plot shows the resolution on the neutrino direction and the resolution on the muon direction.*

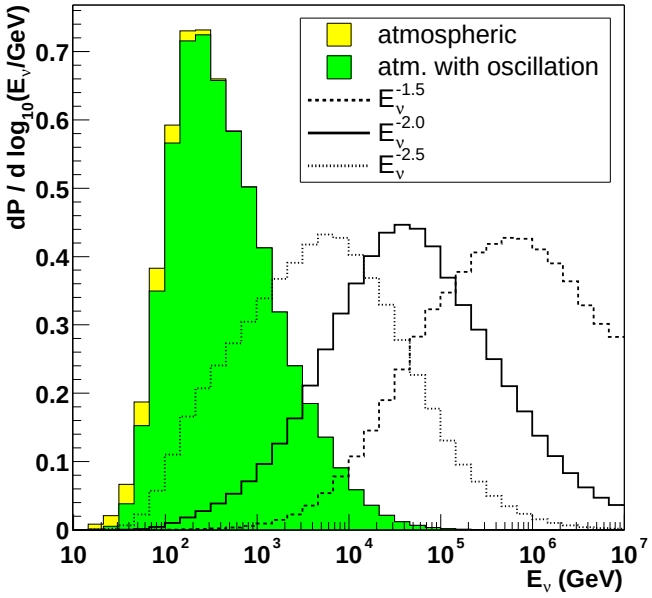

Figure 5.8: *Distribution of the energy of the neutrinos that give rise to selected events in the detector for three different power law spectra and for the atmospheric neutrino spectrum. Also shown is the distribution of the remaining atmospheric neutrino events after inclusion of the effect of neutrino oscillations (this distribution is normalised to the distribution without oscillations).*

from figure 4.18. For low energy events, however, the estimated energy is strongly biased towards higher values. One of the reasons for this bias is that some low energy events are not considered to be 'reconstructed' (see section 4.8); this is also the reason why there are no events with a reconstructed energy below 100 GeV. Furthermore, the energy estimator does not take into account the light from the hadronic shower that may play a role when the interaction occurs inside the instrumented volume. In [38] a set of criteria is suggested that can be used to reject events with badly reconstructed energies. While these cuts were indeed found to reduce some of the bias for low energy events, they also reject about 20% of the well reconstructed events. Since this inefficiency was thought to be more important than the gain from the improved accuracy of the energy reconstruction, this selection was not applied in the analysis.

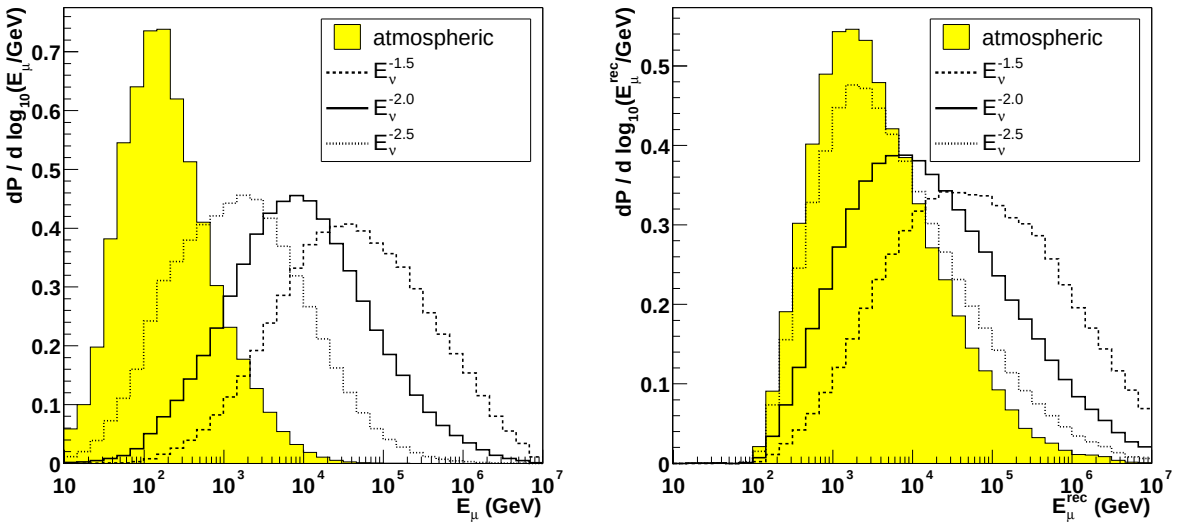

Figure 5.9: *Left: Distribution of the muon energy for the atmospheric neutrino flux and for three different power law spectra. Right: Distribution of the reconstructed muon energy.*

5.2.5 Well reconstructed atmospheric muons

As discussed, atmospheric muon events that are reconstructed as up-going must be rejected. However, atmospheric muons that are well reconstructed could be useful; e.g. for calibration and alignment. In any case, the first physics events seen by ANTARES will be atmospheric muon events.

The distribution of the reconstruction error α_μ for atmospheric muons is shown in figure 5.10. The normalisation of the figure corresponds to one day of data-taking. The distribution is also shown for the events remaining after application of the selection criteria discussed in section 5.1.2 (with the exception of cut 1).

Compared to the performance for up-going muons (figure 5.6), the selection efficiency

is much lower, but the selected events are reconstructed with roughly the same accuracy. Despite the low selection efficiency, 6800 events per day will pass the selection criteria. Of these events, 4000 (490) are reconstructed with an error smaller than 0.5° (0.1°).

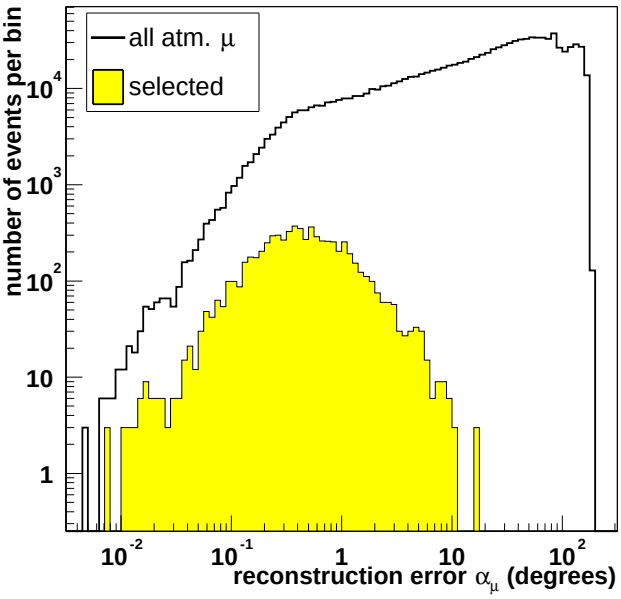

Figure 5.10: *Distribution of the reconstruction error α_μ for a one-day sample of atmospheric muons for all events and for selected events.*

Chapter 6

Point source searches

In this chapter, a new method, called the Likelihood Ratio (LR) method, to search for point-like sources of neutrinos will be described and the resulting sensitivity of the ANTARES detector for point sources will be presented. The method will be described in section 6.3 and the results are compared to the expected sensitivity[1] of binned methods, which are discussed in section 6.2. Finally, in section 6.6, the sensitivity of ANTARES will be compared to a number of flux predictions and to results obtained by other experiments.

6.1 Introduction

The presence of a point source of neutrinos could be indicated by an excess of events from a certain direction in the sky. On the other hand, such an excess can be due to atmospheric neutrinos that, by coincidence, seem to come from the same point in the sky.

After a period of data taking, a set of reconstructed and selected events will have been collected. The reconstruction algorithm provides estimates for the zenith and azimuth angles $\hat{\theta}$ and $\hat{\phi}$. Furthermore, the time of detection t is recorded. From the reconstructed neutrino direction and the detection time of the event, the corresponding celestial coordinates are calculated (standard software is used for this [78]). We use 'equatorial' coordinates: right ascension α^{ra} and declination δ. As an example, the celestial coordinates of the events in a one-year sample of selected atmospheric neutrino events are shown in figure 6.1. Due to the geographical location of the detector, the part of the sky with declinations higher than 48° is always above the horizon and is thus never observed by ANTARES. In contrast, the part of the celestial sphere with declinations below −48°, is always visible. The region in between is visible during some fraction of the day.

The sensitivity of the search depends on the assumptions that are made about the source. Throughout this chapter, two cases will be considered:

Full sky search: In a full sky search, a source of neutrinos is searched for anywhere in the observable sky.

Fixed point search: In this case, we try to determine whether there is a source of

[1] The term 'sensitivity' is sometimes defined as the average upper limit an experiment can set [77]. Here the term is used, in general, as 'the capability to make a discovery'.

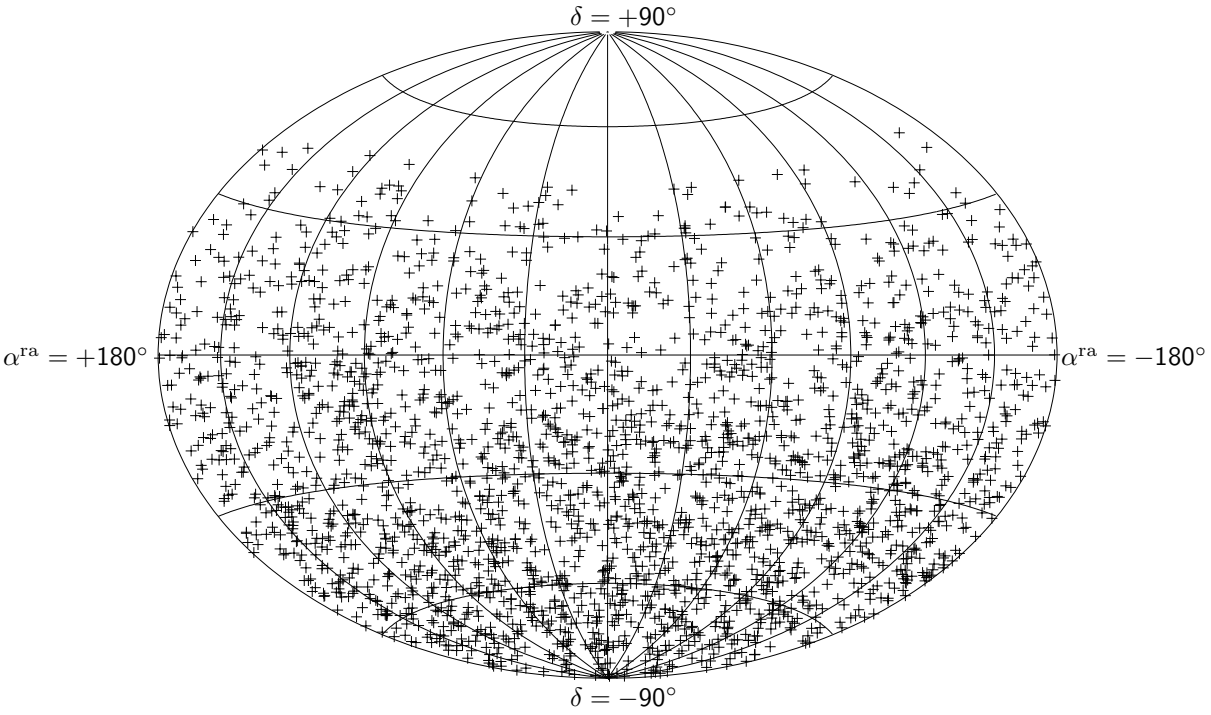

Figure 6.1: *Skyplot showing the reconstructed declination and right ascension. The number of events corresponds to 1 year of data taking.*

neutrinos at one of a number of predefined locations in the sky. The candidate source locations could, for example, correspond to known gamma ray sources, which may be expected to produce neutrinos.

Although it is more restrictive, a fixed point search is more sensitive than a full sky search, since the probability that fluctuations in the background produce an excess is smaller.

6.2 Binned methods

One way to conduct a full sky search for point sources is to divide the observable sky into square-like bins and to look for a bin which contains an excess of events. For a fixed point search, a similar method can be used, where one counts the number of events that fall within circular bins, which are centred on the coordinates of the candidate sources. In this section, the discovery potential of these methods will be estimated for a point source with an E^{-2} energy spectrum. The objective of this exercise is to verify the validity and to quantify the improvement in performance of the more elaborated likelihood ratio method, which will be presented in section 6.3. A more detailed study of the performance of ANTARES using binned methods can be found in [79].

The size of the bins will be chosen such that the probability of discovering a point source at the $3(5)\sigma$ Confidence Level (CL) is maximal. This probability is related to the

number of background events in a bin, which is given by

$$N_{\mathrm{bg}} = R^{\mathrm{bg}}(\delta)\Omega_{\mathrm{bin}}\Delta T, \tag{6.1}$$

where Ω_{bin} is the bin size, ΔT is the observation time, $R^{\mathrm{bg}}(\delta)$ is the rate of background events per unit solid angle, which depends on the declination δ of the bin and which is shown in figure 6.2. ΔT is the observation time, which we take to be one year.

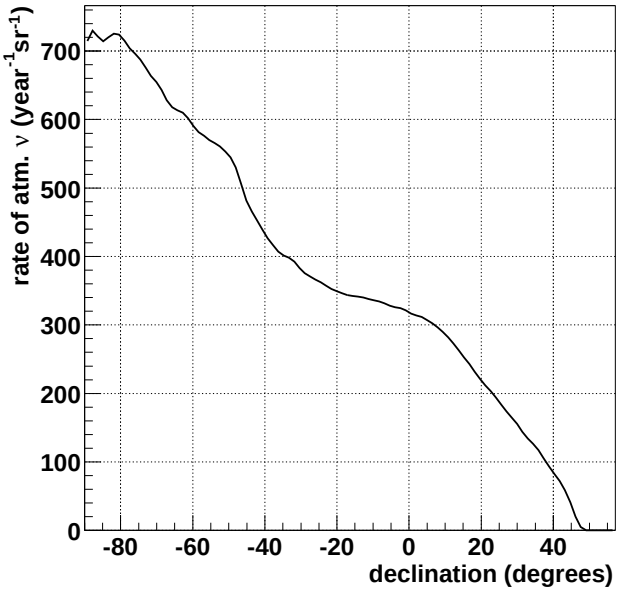

Figure 6.2: *Rate of selected atmospheric neutrino events as a function of declination.*

If no signal is present, the probability of observing at least N_c events is given by the sum of the Poisson probabilities:

$$P(N \geq N_c | \langle N \rangle = N_{\mathrm{bg}}) = \sum_{k=N_c}^{\infty} \frac{N_{\mathrm{bg}}^k e^{-N_{\mathrm{bg}}}}{k!}. \tag{6.2}$$

In order to discover a signal at, for example, $3(5)\sigma$ CL, the probability of observing N or more events in any of the bins must be less than $2.7 \times 10^{-3}(5.7 \times 10^{-7})$ in the background-only case. This can, to good approximation, be translated into the following requirement on a single bin:

$$P(N \geq N_c | \langle N \rangle = N_{\mathrm{bg}}) \leq \frac{2.7 \cdot 10^{-3}}{N_{\mathrm{bins}}}, \tag{6.3}$$

where N_{bins} is the total number of bins.

The value of N_{bins} depends on the type of search. In the case of a fixed point search, N_{bins} is simply the number of candidate sources under consideration. For a full sky search, the whole observable sky is filled with bins. In this case, the bin size is a function of the declination and the total number of bins is given by

$$N_{\mathrm{bins}} = 2\pi \int_{-90^\circ}^{45^\circ} \Omega_{\mathrm{bin}}(\delta)^{-1} d\sin(\delta), \tag{6.4}$$

where the search region is defined by all declinations from $-90°$ to $+45°$, which corresponds to a total solid angle of about 10.7 sr.

The number of events needed in a bin for a $3(5)\sigma$ discovery, N_c, may now be calculated as a function of the bin size for each value of the declination. As an example, the result for a full sky search is shown as the dashed line in figure 6.3 for a source at a declination of $-81°$. This arbitrarily chosen value of the declination will be used throughout this chapter for various examples. It is clear that a small (large) bin size requires a small (large) number of events.

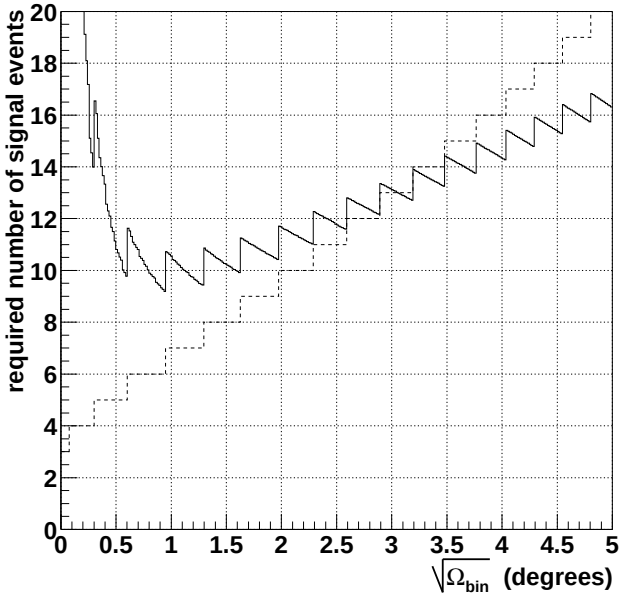

Figure 6.3: *Dashed line: The number of events N_c required in a bin at $\delta = -81°$ for a 3σ discovery as a function of the bin size. Solid line: Mean of the total number of signal events N^c_{sig} required from a point source to have a 50% probability of detection (at 3σ CL).*

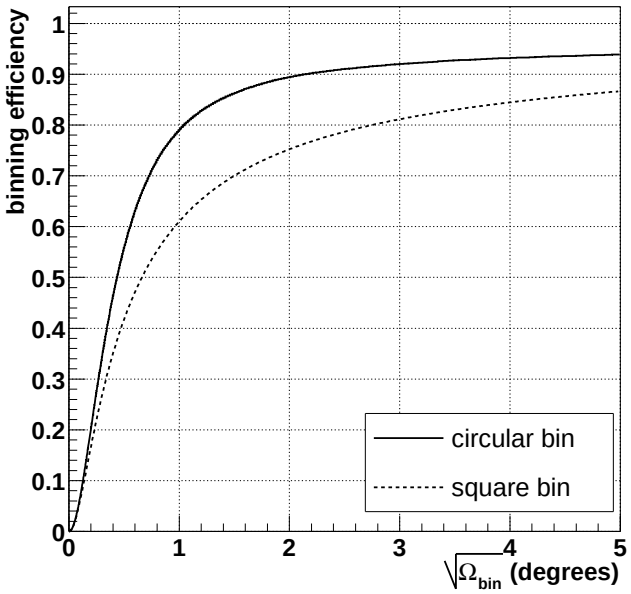

Figure 6.4: *Average binning efficiency for a circular bin, which is centred on the true source coordinates, and for a square bin with the source at a random position within the bin.*

In order to compare these results to the results from the LR method, we calculate the expectation value of the number of observed events in the bin $\langle N \rangle_c$ so that there is a 50% probability that the actual number of observed events is at least N_c. The relation between the two follows from Poisson statistics[2].

The expectation value of the number of events in a bin needed for a discovery is the sum of the expectation value of the number of background events in the bin and the expectation value of the total number of signal events observed from a source $N^c_{\rm sig}$, multiplied by the binning efficiency ϵ:

$$\langle N \rangle_c = N_{\rm bg}(\Omega_{\rm bin}) + \epsilon(\Omega_{\rm bin}) N^c_{\rm sig}. \tag{6.5}$$

The binning efficiency is defined as the probability that the reconstructed coordinates of an event lie within the bin if the coordinates of its astrophysical source are contained in it. This quantity has been calculated for a source with an E^{-2} spectrum and is shown in figure 6.4 for the case of a fixed point search, where a circular bin is centred on the coordinates of the source, and for a full sky search, where the source is located at a random position within a square-like bin. In the latter case, the binning efficiency is reduced, because the source may be located close to the edge of the bin.

Equation 6.5 is used to calculate the number of signal events a source must produce to yield a 50% chance of a discovery. For the full sky search, the result is shown in figure 6.3 as a function of the bin size. The discontinuities in the figure correspond to changes in the value of N_c, which occur at values of $\Omega_{\rm bin}$ where the inequality in equation 6.3 is an equality. In between the discontinuities, the number of required events decreases with $\Omega_{\rm bin}$ due to the increase in binning efficiency.

The optimal bin size is determined from figure 6.3 as the value at which the expectation value of the number of required signal events is smallest (i.e. where the flux needed for a discovery is lowest); this occurs just before a step[3]. From the figure one sees that if the bins are chosen to be optimal for a 3σ discovery, the number of signal events needed is about 9.1 for a source at a declination of $-81°$. The optimal bin size is about $0.95° \times 0.95°$ for this declination. At higher declination, where there is less background, the optimal bin sizes are somewhat larger. The corresponding binning efficiency is 60%. When optimised for a discovery at 5σ CL, the bin size is smaller: $0.85° \times 0.85°$.

After the optimal bin size has been determined for each value of the declination, equation 6.4 is used to re-calculate the total number of bins. This procedure is repeated (a few times) until the result has converged. The result is a configuration of bins for which equation 6.3 is satisfied for each bin.

The final result is the discovery potential, which we have defined as the number of signal events needed for a 3σ discovery in 50% of the experiments. This quantity is calculated as a function of the declination and it will be shown in figures 6.13 (full sky search) and 6.17 (fixed point search), where it will be compared to the results obtained with the LR method.

[2] $\langle N \rangle_c$ is always smaller than N_c; the relative difference is typically less than 10% for the values involved here ($N_c \geq 4$).

[3] At this point we make an assumption that is favourable to the binned method, since in reality, this 'fine-tuning' of the bin size seems not feasible.

6.3 Likelihood ratio search method

6.3.1 Motivation

The binned methods described in the previous sections are well known ways to search for point sources of neutrinos. The motivation to develop a new method is that such methods do not make optimal use of the following pieces of information:

The events outside the bin: In order to reduce the background, the size of the bin is chosen such that a fraction of the signal events falls outside the bin. The information contained in these events is lost.

The distribution of the events within the bin: Not only the number of events in a bin is important, but there is also information in the distribution of the events within the bin. For a fixed number of events, there are still configurations of events which 'look' more like they are the result of a point source than others.

The energy of the events: The reconstructed muon energies are, in general, distributed differently for signal and background events (see figure 5.9). This information can be used, even when the energy spectrum of the signal is not known a priori. Furthermore, the angular resolution varies with energy; high energy events should be close to the source coordinates in order to be compatible with the point source signal, whereas low energy events may have a larger deviation.

The angular error estimate: The accuracy of the reconstructed direction varies from event to event and is described by the error estimates provided by the reconstruction algorithm.

The zenith angle of the events: Typically, binned methods only use the celestial coordinates of the events. The expected number of background events can, however, be estimated most accurately from the zenith angle. Events from a range of azimuth angles contribute to the events at a given declination. Therefore information is lost when using only the celestial coordinates.

The likelihood ratio (LR) method, which will be introduced in the following sections, was developed with the objective to increase the sensitivity by making use of this information. It will be shown that the new method indeed leads to an increase in the sensitivity compared to binned methods.

6.3.2 Hypothesis testing

Searching for point sources involves testing the compatibility of the data with two hypotheses; traditionally the default one is called H_0 and the exceptional one is called H_1. In our case they are H_0: "*Only atmospheric neutrinos are present.*" and H_1: "*In addition to the atmospheric neutrinos, there exists a point source of neutrinos.*".

Testing the compatibility of the data with these two hypotheses is accomplished by computing the value of the so-called test statistic λ(data), which can, in principle, be any function of the data. The idea is to choose the test statistic such that, if H_0 is true, it is

expected to have a different value from the case where H_1 is true. Thus, the value of λ indicates whether the data is more compatible with H_0 or with H_1. The distributions of λ for H_0 and H_1 can be computed (numerically if needed). Using this information, one can define a set of values that is unlikely to contain λ if H_1 is true. This region is called the 'rejection region' ω. If λ lies within the rejection region, hypothesis H_0 is 'rejected' in favour of H_1.

It is possible that λ is contained in the rejection region, even though H_0 is true. In this case H_0 will be wrongly rejected. In our case this means that a discovery is claimed, while in reality there is no source. The probability that this happens can be calculated and is related to the Confidence Level (CL) of the test:

$$1 - \text{CL} \equiv P(\lambda \in \omega | H_0). \tag{6.6}$$

The CL is usually chosen beforehand and it defines the rejection region.

The probability to reject H_0 in favour of H_1 if H_1 is indeed the correct hypothesis is called the 'power' of the test:

$$\text{power} \equiv P(\lambda \in \omega | H_1). \tag{6.7}$$

At a fixed level of significance, the power of the test corresponds to the sensitivity for discovering the signal. It depends on the level of separation of the distributions of the test statistic for H_0 and H_1, as is illustrated in figure 6.5. Searching for point sources with optimal sensitivity is therefore equivalent to choosing the best test statistic, which is the subject of the next section.

6.3.3 Likelihood ratio test statistic

There are many possibilities to choose the test statistic. In the case of a binned method, for example, the test statistic is 'the number of entries in the bin with the highest content'. In the method presented here, the test statistic is defined as the ratio of the probabilities of the data under the assumption that H_1 respectively H_0 is the correct model:

$$\lambda = \log \left[\frac{P(\text{data}|H_1)}{P(\text{data}|H_0)} \right]. \tag{6.8}$$

The corresponding test is called the Neyman-Pearson test, or likelihood ratio test [44, 80]. It has been shown to be the best possible test in case H_0 and H_1 are completely specified. Here, H_0 and H_1 have unknown parameters that need to be measured from the data. In such cases it is customary to use equation 6.8, with the additional requirement that the unknown parameters are chosen such that the probability of the data is maximised:

$$\lambda = \log \left[\frac{P(\text{data}|H_1^{\text{max}})}{P(\text{data}|H_0^{\text{max}})} \right], \tag{6.9}$$

where H_1^{max} is hypothesis H_1 with the (unknown) parameters chosen such that $P(\text{data}|H_1)$ is maximal. In other words, maximum likelihood (ML) estimates are used to determine the unknown parameters. The background-only hypothesis H_0 also has unknown parameters.

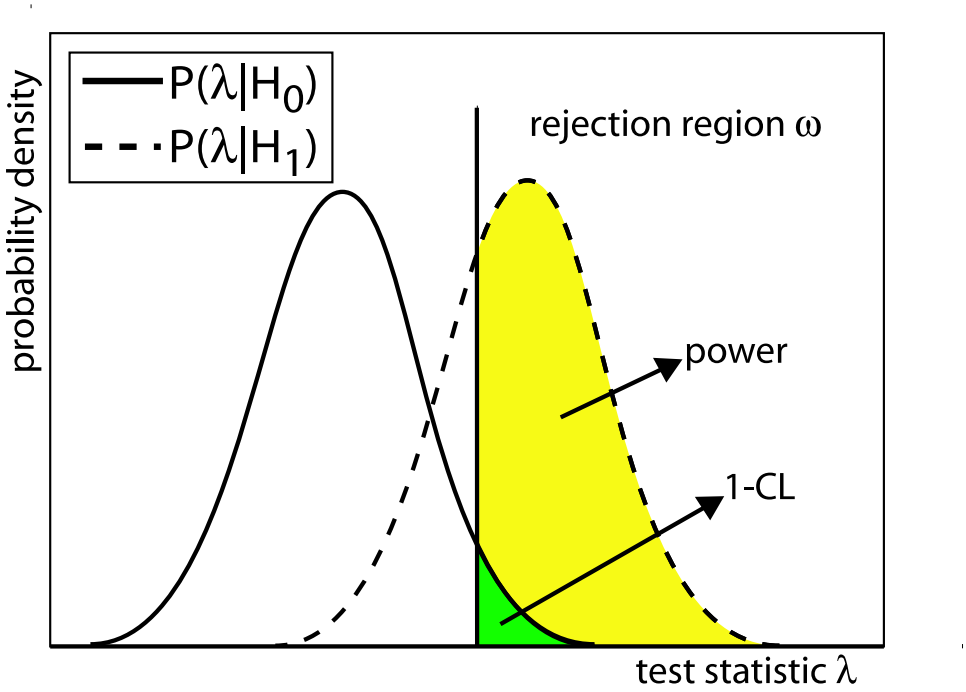

Figure 6.5: *Illustration of hypothesis testing. The probability density functions of the test statistic for H_0 and H_1 are shown. The rejection region ω is the region to right of the vertical line. The filled regions are related to the confidence level and the power of the test.*

For example, the normalisation of the atmospheric neutrino flux is uncertain. However, after a period of data taking, the ML estimators of the corresponding parameters can be estimated, and we can consider H_0 to be fully specified. In the remainder of this chapter, it is therefore assumed that H_0 does not contain unknown parameters.

In terms of the flux $\Phi(\theta, \phi, E, t)$, H_0 can be written as

$$H_0 : \quad \Phi(\theta, \phi, E, t) = \Phi^{\mathrm{bg}}(\theta, E), \tag{6.10}$$

where Φ^{bg} is the atmospheric neutrino flux, which is known to be independent of time and azimuth angle.

It is important that H_1 is precisely defined, since the power and interpretation of the search depend on what one is searching for. The most general hypothesis that we will consider for H_1 is: *In addition to the known background, there is a point source, with a power law spectrum with (unknown) spectral index, and (unknown) normalisation at an (unknown) position in the sky.* H_1 can be written as

$$H_1 : \quad \Phi(\theta, \phi, E, t) = \Phi^{\mathrm{bg}}(\theta, E) + \Phi^{\mathrm{sig}}(\theta, \phi, E, t), \tag{6.11}$$

where Φ^{sig} is the neutrino flux from the point source, which depends on the time due to the rotation of the Earth. It can be expressed as

$$\frac{d\Phi^{\mathrm{sig}}(\theta, \phi, E, t)}{dE d\Omega} = \varphi \cdot \left(\frac{E}{\mathrm{GeV}}\right)^{-\gamma} \delta\left[\cos\theta - \cos\theta_0(t, \alpha^{\mathrm{ra}}, \delta)\right] \; \delta\left[\phi - \phi_0(t, \alpha^{\mathrm{ra}}, \delta)\right], \tag{6.12}$$

where δ is the Dirac delta function and (ϕ_0,θ_0) is the time dependent location of the source in the sky, which depends on the (fixed) celestial coordinates $\alpha^{\rm ra}, \delta$. The spectral index of the energy spectrum of the source is denoted by γ and φ is the flux 'normalisation'[4].

In the case of a full sky search, ML estimators have to be determined for the parameters $\varphi, \gamma, \alpha^{\rm ra}, \delta$, whereas for a fixed point search, only φ and γ are free.

6.3.4 Expressions for the likelihood

The crucial ingredient for calculating the test statistic is the probability of the data for a given hypothesis, i.e. for a given neutrino flux.

After the reconstruction and selection procedures, the data will consist of a number of uncorrelated events. The ith event is characterised by the detection time t_i and the true values of the neutrino's zenith and azimuth angles and energy: θ_i, ϕ_i and E_i. The observed quantities are the reconstructed angles $\hat{\theta}_i$, $\hat{\phi}_i$, the reconstructed muon energy $\hat{E}_i$ and the time of the event t_i. The time of the event can be determined with an accuracy of about a millisecond, which makes the uncertainty on the event time negligible ($\hat{t} = t$) since the induced angular error is below 10^{-5} degrees.

The probability of obtaining a set of events $(\hat{\theta}_i, \hat{\phi}_i, \hat{E}_i, t_i)$ for flux Φ is (see appendix A)

$$\sum_i \log P(\hat{\theta}_i, \hat{\phi}_i, \hat{E}_i, t_i|\Phi) = \sum_i \log \Big[\mathcal{N}(\hat{\theta}_i, \hat{\phi}_i, \hat{E}_i, t_i|\Phi)\Big] - \langle N_{\rm tot}\rangle(\Phi) + C, \tag{6.13}$$

where $\mathcal{N}(\hat{\theta}_i, \hat{\phi}_i, \hat{E}_i, t_i|\Phi)$ denotes the expected density of events with the observed parameters $\hat{\theta}, \hat{\phi}, \hat{E}, t$ per unit[5] solid angle, energy and time due to the flux Φ. $\langle N_{\rm tot}\rangle(\Phi)$ is the expectation value of the total number of detected events produced by the flux Φ. The constant C does not depend on the flux and will be omitted in the remainder of this chapter, since it plays no role in the calculation of likelihood ratios or maximum likelihood estimates.

In general, $\langle N_{\rm tot}\rangle$ and $\mathcal{N}(\hat{\theta}_i, \hat{\phi}_i, \hat{E}_i, t_i|\Phi)$ can be calculated from the flux Φ and the knowledge of the detector behaviour. The total number of expected events is given by a convolution of the effective area for neutrinos, $A_\nu^{\rm eff}$, with the differential flux:

$$\langle N_{\rm tot}\rangle = \int A_\nu^{\rm eff}(\theta, \phi, E) \frac{d\Phi(\theta, \phi, E, t)}{dE d\Omega} d\Omega dE dt, \tag{6.14}$$

where the integration is over the live-time of the detector, over all upward directions and over all energies that produce events in the detector for the flux under consideration. Similarly, $\mathcal{N}(\hat{\theta}_i, \hat{\phi}_i, \hat{E}_i, t_i)$ is given by

$$\mathcal{N}(\hat{\theta}, \hat{\phi}, \hat{E}, t) = \int P(\hat{\theta}, \hat{\phi}, \hat{E}|\theta, \phi, E) A_\nu^{\rm eff}(\theta, \phi, E) \frac{d\Phi(\theta, \phi, E, t)}{dE d\Omega} d\Omega dE, \tag{6.15}$$

[4] We have explicitly made the term $\left(\frac{E}{\rm GeV}\right)^{-\gamma}$ dimensionless, so that φ always has the same units (e.g. GeV^{-1} m^{-2} s^{-1}), regardless of the value of γ.

[5] Note that the units used to express $\mathcal{N}$ do not play a role since the factors resulting from a change of units can be absorbed in the constant C.

where $P(\hat{\theta}, \hat{\phi}, \hat{E}|\theta, \phi, E)$ is the probability density (per unit solid angle and per unit energy) of obtaining reconstructed values $\hat{\theta}, \hat{\phi}$ and $\hat{E}$ when the true neutrino direction and energy are θ, ϕ and E.

In general, the integral in equation 6.15 is difficult to evaluate and numerical integration is very time consuming. However, for the fluxes that are of interest here, some approximations can be made to simplify the expression.

Likelihood for the background flux

Both the flux of atmospheric neutrinos and the neutrino effective area are known to be a smooth function of the zenith angle. In contrast, the function $P(\hat{\theta}, \hat{\phi}, \hat{E}|\theta, \phi, E)$ is sharply peaked around the true direction (θ, ϕ): the angle between the reconstructed muon direction and the true neutrino direction is typically smaller than a few degrees, which is small compared to the scales on which the flux or the effective area change significantly. This justifies the following approximation:

$$P(\hat{\theta}, \hat{\phi}, \hat{E}|\theta, \phi, E) \approx \delta(\phi - \hat{\phi})\delta(\cos\theta - \cos\hat{\theta})P(\hat{E}|E), \tag{6.16}$$

where $P(\hat{E}|E)$ is the probability density function for obtaining a reconstructed muon energy $(\hat{E})$ as a function of the true neutrino energy (E). Using this approximation, the density of expected events can be expressed as

$$\mathcal{N}^{\mathrm{bg}}(\hat{\theta}, \hat{\phi}, \hat{E}) = \int P(\hat{E}|E) A_{\nu}^{\mathrm{eff}}(\hat{\theta}, \hat{\phi}, E) \frac{d\Phi^{\mathrm{bg}}(\hat{\theta}, E)}{dE} dE. \tag{6.17}$$

The expected total number of background events, which contributes to $\langle N_{\mathrm{tot}} \rangle$ in equation 6.13, can be calculated from equation 6.17 by integrating over $\hat{E}$ and the angles, and by multiplying with the live-time. However, this quantity gives a constant contribution to the likelihood and it can therefore be neglected.

In practice, it will be possible to determine $\mathcal{N}^{\mathrm{bg}}$ directly from the data, since, in first order, all events can be considered to be background. In this way, the influence of systematic uncertainties in the atmospheric neutrino flux and the effective area may be reduced.

Likelihood for the signal flux

The differential flux from a point source with a power law energy spectrum with spectral index γ is given by equation 6.12. Substitution into equation 6.15 yields

$$\mathcal{N}^{\mathrm{sig}}(\hat{\theta}, \hat{\phi}, \hat{E}, t) = \varphi \int P(\hat{\theta}, \hat{\phi}, \hat{E}|\theta, \phi, E) A_{\nu}^{\mathrm{eff}}(\theta_0(t, \alpha^{\mathrm{ra}}, \delta), \phi_0(t, \alpha^{\mathrm{ra}}, \delta), E) \left(\frac{E}{\mathrm{GeV}}\right)^{-\gamma} dE \tag{6.18}$$

The three-dimensional PDF $P(\hat{\theta}, \hat{\phi}, \hat{E}|\theta, \phi, E)$ has been factorised. One factor is $P(\hat{E}|E)$, which was introduced in equation 6.16. The other is the probability density (per unit solid angle) for obtaining the reconstructed muon direction $(\hat{\theta}, \hat{\phi})$ for a true neutrino direction (θ, ϕ). This PDF is known as the point spread function (PSF), since it describes the distribution of the reconstructed coordinates if the events come from the

same point in the sky. The PSF is parameterised as a function of the angle α_ν between the directions of the neutrino and the reconstructed muon. The PDF of α_ν is determined for each event separately from the true neutrino energy (E) and the estimate of the error on the muon direction $\hat{\alpha}_\mu$ (see section 4.7.2). The expression for $P(\hat{\theta}, \hat{\phi}, \hat{E}|\theta, \phi, E, \hat{\alpha}_\mu)$ thus becomes

$$P(\hat{\theta}, \hat{\phi}, \hat{E}|\theta, \phi, E) = P(\alpha_\nu|\hat{\alpha}_\mu, E)P(\hat{E}|E). \tag{6.19}$$

The factors $P(\alpha_\nu|\hat{\alpha}_\mu, E)$ and $P(\hat{E}|E)$ have been estimated from simulations as will be discussed in section 6.3.5. The expected density of events from the signal flux is then

$$\mathcal{N}^{\text{sig}}(\hat{\theta}, \hat{\phi}, \hat{E}, t) = \varphi \int P(\alpha|\hat{\alpha}_\mu, E)P(\hat{E}|E)A_\nu^{\text{eff}}(\theta_0(t, \alpha^{\text{ra}}, \delta), \phi_0(t, \alpha^{\text{ra}}, \delta), E)\left(\frac{E}{\text{GeV}}\right)^{-\gamma} dE. \tag{6.20}$$

As expected, this expression contains four unknown parameters: the position of the source $(\alpha^{\text{ra}}, \delta)$, the spectral index γ and the flux normalisation φ.

The expectation value of the total number of signal events $\langle N_s \rangle$ gives the only relevant contribution to the term $\langle N_{\text{tot}} \rangle$ in equation 6.13, since the expected number of background events is constant (and can thus be absorbed in the constant C). It is calculated by

$$\langle N_s \rangle = \varphi \int A_\nu^{\text{eff}}(\theta_0(t, \alpha^{\text{ra}}, \delta), \phi_0(t, \alpha^{\text{ra}}, \delta), E)\left(\frac{E}{\text{GeV}}\right)^{-\gamma} dE dt. \tag{6.21}$$

For speed, the integration over time of $A_\nu^{\text{eff}}(\theta_0(t, \alpha^{\text{ra}}, \delta))$ is performed by using a table of the time-averaged effective area as s function of the celestial coordinates, which is multiplied by the live-time.

In conclusion, the calculation of each of the terms discussed in this section involves only the (one-dimensional) integration over the energy, instead of the three-dimensional integration in equations 6.14 and 6.15. As a result, the computation is now fast enough to be used in a practical search method.

6.3.5 Ingredients of the likelihood calculation

Knowledge of the detector response is used in the search method to evaluate equations 6.17, 6.20 and 6.21. The information used consists of three parts: the PSF, the effective area and a table describing the behaviour of the estimate of the muon energy as a function of the neutrino energy.

The PSF has been parameterised because it is used directly for fitting the position of the source. The maximisation algorithm is expected to work better with smooth functions than with tabulated values. In contrast, the information on the behaviour of the energy reconstruction and the effective area are not used directly in the fit, but are convolved with the neutrino spectrum. Therefore, no parameterisations are needed for these two quantities and tabulated values are used.

Point spread function

The point spread function is related to the PDF of α_ν, which was shown in figure 5.6 for the case of an E^{-2} spectrum. Here, this PDF is parameterised as a function of the

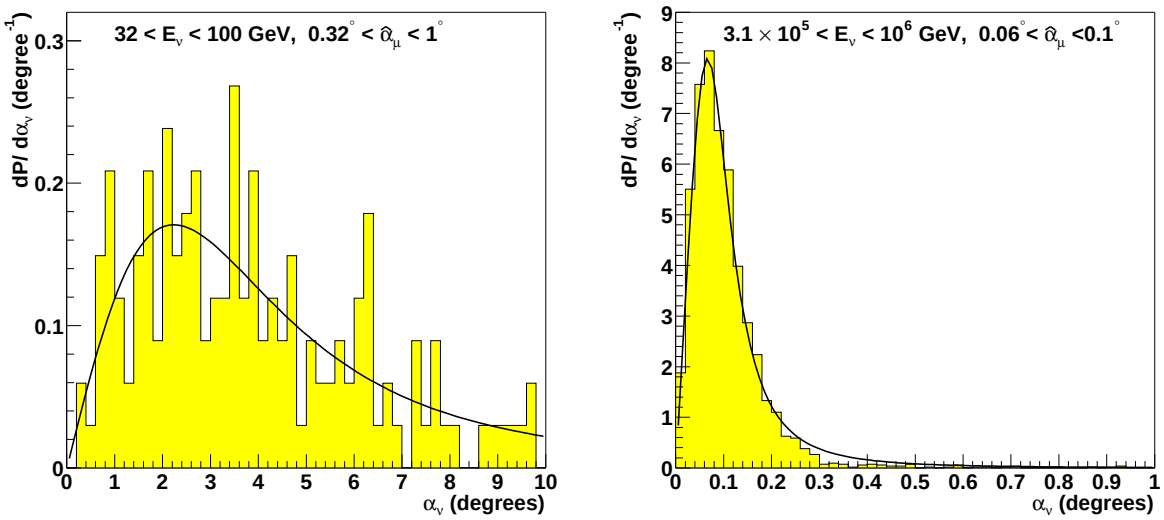

Figure 6.6: *Two examples of the distribution of the angle α_ν between the neutrino direction and the reconstructed muon direction for two arbitrarily chosen bins in the neutrino energy E and the error estimate $\hat{\alpha}_\mu$ obtained from simulations. The line is a fit to the data using the functional form of equation 6.22. This parameterisation is used in the search method.*

neutrino energy E and the estimated error on the muon direction, $\hat{\alpha}_\mu$. The PDF was parameterised for 12×8 bins[6] in $\log(E)$ and $\log(\hat{\alpha}_\mu)$ respectively, using the following functional form:

$$\frac{dP}{d\alpha_\nu} \propto \frac{\alpha_\nu}{1 + a\alpha_\nu^2 + b\alpha_\nu^4}. \tag{6.22}$$

Two examples of the distribution of the angle α_ν and the fitted parameterisations are shown in figure 6.6.

The point spread function used in the search method (i.e. the term $P(\alpha|\hat{\alpha}_\mu, E)$ in equation 6.20) is the probability density per unit solid angle. It is related to the PDF of α_ν:

$$P(\alpha|\hat{\alpha}_\mu, E) = \frac{dP}{d\Omega} = \frac{1}{2\pi \sin\alpha_\nu} \frac{dP}{d\alpha_\nu}. \tag{6.23}$$

The form of equation 6.22 was chosen such that equation 6.23 is well behaved for $\alpha_\nu = 0$, which ensures that no singularities occur in the likelihood function.

Neutrino effective area

A plot of the neutrino effective area was already shown in figure 5.5. In the search method, a table of the neutrino effective area as a function of the neutrino energy and the zenith angle is used. The azimuth dependence of the neutrino effective area has been neglected throughout this analysis in order to decrease statistical bin-by-bin fluctuations.

[6] In some bins, not enough events were simulated to fit the data. In that case, values of a and b (see equation 6.6) were copied from bins with the same $\hat{\alpha}_\mu$, but higher E.

PDF of the reconstructed muon energy

The probability density function of finding a muon with reconstructed energy $\hat{E}$ was determined from simulations as a function of the neutrino energy E_ν. It is shown in figure 6.7.

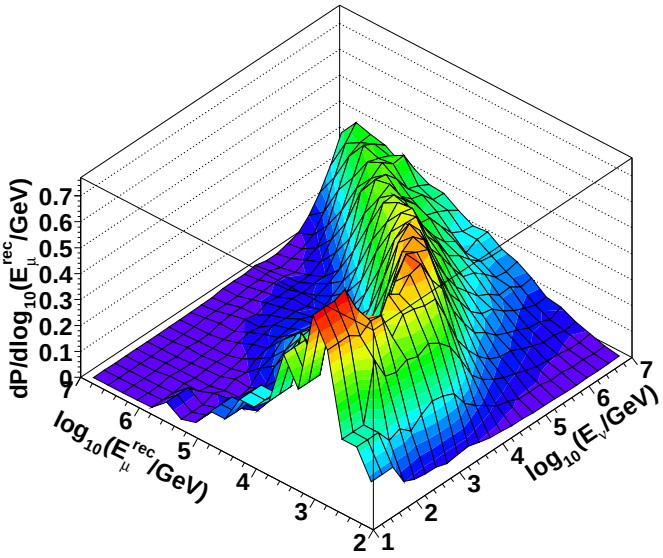

Figure 6.7: *Probability density function of the reconstructed muon energy as a function of the true neutrino energy.*

6.3.6 Likelihood maximisation

To evaluate the test statistic, maximum likelihood estimates of the unknown parameters of the signal hypothesis are needed. This means that values for $\alpha^{\mathrm{ra}}, \delta, \gamma$ and φ must be found that maximise

$$\log P(\mathrm{data}|\alpha^{\mathrm{ra}}, \delta, \gamma, \varphi) = \sum_i \log\left[\mathcal{N}^{\mathrm{sig}}(\hat{\theta}_i, \hat{\phi}_i, \hat{E}_i, t_i|\alpha^{\mathrm{ra}}, \delta, \gamma, \varphi) + \mathcal{N}^{\mathrm{bg}}(\hat{\theta}_i, \hat{\phi}_i, \hat{E}_i|\Phi^{\mathrm{bg}})\right] - \langle N_s\rangle(\alpha^{\mathrm{ra}}, \delta, \gamma, \varphi), \tag{6.24}$$

where $\langle N_s\rangle(\alpha^{\mathrm{ra}}, \delta, \gamma, \varphi)$ is the expectation value of the number of events due to the signal flux and $\mathcal{N}^{\mathrm{sig}}(\hat{\theta}_i, \hat{\phi}_i, \hat{E}_i, t_i|\alpha^{\mathrm{ra}}, \delta, \gamma, \varphi)$ is given by equation 6.20.

For any given source position $(\alpha^{\mathrm{ra}}, \delta)$, the factor $P(\alpha|\hat{\alpha}_\mu, E)$ in equation 6.20 will only be non-negligible for events with reconstructed celestial coordinates that are close to the source position. It is therefore sufficient to evaluate only one cluster of events at a time.

The clusters are selected by a clustering algorithm. A cluster can be built around each event by selecting all other events that are located within a cone with an opening angle of 1.25°. This opening angle is called the cluster size. It was chosen to be large compared to the typical angular resolution in order to ensure that all relevant events are selected. However, it can not be chosen too large, since the number of clusters increases very rapidly with the cluster size. The value of 1.25° was found to give an acceptable

performance, while the sensitivity is not degraded compared to larger cluster sizes. Note also that 1.25° is large compared to the optimal bin size found in section 6.2. To increase the speed of the algorithm, clusters with less then four events are not taken into account. It was checked that such clusters have a negligible probability to produce a 3σ effect.

For each cluster the likelihood maximisation is performed by the `e04jyf` function from the NAG library [69]. The fit is started with $\gamma = 2$, $\varphi = 3 \times 10^{-3}$ m^{-2}s^{-1} and with the coordinates $(\alpha^{\mathrm{ra}}, \delta)$ at the centre of gravity of the coordinates of the events. The fit results in estimates of the position and the flux of the point source. The likelihood ratio corresponding to the fitted values can now be calculated as follows:

$$\begin{aligned} \lambda &= \sum_i \log\left[\mathcal{N}^{\mathrm{sig}}(\hat{\theta}_i, \hat{\phi}_i, \hat{E}_i, t_i|\Phi^{\mathrm{sig}}) + \mathcal{N}^{\mathrm{bg}}(\hat{\theta}_i, \hat{\phi}_i, \hat{E}_i|\Phi^{\mathrm{bg}})\right] \\ &\quad - \log\left[\mathcal{N}^{\mathrm{bg}}(\hat{\theta}_i, \hat{\phi}_i, \hat{E}_i|\Phi^{\mathrm{bg}})\right] - \langle N_{\mathrm{tot}}\rangle(\Phi^{\mathrm{sig}}), \end{aligned} \tag{6.25}$$

where $\mathcal{N}^{\mathrm{sig}}$ is calculated using equation 6.15 with the fitted values for $\varphi, \gamma, \alpha^{\mathrm{ra}}$ and δ. The sum in equation 6.25 is restricted to the events in the cluster.

The cluster with the highest value of the likelihood ratio is considered the 'best' source candidate. This is not necessarily the cluster with the highest likelihood and therefore we do not, strictly speaking, use ML estimates for the source position.

In case of a fixed point search, a similar procedure is followed. In this case, the clusters are selected by selecting all events within an angle of 5° from the coordinates of the candidate source. The parameters φ and γ are then fitted to the events in each cluster, while the source coordinates are fixed. Again, the cluster with the highest value of the likelihood ratio corresponds to the best source candidate.

6.4 Full sky search

In this section, the results of the method described in section 6.3 are presented for a search for a point source with a power law spectrum with unknown spectral index and flux at an unknown position. This means that the four parameters of the point source flux (the source position, the spectral index and the normalisation of the flux) were left free when maximising the likelihood for the signal+background hypothesis.

6.4.1 Distribution of the test statistic

The distribution of the test statistic for the background-only case has been obtained from a simulation of about 50000 one-year periods of data taking, containing, on average, 3650 selected atmospheric neutrino events each. These samples were generated by (over)sampling a set of $\sim 66 \times 10^3$ simulated events while randomly choosing the time of detection and azimuth angle, both of which enter into the calculation of the celestial coordinates. In each one-year sample, the likelihood ratio is determined for an average of 74 clusters of events. The highest value of the likelihood ratio is the test statistic λ obtained for the one-year experiment.

The distribution of λ for background-only experiments is shown in figure 6.8. A discovery is made if the test statistic exceeds a critical value λ_c. The value of λ_c follows

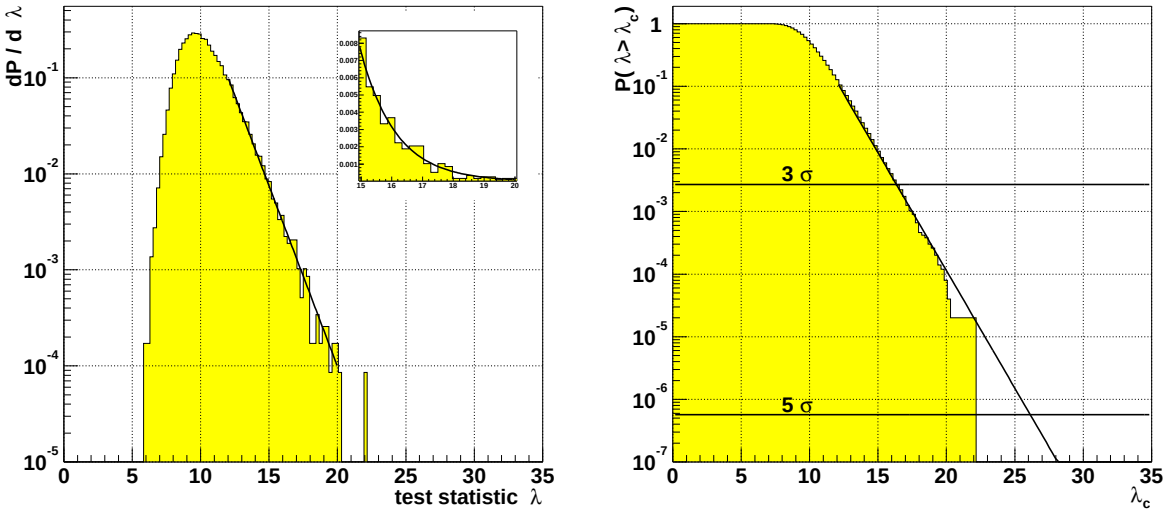

Figure 6.8: *Left: Distribution of the test statistic in case only background is present. An exponential function is fitted to the tail of the distribution to extrapolate to the* 5σ *level. Right: Cumulative distribution of the test statistic* $\int_{\lambda_c}^{\infty} \frac{dP}{d\lambda} d\lambda$. *Indicated are the probabilities corresponding to the* 3σ *and* 5σ *CL.*

from the distribution of λ in the case there is only background and from the desired confidence level (CL), since, by definition, $1 - \mathrm{CL} \equiv \mathrm{P}(\lambda_0 > \lambda_c | \mathrm{H}_0)$. Values for λ_c have been determined from figure 6.8(right) for the confidence levels (CLs) of $1 - 2.7 \times 10^{-3}$ and $1 - 5.7 \times 10^{-7}$, which are also known as the 3σ and 5σ CLs. Due to the limited number of simulated experiments, it was not possible to determine the value of λ_c that corresponds to the 5σ CL by means of simulations. In order to estimate this value, an exponential function was fitted to the distribution in figure 6.8, which is used to extrapolate to the probability corresponding to the 5σ CL. This yields the following values for λ_c for 3σ and 5σ CLs: $\lambda_c^{3\sigma} = 16.3$ and $\lambda_c^{5\sigma} = 26.1$.

The distribution of the test statistic for a source at a declination of $\delta = -81^\circ$ is shown in figure 6.9 for $N_s = 3, 6, 9$ and 12 detected signal events. As expected, the value of λ is increased by the presence of the signal. Whereas N_s represents the *actual* number of signal events that are detected (i.e. pass the selection criteria), only the *expectation value* of N_s, $\langle N_s \rangle$, can be calculated from a given neutrino flux. N_s is distributed according to a Poisson distribution with mean $\langle N_s \rangle$. The distribution of the test statistic for any value of $\langle N_s \rangle$ can therefore be calculated by

$$P(\lambda | \langle N_s \rangle) = \sum_{N_s=0}^{\infty} P(\lambda | N_s) \frac{\langle N_s \rangle^{N_s} e^{-\langle N_s \rangle}}{N_s!}. \tag{6.26}$$

In practice the summation is truncated when the terms become negligible[7].

[7] The maximal value of N_s in the simulations is 14.

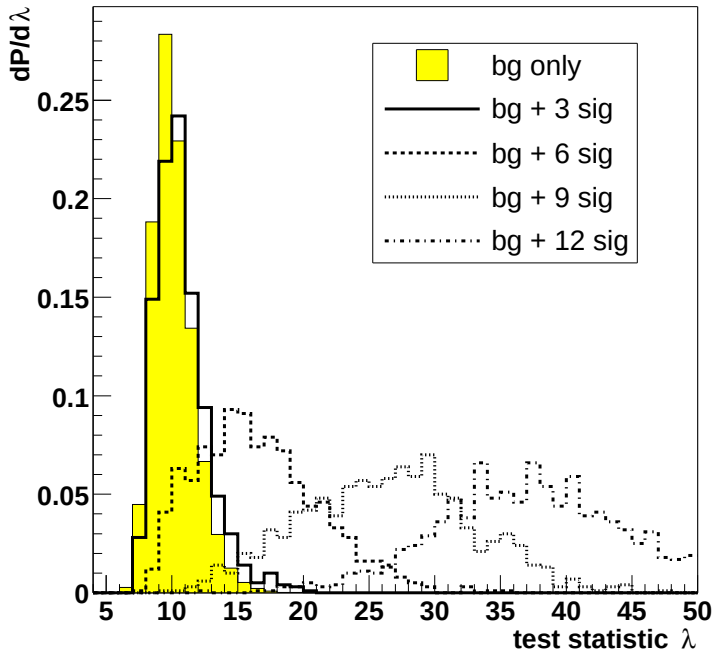

Figure 6.9: *Distribution of the test statistic for the background only case and for the case where a number of signal events are present. The point source signal has an E^{-2} energy spectrum and is located at a declination of $-81°$.*

6.4.2 Examples

As an illustration of the LR method, three rare examples of clusters of events and the corresponding value of the test statistic are shown in figure 6.10. The cluster in figure 6.10.a consists of only four events, but since three of them are located very close to the fitted (and true) source position, the likelihood ratio has a value of 19.20, which means that the source would be discovered at 3σ CL. In contrast, when using the binned method discussed in section 6.2 at least 6 events are needed to discover a source at 3σ CL at this declination (see figure 6.3).

The cluster in figure 6.10.b is an example of a cluster that has a low value of the test statistic, 11.48, despite the relatively large number of events (i.e. 6). Typically, clusters with 6 signal events, have $\lambda \approx 15$, but this cluster is more background-like due to the large angular deviations and the low values of the reconstructed energy of the events.

Finally, the cluster in figure 6.10.c is an example of a background-only cluster that has a high value of the test statistic: $\lambda = 17.56$. The probability that such a cluster (or one with a even higher value of λ) appears in a one year background-only sample is about 10^{-3}. Apart from the small angular separation between the events and the relatively high energies, the likelihood ratio of this cluster is large because it occurs at a declination of 15°, where the number of background events is relatively low. As a consequence the likelihood for the background hypothesis is low for this cluster, which enhances the value of the test statistic.

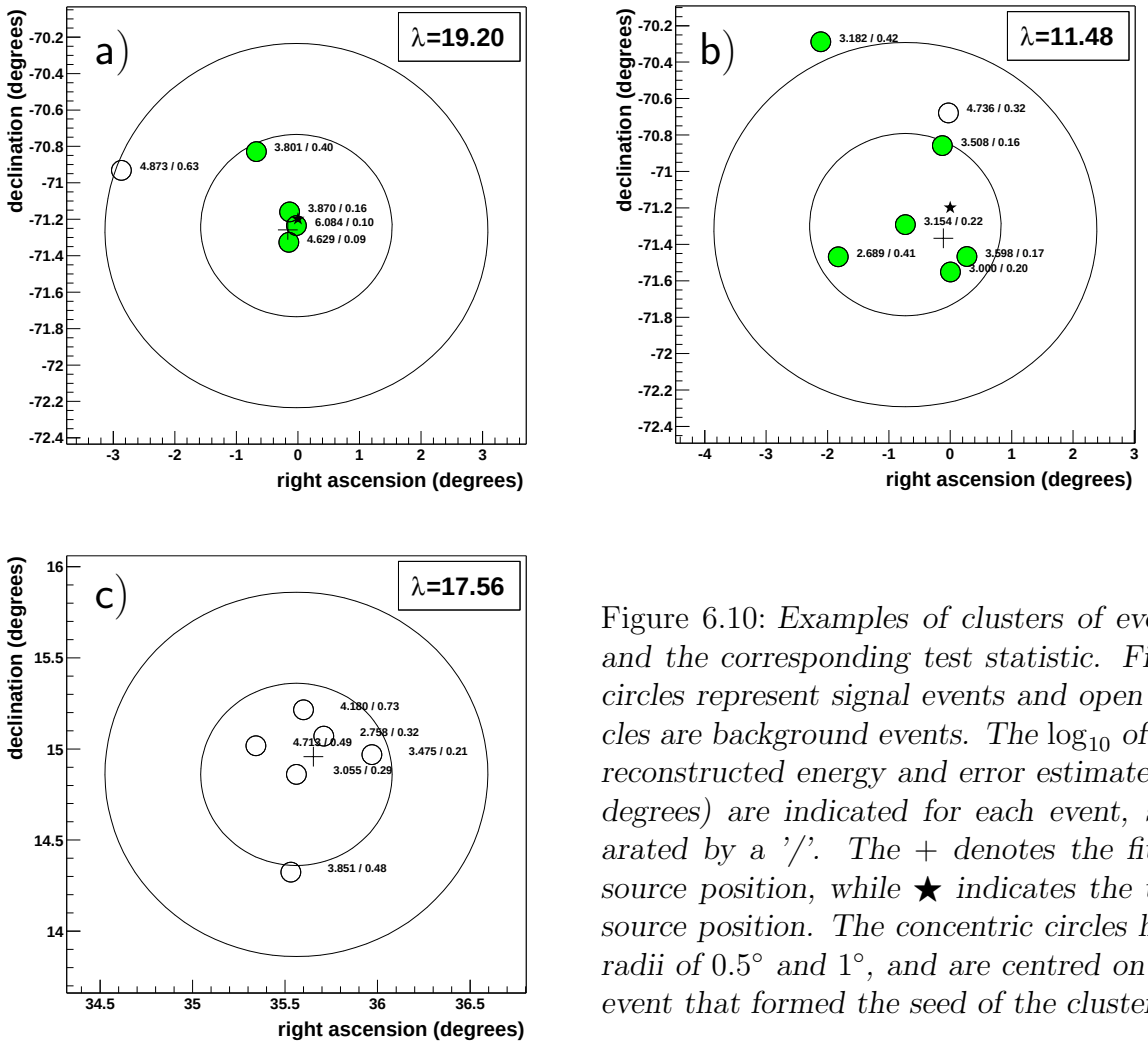

Figure 6.10: *Examples of clusters of events and the corresponding test statistic. Filled circles represent signal events and open circles are background events. The* $\log_{10}$ *of the reconstructed energy and error estimate (in degrees) are indicated for each event, separated by a '/'. The + denotes the fitted source position, while ★ indicates the true source position. The concentric circles have radii of* 0.5° *and* 1°*, and are centred on the event that formed the seed of the cluster.*

6.4.3 Fitted source position

For each cluster, the source coordinates are fitted to the data. As a result, we obtain an ML estimate of the source location. In figure 6.11 this fitted source position is compared to the true position of the source.

The resolution is defined as the median of the angular error on the source position, similar to the resolution of a single event (see section 5.2.3). As expected, the resolution on the source position improves as the number of detected events from the source, N_s, increases. The resolution could be expected to be approximated by $\alpha_\nu^{\gamma=-2}/\sqrt{N_s}$, where $\alpha_\nu^{\gamma=-2}$ is the median of the single-event resolution for an E^{-2} neutrino source, which is 0.23°. The ML estimate of the source position is somewhat more accurate than this, as is shown in figure 6.11. In order to discover a source at $3\sigma(5\sigma)$ CL, about 6(9) events need to be detected. The position of the source can then be determined with an accuracy of about 0.08°(0.07°).

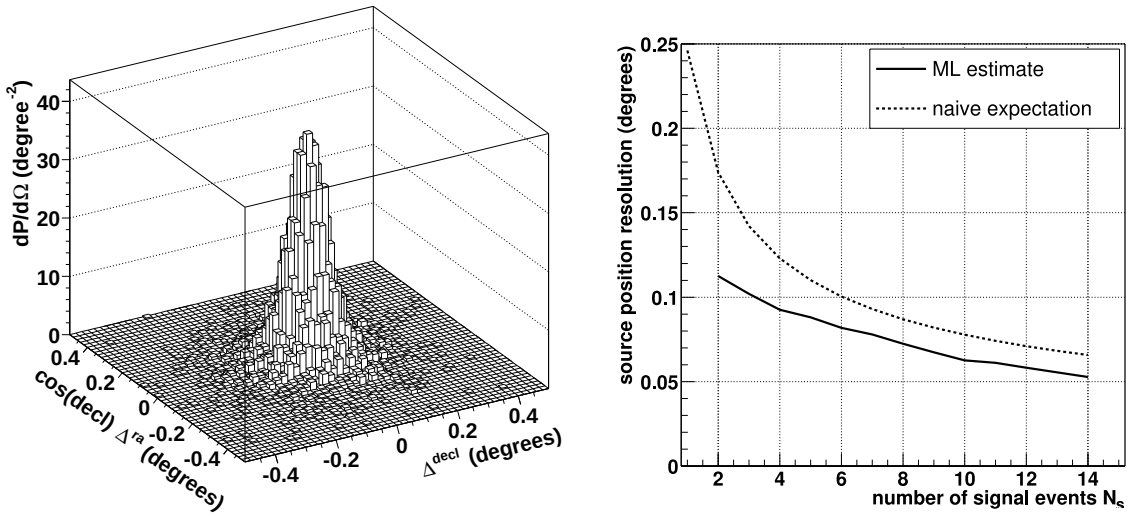

Figure 6.11: *Left: Distribution of the error of the fit of the right ascension and the declination of the neutrino point source for a source producing 6 events in the detector. Right: Resolution of the determination of the position of the source as a function of N_s, i.e. the number of events produced by the source. The dashed line indicates the 'naive expectation' that results from scaling the single event resolution with $1/\sqrt{N_s}$.*

6.4.4 Discovery potential

The probability of discovering a source (i.e. the power of the test) at the $3(5)\sigma$ level is given by the probability of $P(\lambda|\langle N_s\rangle)$ to exceed the value of $\lambda_c^{3\sigma}$ ($\lambda_c^{5\sigma}$), which was found in section 6.4.1. This probability is calculated using equation 6.26 and the result is shown in figure 6.12 as a function of $\langle N_s\rangle$ for a source at a declination of $-81°$.

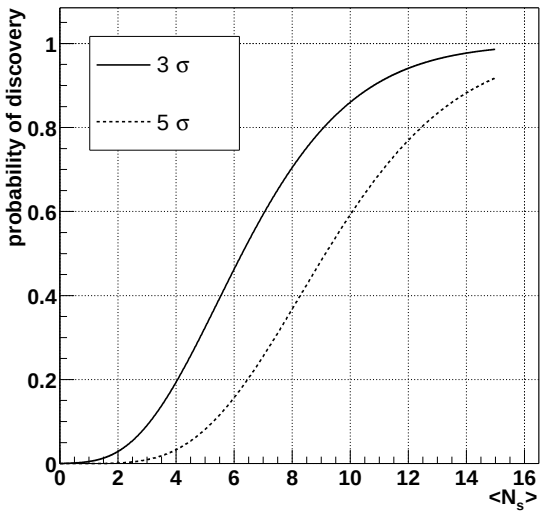

Figure 6.12: *The probability for the discovery of a point source as a function of the expectation value of the number of observed signal events from the source (which is directly related to the flux of the source) at the 3σ and 5σ level after one year of data taking.*

As a measure of the discovery potential, we take the number of events (or neutrino flux) needed for a 50% probability to discover the source. This quantity is shown in figure 6.13 and is compared to the discovery potential obtained with the binned method described in section 6.2. Compared to the binned method, the LR method needs rougly 40(35)% less events in order to make a $3(5)\sigma$ discovery after one year of data taking. Consequently, the LR method can discover a source at the 5σ level, while it is only a 3σ effect when using the binned method. Using equation 6.21, the average number of events needed for discovery can be directly translated into the normalisation of the required neutrino flux, which is shown in figure 6.14. In order to make a 5σ discovery, a neutrino flux is needed of roughly $1.4 \times 10^{-3}\ E^{-2}$ GeV m^{-2} s^{-1} for the lowest declinations.

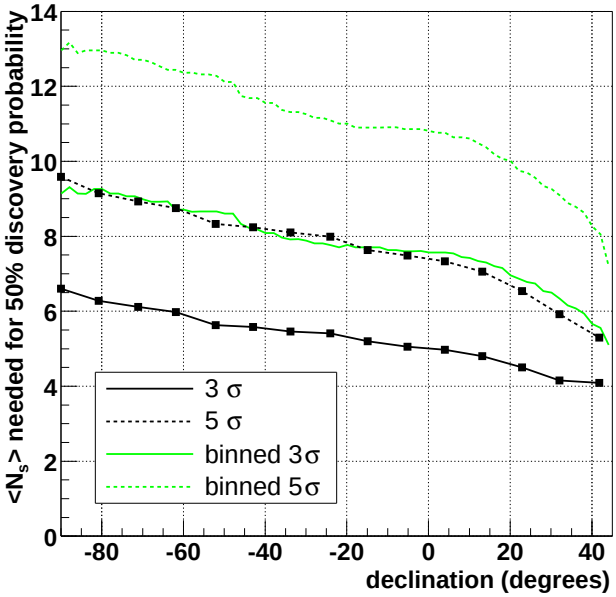

Figure 6.13: *Discovery potential of the search after one year of data taking, in terms of the expectation value of the number of signal events required to yield a probability of 50% for discovery of the source in a full sky search as a function of the declination of the source. Also shown is the result obtained with the binned method.*

Discovery potential after two years of data taking

The discovery potential was also determined for a two-year data taking period. The results are shown in figure 6.15. Since there are more background events in the two-year sample, between roughly 5% and 20% more events are needed, depending on the declination. As a result, the flux that can be discovered is a factor 1.7 to 1.9 lower than the flux that can be discovered after one year.

6.4.5 Exclusion limit

If a small value of the test statistic is observed, no discovery can be claimed, but the existence of an intense source of neutrinos can be excluded. This results in a declination dependent upper limit on the flux.

If, after a period of data taking, a value λ_0 is obtained, then, all signal hypotheses that would yield a value greater than λ_0 in at least 90(99)% of the cases can be excluded

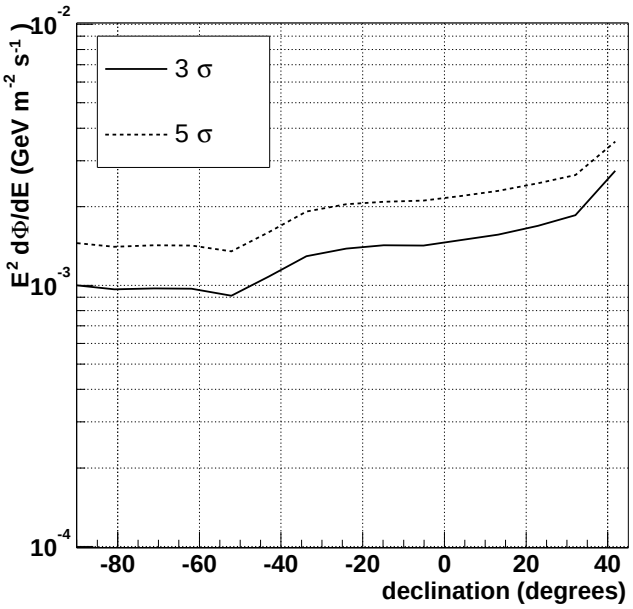

Figure 6.14: *Neutrino flux from a point source needed to yield a probability of 50% of discovery of the source in a one-year full sky search as a function of the declination.*

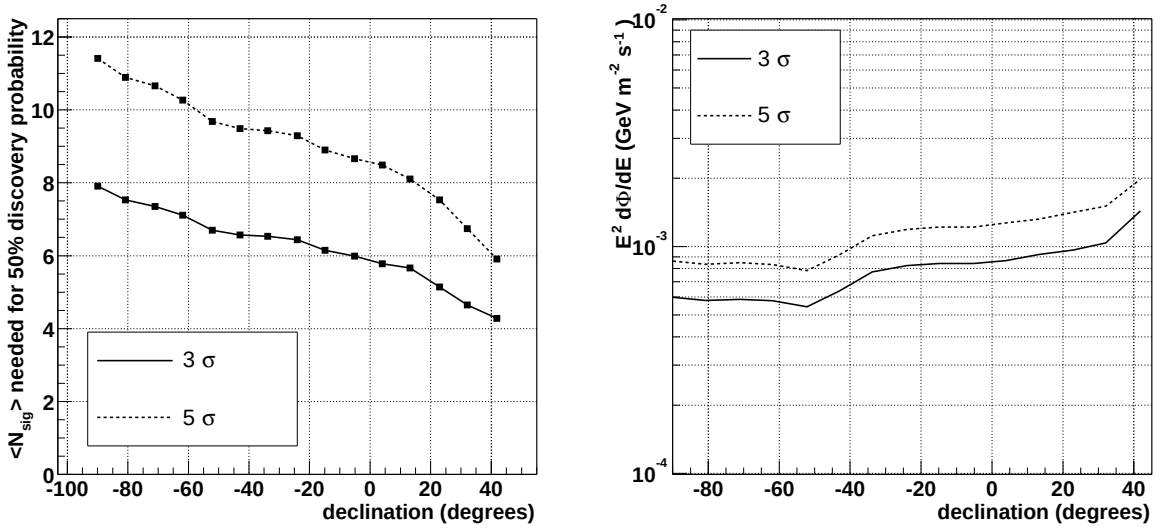

Figure 6.15: *Left: Number of events needed for a 3(5)σ discovery of a point source, after two years of data taking. Right: Flux needed for discovery of a point source after two years of data taking.*

at 90(99)% CL. As a characteristic value for λ_0, we take the median of the distribution of the test statistic in case there is only background. Using a similar calculation as for the discovery potential, the corresponding flux limit is found in terms of the expectation value of the number of signal events $\langle N_s \rangle$. The result is shown in figure 6.16. Since λ_0 is the median of the distribution, the result should be interpreted as follows: *If there is no point source of neutrinos, there is a 50% probability that we will be able to set the limit*

shown in figure 6.16 or a stronger one.

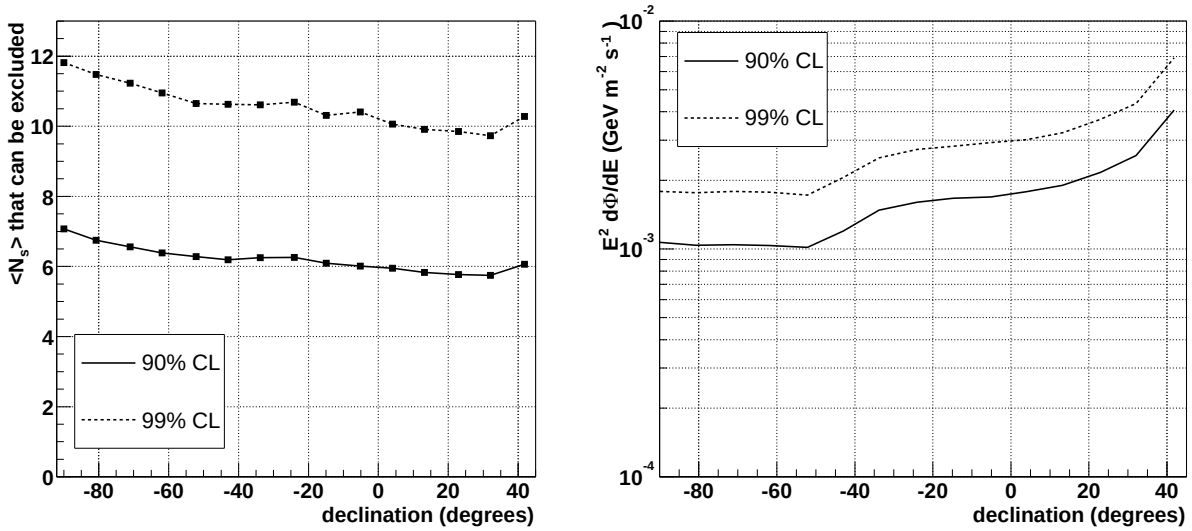

Figure 6.16: *Left: Median exclusion limit for an E^{-2} source anywhere in the sky in terms of the number of events produced by that source. The probability of being able to set this limit or a stronger one is 50% in the case that there is no signal. Right: Median exclusion limit on the (E^{-2}) flux from a source anywhere in the sky.*

6.5 Fixed point searches

In this section, the LR method will be used to 'search' for a source at a number of predefined locations in the sky. This restriction increases the sensitivity for a source at the specified location by reducing the 'trial factor' that stems from searching at many different locations in the sky. While it is unlikely that, in reality, the search will be restricted to only one single point, the upper limit on the flux that is obtained from such a search is an important quantity, as will be explained in section 6.5.3.

6.5.1 Distribution of the test statistic

For a single-point search, the distribution of the test statistic λ for the background-only case is shown in figure 6.17. In many cases, the fitted flux is zero, resulting in $\lambda = 0$. In these cases, the fluctuations in the background are less signal-like than the average background cluster. The tail of the distribution is approximately proportional to $e^{-s\lambda}$, with $s \approx 1$. The fitted values of s vary between 0.92 and 0.99, depending on the declination. The exponential distribution may be intuitively understood: for the background-only case, the probability to obtain a given likelihood ratio is inversely proportional to the likelihood ratio. Under the assumption that the ML estimates of the free parameters in H_1 are normally distributed around the true values, it can be shown [80] that λ is distributed

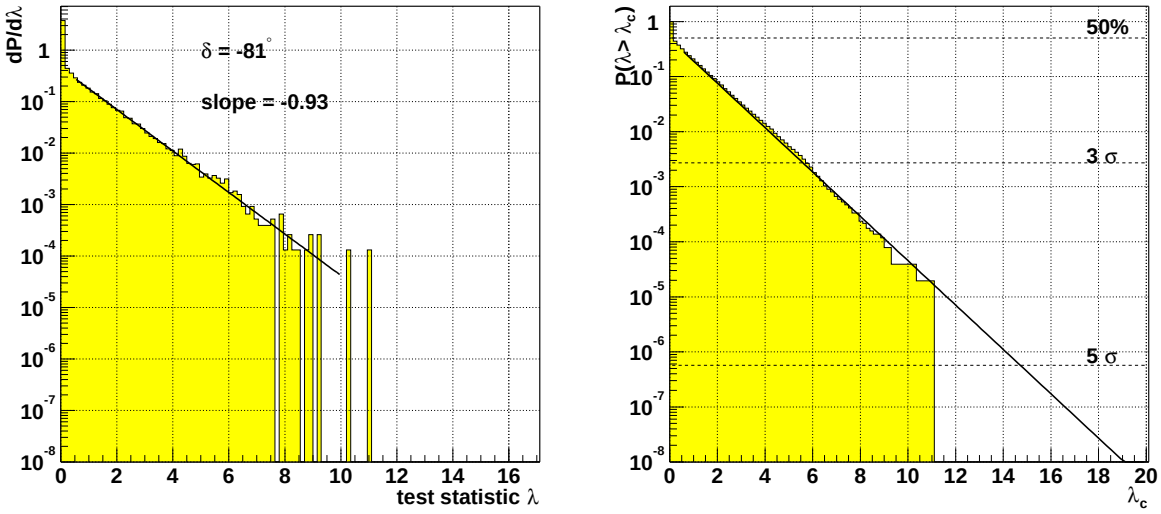

Figure 6.17: *Left: Distribution of the test statistic for a fixed point search for simulated background-only experiments. The line is an exponential function that was fitted to the data. Right: Cumulative distribution, indicating the probability to obtain a value of the test statistic that is higher than the ordinate. Indicated are the probabilities corresponding to the 3σ and 5σ confidence levels and the line corresponding with a probability of 50%. The line corresponds to the fit in the left figure.*

according to a $\chi^2(r)$ distribution, where r is the number of unknown parameters in H_1. This assumption in not strictly valid here, since the true value ($\varphi = 0$) is at the boundary of the allowed region ($\varphi > 0$), which results in the peak at $\lambda = 0$. However, when considering only the cases with positive φ, the distribution is reasonably well approximated by a $\chi^2(2)$ distribution, i.e. $dP/d\lambda \propto \chi^2(2) = e^{-\lambda}$.

If multiple candidate sources are being considered, the test statistic is taken to be the likelihood ratio of the most signal-like candidate (i.e. the one with the highest likelihood ratio). The distribution of the test statistic is shown in figure 6.18 for the cases where 10 and 100 candidate sources are being considered. The sources were assumed to have random positions, uniformly distributed in $\sin(\delta)$. The PDF of λ scales linearly with the number of candidates for large values of λ. This is expected as long as the candidate sources are separated by angular distances much larger than the resolution of the detector.

The distribution of the test statistic when a signal is present is shown in figure 6.19 for several values of the number of selected signal events. Again, the presence of one or more signal events results in an increase in the test statistic.

6.5.2 Discovery potential

The probability of discovering the source at the $3(5)\sigma$ CL has been calculated from the distributions of λ in the same manner as described in section 6.4.4. The number of signal events needed for a 50% discovery probability is shown in figure 6.21 for the cases where

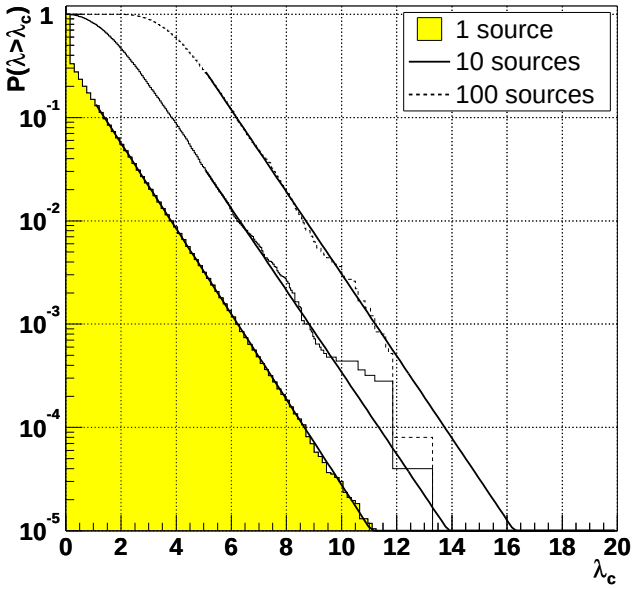

Figure 6.18: *Distribution of the test statistic in a fixed point search for background-only when 1,10 and 100 candidate neutrino sources are being considered. The candidate sources are uniformly distributed in the sky. The lines are exponential fits to the distributions.*

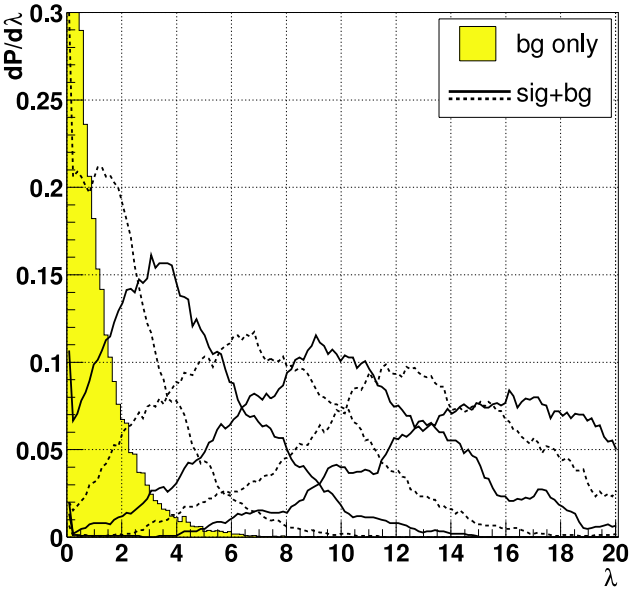

Figure 6.19: *Distributions of the test statistic in a fixed point search for background-only and one candidate source (filled histogram), and for the case where a number of signal events (1 to 6, from left to right) are present in addition to the background. The declination of the source is* $-81°$.

1,10 and 100 source candidates are considered.

The number of signal events required for a discovery with the binned method is also shown in figure 6.17. The LR method requires typically about 15% less events to discover a source. While this is a modest improvement, it means, for example, that 100 candidate sources can be considered instead of 10 while retaining the same sensitivity for a 5σ discovery.

The neutrino flux needed for a discovery is shown in figure 6.17(right). It can be compared to the flux needed for a discovery in a full sky search (figure 6.14). If the search is restricted to 10 sources, for example, the flux needed for a discovery is roughly half the

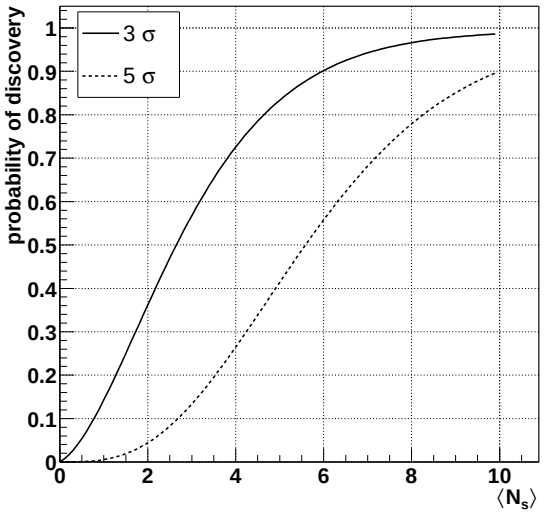

Figure 6.20: *Probability to discover the source in a one-year fixed point search with one candate source as a function of the expectation value of the number of detected events for a declination of* $-81°$.

flux that would be required in a full sky search.

6.5.3 Upper limits

It is unlikely that a point source search will be restricted to only a single point in the sky. However, the value of the test statistic obtained for a particular point in the sky can also be used to set an upper limit on the flux from that particular direction. The value of the limit depends on the observed value of the test statistic λ_0, which is distributed as shown in figure 6.17 under the assumption that no neutrino source is present. The mean value of λ varies between $0.5(\delta = -90°)$ and 0.2 $(\delta = 40°)$. The resulting mean number of events from a point source that can be excluded is shown in figure 6.22 for 90% and 99% CL.

A flux limit can be determined in this way for each point in the sky individually. However, the presence of a point source at *any* location is not ruled out by these limits, in contrast to the limits discussed in section 6.4.5.

6.6 Discussion

The LR method that has been presented in this chapter is a valuable tool for detecting point sources with ANTARES. Compared to the more conventional binned method, the discovery potential is increased by up to 40%. This means that sources can be discovered at the 5σ CL that can only be detected at about the 3σ CL with the binned methods. Below some more aspects of the method are discussed.

- A disadvantage of the LR method is its complexity. Both the principle and the implementation of the method are more complicated than for binned methods. Furthermore, the LR method relies on knowledge of the detector response, which is implemented via parameterisations and tables of the point spread function, the neutrino effective area and the response of the energy estimator. Inaccuracies in any of these will result in a degraded sensitivity of the search method. However,

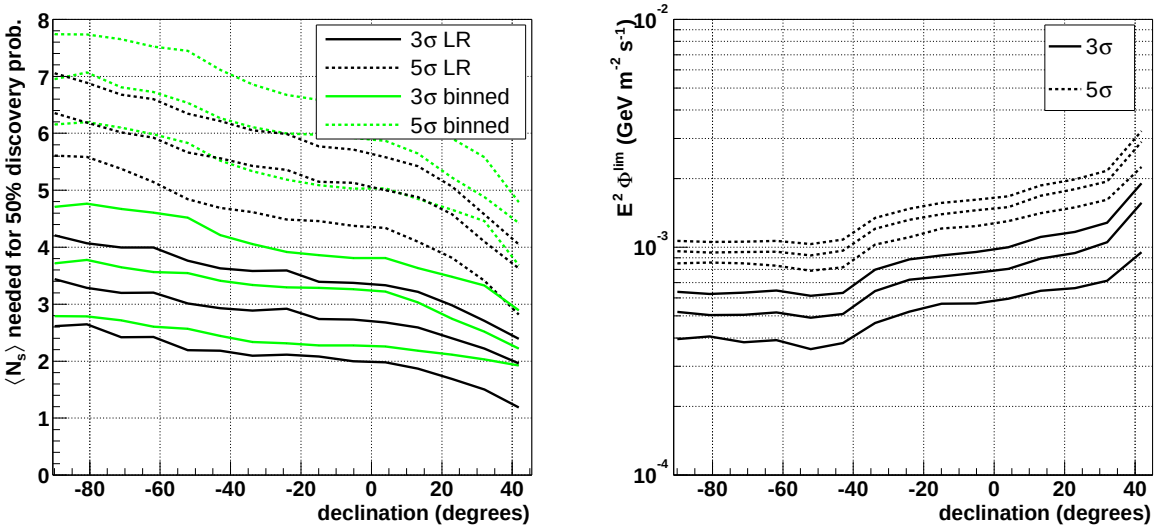

Figure 6.21: *Left: Expectation value of the number of detected events from an E^{-2} neutrino point source needed to yield a 50% probability of discovering the neutrino point source as a function of declination. The three curves correspond to a search in which 1,10 and 100 (from bottom to top) candidate sources are considered. Also shown are the results from the binned method. Right: Neutrino flux needed to give a 50% discovery probability as a function of the source declination for a search with 1,10 and 100 (from bottom to top) source candidates.*

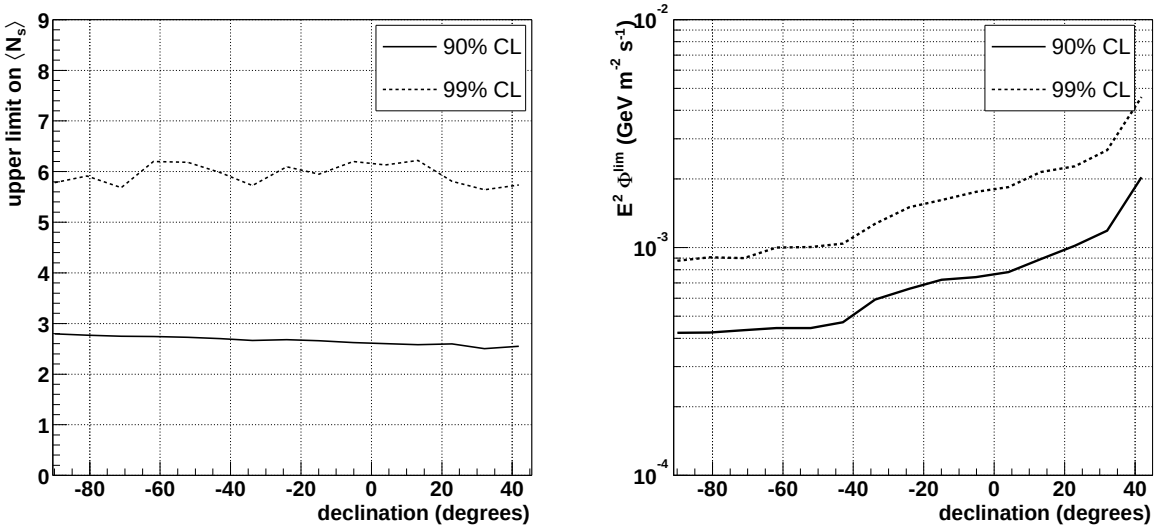

Figure 6.22: *Left: Mean upper limit that can be set on the mean number of signal events $\langle N_s \rangle$ from an E^{-2} neutrino point source as a function of declination. Right: Mean upper limit that can be set on the neutrino flux from an E^{-2} point source as a function of declination.*

the probabilistic statements made will remain valid; i.e. the method does not require perfect knowledge of the detector response in order to accurately determine the significance of a cluster of events. Moreover, binned methods require knowledge of the detector response as well. Knowledge of the angular resolution, for example, is used to optimise the bin size. The influence of systematic uncertainties in the angular resolution, acceptance (effective area) and energy estimation on the sensitivity should be studied in the future for both methods.

- The LR method was developed to be an optimal way to search for point sources: at any confidence level, the discovery potential (power) should be optimal. The derivation in the first part of this chapter explicitly states the approximations made that could lead, in principle, to degradation of the method compared to the full maximum likelihood ratio test.

- The LR method does not require any optimisation. No special cuts are required on the input sample and there are no bin sizes to be optimised. The disadvantage of such optimisations is that one needs to make a choice what to optimise for. A binned method optimised for maximum discovery potential at e.g. 3σ CL will, in general, not be optimal at other confidence levels nor for setting an upper limit. Note that, in the comparison with the binned methods, the bin size was always chosen to be optimal for the stated CL.

- By simply fixing or releasing parameters in the fitting routine that finds the most likely signal hypothesis, one can change the scope of the search-method. For example the search could be restricted to look only for sources with a particular spectrum or to look only for sources at specific points in the sky. Each of these searches will have its own interpretation and discovery potential.

6.6.1 Comparison with models and experiments

Searches for point sources of neutrinos have been conducted by various experiments. No sources have been discovered, and upper limits on the flux have been published by the MACRO [81] and AMANDA-II [82] experiments[8]. These are 'point-by-point' limits of the type discussed in section 6.5.3. The established limits are shown in figure 6.23 and can be compared to the limit that ANTARES expects to set in one year. The MACRO results are for a live-time of 6.3 years. The AMANDA-II limit is obtained from 197 days of data taken in the year 2000. It will be further improved as more data is analysed. Also indicated is the limit that is expected to be set after one year of taking data with the IceCube detector, which is being built on the South Pole [84, 85] and is planned to be completed by 2011. In the northern hemisphere, ANTARES will improve on the present limits after one year of data taking. The flux needed for a 5σ discovery is also shown in the figure. The limits set by MACRO do not exclude the possibility that ANTARES will discover a source at 5σ CL. For the part of the sky which is visible to both ANTARES and AMANDA, the latter experiment already excludes this possibility, although one should

[8] A search was also performed by the Super-Kamiokande [83] collaboration, but only limits on the neutrino induced muon flux have been published.

bear in mind that the AMANDA limit in the figure represents the average limit and that there are source candidates for which the limit is higher.

It should be stressed that any inefficiencies due to dead time of the detector or high levels of optical background have been neglected in the calculation for ANTARES. Depending on the circumstances, the sensitivity presented here may only be reached after several years of operating the detector, especially since the optical background rate is often much higher than 60 kHz, which is the value used in the simulations (see section 2.6).

A number of flux models were already shown in figure 1.3. Most of the fluxes in this figure are too low to be detected by ANTARES, even after several years of data taking. This confirms the general notion that neutrino telescopes require an effective area of the order of a km^2. Nevertheless, the AGN core model [14] predicts fluxes in the sensitivity range of ANTARES. Hence, the most luminous AGNs could be detected if a significant fraction of the non-thermal energy emitted by these objects is due to hadronic interactions.

In addition, figure 6.23 shows neutrino flux predictions for a number of Galactic microquasars taken from [26]. The intense fluxes predicted imply that microquasars may be the first objects that will be detectable by neutrino telescopes. Many microquasars show strong temporal variability. The fluxes are given for the active state and may only be applicable for a fraction of the time. Furthermore, oscillations are not taking into account, so the expected flux of ν_μ's is actually a factor two lower. If these predictions are correct, ANTARES will start to be sensitive to the most intense microquasars within a year of data taking.

Finally, a model for the neutrino flux[9] [86] due to GRBs is shown in the figure. In this model, the neutrinos are due to accelerated protons, which interact first in the remnants of the progenitor star (in this case mainly the hydrogen envelope) and later in internal shocks in the GRB jet. GRBs could be detected [87] using external information (provided by satellites) by selecting events that are closely correlated to the GRB in direction and time. The search will then be virtually background free. The results presented here are thus conservative estimates for the discovery potential of ANTARES for GRBs.

[9] In [86], the diffuse flux is given. We have integrated this over 2π sr, i.e. the instantaneous field of view of the detector.

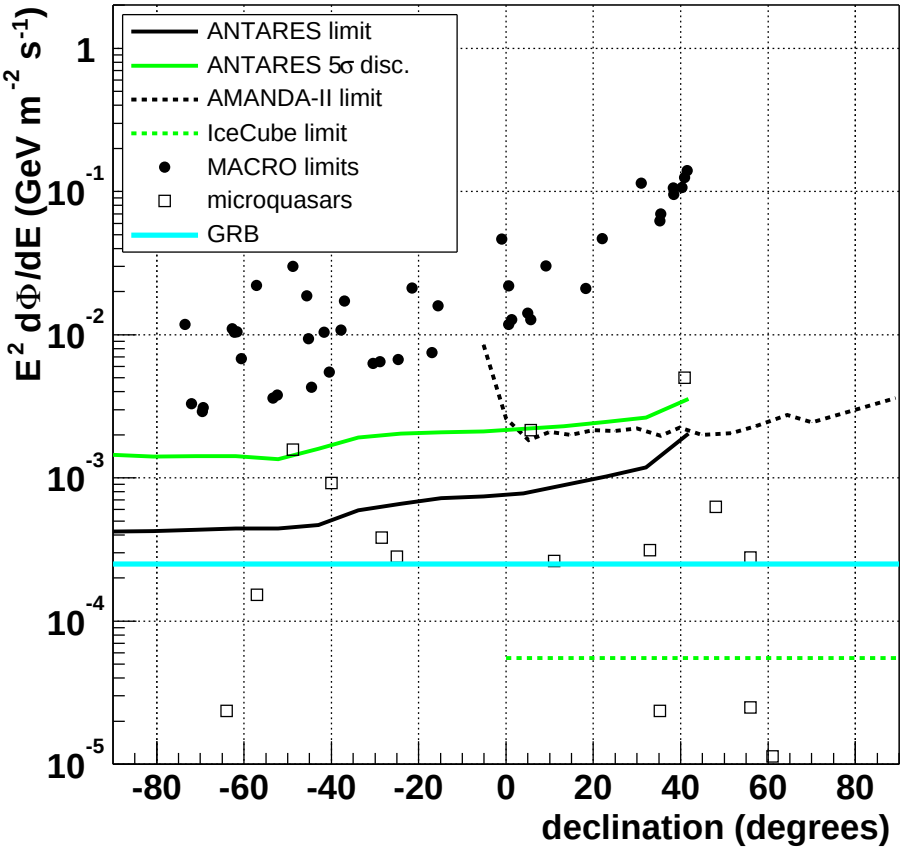

Figure 6.23: *Upper limits (90% CL) on the neutrino flux as a function of declination. Established limits are shown from MACRO (limit on a selected number of sources [81]) and AMANDA-II (average limit) [82]. The expected average limits after one year of data taking are shown for ANTARES and IceCube [84]. The flux needed for a 5σ discovery at ANTARES after one year of data taking is also shown.*

Appendix A

Unbinned likelihood

In this appendix the formula for the unbinned likelihood is derived by taking the expression for the binned likelihood and letting the bin-size go to zero. A similar derivation can be found in e.g. [88].

Consider the case that the data consists of uncorrelated events and that each event is characterised by k observed parameters $x^1, ..., x^k$. Then the events could be binned (into an N-dimensional histogram) and, for each hypothesis (or theory), the expectation value of the number of entries in bin i is given by the k-dimensional integral

$$\mu_i(H) = \int_{\text{bin}_i} \frac{dN(x^1, ..., x^k|H)}{dx^1...dx^k} dx^1...dx^k, \tag{A.1}$$

where $\frac{dN(x^1,...,x^k|H)}{dx^1...dx^k}$ is the number density of expected events with observed parameters $x^1, ..., x^k$ for the hypothesis H and where the integration boundaries are the boundaries of bin i. For small bins, the integral is proportional to the value of the PDF for the observed parameters of event i:

$$\mu_i(H) \propto \frac{dN(x_i^1, ..., x_i^k|H)}{dx^1...dx^k}. \tag{A.2}$$

The observed number of events r_i in bin i is distributed according to a Poisson distribution:

$$P(r_i|\mu_i) = \frac{e^{-\mu_i}\mu^{r_i}}{r_i!}. \tag{A.3}$$

The total log likelihood is given by the sum of the log likelihood of the individual bins:

$$\log P(\text{data}|H) = \sum_i \log P(r_i|\mu_i(H)). \tag{A.4}$$

If the size of the bins is chosen sufficiently small, all bins will contain either zero or one entries; equation A.4 can then be written as

$$\log P(\text{data}|H) = \sum_{i \in B_1} \log(\mu_i e^{-\mu_i}) + \sum_{i \in B_0} \log(e^{-\mu_i}), \tag{A.5}$$

where B_m indicates the collection of all bins with exactly m entries. This can be rewritten as:

$$\log P(\text{data}|H) = \sum_{i \in B_1} \log(\mu_i) - \sum_{i \in \text{all bins}} \mu_i. \tag{A.6}$$

The second term is the total number of predicted events $\langle N_{\text{tot}} \rangle$. The first term can be expressed as a sum over all events:

$$\log P(\text{data}|H) = \sum_{\text{events}} \log\left(\frac{dN(x_i^1, ..., x_i^N|H)}{dx_1 ... dx_N}\right) - \langle N_{\text{tot}} \rangle + C, \tag{A.7}$$

where we have used equation A.2. The constant C does not depend on the hypothesis H and therefore it plays no role when calculating ML estimates or likelihood ratios.

For brevity, we introduce the following definition:

$$\mathcal{N}(x_i^1, ..., x_i^N|H) \equiv \frac{dN(x_i^1, ..., x_i^N|H)}{dx_1 ... dx_N}, \tag{A.8}$$

which is the 'event density'. $\mathcal{N}(x_i^1, ..., x_i^N|H)$ may be thought of as the number of events we expect within a certain interval around the measured values $x_i^1, ..., x_i^N$ for the hypothesis H.

Example

As a simple example, consider the case were $\mathcal{N}$ depends linearly on one of the model parameters, φ, i.e. $\mathcal{N}(x_i^1, ..., x_i^N|H(\varphi)) \propto \varphi$. The ML estimate of φ can be calculated by setting $\frac{\partial}{\partial \varphi} \log P(\text{data}|H(\varphi)) = 0$, which yields

$$\hat{\varphi} = MA, \tag{A.9}$$

where M is the number of observed events, and the constant $A \equiv \frac{\langle N_{\text{tot}} \rangle}{\varphi}$. Thus, the value of $\hat{\varphi}$ is such that the expected number of events precisely equals the actual number of observed events: $\langle N_{\text{tot}} \rangle = M$, irrespective of the observed parameters of the events and irrespective of the other model parameters. One may note the role of the term $-\langle N_{\text{tot}} \rangle$ in equation A.7: if this term were omitted, the likelihood would have no maximum ($\hat{\varphi} = \infty$).

References

[1] B. T. Cleveland et al., *Measurement of the Solar electron neutrino flux with the Homestake chlorine detector.* Astrophys. J. **496**, 505 (1998).

[2] K. S. Hirata et al., *Observation in the Kamiokande-II detector of the neutrino burst from supernova SN1987a.* Phys. Rev. **D38**, 448 (1988).

[3] Q. R. Ahmad et al., *Direct evidence for neutrino flavor transformation from neutral-current interactions in the Sudbury Neutrino Observatory.* Phys. Rev. Lett. **89**, 011301 (2002), nucl-ex/0204008.

[4] K. Hirata et al., *Observation of a neutrino burst from the supernova SN1987a.* Phys. Rev. Lett. **58**, 1490 (1987).

[5] J. C. Van Der Velde et al., *Neutrinos from SN1987a in the IMB detector.* Nucl. Instrum. Meth. **A264**, 28 (1988).

[6] J. G. Learned and K. Mannheim, *High-energy neutrino astrophysics.* Ann. Rev. Nucl. Part. Sci. **50**, 679 (2000).

[7] T. K. Gaisser, *Cosmic rays and particle physics.* Cambridge, UK: Univ. Pr. (1990) 279 p.

[8] M. Nagano and A. A. Watson, *Observations and implications of the ultrahigh-energy cosmic rays.* Rev. Mod. Phys. **72**, 689 (2000).

[9] K. Hagiwara et al., *Review of Particle Physics.* Phys. Rev. **D66**, 010001 (2002).

[10] R. J. Protheroe, *Origin and propagation of the highest energy cosmic rays* (1996), astro-ph/9612212.

[11] K. Greisen, *End to the cosmic ray spectrum?* Phys. Rev. Lett. **16**, 748 (1966).

[12] G. T. Zatsepin and V. A. Kuzmin, *Upper limit of the spectrum of cosmic rays.* JETP Lett. **4**, 78 (1966).

[13] A. Mücke, et al., *Photomeson production in astrophysical sources* (1998), astro-ph/9905153.

[14] L. Nellen et al., *Neutrino production through hadronic cascades in AGN accretion disks.* Phys. Rev. **D47**, 5270 (1993), hep-ph/9211257.

[15] F. W. Stecker and M. H. Salamon, *High energy neutrinos from quasars.* Space Sci. Rev. **75**, 341 (1996), astro-ph/9501064.

[16] E. Waxman, *Cosmological gamma-ray bursts and the highest energy cosmic rays.* Phys. Rev. Lett. **75**, 386 (1995), astro-ph/9505082.

[17] E. Waxman and J. N. Bahcall, *High energy neutrinos from cosmological gamma-ray burst fireballs.* Phys. Rev. Lett. **78**, 2292 (1997), astro-ph/9701231.

[18] J. Hjorth et al., *A very energetic supernova associated with the gamma-ray burst of 29 march 2003.* Nature. **423**, 847 (2003), astro-ph/0306347.

[19] S. Razzaque, et al, *Neutrino signatures of the supernova - gamma ray burst relationship* (2003), astro-ph/0308239.

[20] R. Enomoto et al., *The acceleration of cosmic ray protons in the supernova remnant RX J1713.7-3946.* Nature **416**, 823 (2002).

[21] O. Reimer et al., *No evidence yet for hadronic TeV gamma-ray emission from SNR RX J1713-3946.* Astron. Astrophys. **390**, L43 (2002), astro-ph/0205256.

[22] R. J. Protheroe et al., *Gamma-rays and neutrinos from very young supernova remnants.* Astropart. Phys. **9**, 1 (1998), astro-ph/9703045.

[23] M. Roy, *Ultra high energy neutrinos from supernova remnants.* J. Phys. **G25**, 129 (1999), astro-ph/9901215.

[24] D. Guetta and E. Amato, *Neutrino flux predictions for galactic plerions.* Astropart. Phys. **19**, 403 (2003), astro-ph/0209537.

[25] A. Levinson and E. Waxman, *Probing microquasars with TeV neutrinos.* Phys. Rev. Lett. **87**, 171101 (2001), hep-ph/0106102.

[26] C. Distefano et al., *Neutrino flux predictions for known galactic microquasars.* Astrophys. J. **575**, 378 (2002), astro-ph/0202200.

[27] K. Mannheim, *Gamma-rays and neutrinos from a powerful cosmic accelerator.* Phys. Rev. **D48**, 2408 (1993), astro-ph/9306005.

[28] S. Colafrancesco and P. Blasi, *Clusters of galaxies and the diffuse gamma-ray background.* Astropart. Phys. **9**, 227 (1998), astro-ph/9804262.

[29] W. Bednarek and R. J. Protheroe, *Gamma rays and neutrinos from the Crab Nebula produced by pulsar accelerated nuclei.* Phys. Rev. Lett. **79**, 2616 (1997), astro-ph/9704186.

[30] G. Ingelman and M. Thunman, *High energy neutrino production by cosmic ray interactions in the Sun.* Phys. Rev. **D54**, 4385 (1996), hep-ph/9604288.

[31] T. K. Gaisser et al., *Gamma-ray production in supernova remnants.* Astrophys. J. **492**, 219 (1998), astro-ph/9609044.

[32] A.M. Atoyan et al., *On the gamma-ray fluxes expected from Cassiopeia A* (2000), astro-ph/0001186.

[33] A. Letessier-Selvon, *Auger: A large air shower array and neutrino telescope* (2002), astro-ph/0208526.

[34] F. Blanc, et al., *Dark matter searches with the ANTARES neutrino telescope.* Presented by L. Thompson on behalf of the ANTARES Collaboration, to appear in the proceedings of 28th International Cosmic Ray Conferences (ICRC 2003), Tsukuba, Japan, 31 Jul - 7 Aug 2003.

[35] M. C. Gonzalez-Garcia and Y. Nir, *Neutrino masses and mixing: Evidence and implications.* Rev. Mod. Phys. **75**, 345 (2003).

[36] M. C. Gonzalez-Garcia and C. Pena-Garay, *Three-neutrino mixing after the first results from K2K and KamLAND* (2003), hep-ph/0306001.

[37] R. Gandhi et al., *Neutrino interactions at ultrahigh energies.* Phys. Rev. **D58**, 093009 (1998), hep-ph/9807264.

[38] A. Romeyer, *Etude de la sensibilité du détecteur ANTARES à un flux diffus de neutrinos cosmiques de haute énergie.* Ph.D. Thesis, Université de Paris VII, 2003.

[39] A. Okada, *On the atmospheric muon energy spectrum in the deep ocean and its parameterization.* Astropart. Phys. **2**, 393 (1994).

[40] V. Agrawal, et al., *Atmospheric neutrino flux above 1 GeV.* Phys. Rev. **D53**, 1314 (1996), hep-ph/9509423.

[41] J.D. Jackson, *Classical Electrodynamics.* John Wiley & Sons, Inc., 1998.

[42] P. Amram et al., *The ANTARES optical module.* Nucl. Instrum. Meth. **A484**, 369 (2002), astro-ph/0112172.

[43] F. Feinstein, *The analogue ring sampler: A front-end chip for ANTARES.* Nucl. Instrum. Meth. **A504**, 258 (2003).

[44] W. J. Metzger, *Statistical methods in data analysis*, 2001. HEN-343.

[45] D. J. L. Bailey, *Monte Carlo tools and analysis methods for understanding the ANTARES experiment and predicting its sensitivity to Dark Matter.* Ph.D. Thesis, Wolfson College, Oxford, 2002.

[46] S. Ricciardi. Ph.D. Thesis, Università Ferrara, 1996.

[47] G. Ingelman et al., *LEPTO 6.5 - a Monte Carlo generator for deep inelastic lepton-nucleon scattering.* Comput. Phys. Commun. **101**, 108 (1997), hep-ph/9605286.

[48] T. Sjostrand, *High-energy physics event generation with PYTHIA 5.7 and JETSET 7.4.* Comput. Phys. Commun. **82**, 74 (1994).

[49] F. Halzen and A. Martin, *Quarks & Leptons*. John Wiley & Sons, Inc., 1984.

[50] J. Pumplin et al., *New generation of parton distributions with uncertainties from global QCD analysis*. JHEP **07**, 012 (2002), hep-ph/0201195.

[51] R. Gandhi et al., *Ultrahigh-energy neutrino interactions*. Astropart. Phys. **5**, 81 (1996), hep-ph/9512364.

[52] R. M. Barnett, *Evidence in neutrino scattering for righthanded currents associated with heavy quarks*. Phys. Rev. **D14**, 70 (1976).

[53] P. Lipari and T. Stanev, *Propagation of multi-TeV muons*. Phys. Rev. **D44**, 3543 (1991).

[54] P. Antonioli, et al., *A three-dimensional code for muon propagation through the rock: MUSIC*. Astropart. Phys. **7**, 357 (1997), hep-ph/9705408.

[55] Application Software Group, *GEANT, Detector Description and Simulation Tool*, 1993. CERN Program Library Long Writeup W5013.

[56] W. H. Schuster, *Measurement of the Optical Properties of the Deep Mediterranean.* Ph.D. Thesis, University of Oxford, United Kingdom, 2002.

[57] P. B. Price, *Implications of optical properites of ocean, lake and ice for ultrahigh-energy neutrino detection*. Apl. Optics **34** (1997).

[58] C. D. Mobley, *Light and Water: Radiative transfers in natural waters*. Academic Press, 1994.

[59] L. A. Kuzmichev, *On the velocity of light signals in the deep underwater neutrino experiments*. Nucl. Instrum. Meth. **A482**, 304 (2002), hep-ex/0005036.

[60] X. Quan and E. Fry, *Empirical equation for the index of refraction of seawater*. Appl. Optics **34**, 3477 (1995).

[61] N. Palanque-Delabrouille, *Light velocity in the ANTARES site*, 2004. ANTARES internal note Site/2004-4.

[62] E. Scapparone, *HEMAS: a Monte Carlo code for hadronic, electromagnetic and TeV muon components in air shower* (1998), physics/9902043.

[63] J. Wentz et al., *Simulation of atmospheric muon and neutrino fluxes with CORSIKA*. Phys. Rev. **D67**, 073020 (2003), hep-ph/0301199.

[64] G. Battistoni et al, *High energy extension of the FLUKA atmospheric neutrino flux* (2003), hep-ph/0305208.

[65] M. Honda et. al., *Comparison of 3-dimensional and 1-dimensional schemes in the calculation of atmospheric neutrinos*. Phys. Rev. **D64**, 053011 (2001), hep-ph/0103328.

[66] C. G. S. Costa, *The prompt lepton cookbook.* Astropart. Phys. **16**, 193 (2001), hep-ph/0010306.

[67] V. Stenger, *Track fitting for the Dumand Octagon*, 1990. HDC-1-90.

[68] F. Hubaut, *Optimisation et caractérisation des performances d'un télescope sous-marin a neutrinos pour le projet ANTARES.* Ph.D. Thesis, Université de la Méditeranée, 1999.

[69] Numerical algorithms group, *NAG fortran library, online manual*, 2001. Http://www.nag.com/.

[70] P. Payre, *private communication.*

[71] W. H. Press et al., *Numerical recipes in C.* Cambridge University Press, 1993.

[72] Z. Zhang, *Parameter estimation techniques: A tutorial with application to conic fitting.* Image and Vision Computing Journal **15**, 59 (1997).

[73] R. Bruijn, *Muon energy reconstruction in ANTARES using neural networks.* Master's. Thesis, University of Amsterdam, 2002.

[74] A. Romeyer et al., *Muon energy reconstruction in ANTARES and its application to the diffuse neutrino flux* (2003), hep-ex/0308074.

[75] T. Montaruli et al., *ANTARES status report* (2003), physics/0306057.

[76] D. Zaborov, *Simulation of a km^3-scale deep-sea neutrino detector* (2002), hep-ex/0207039. 37th Rencontres de Moriond on Electroweak Interactions and Unified Theories, Les Arcs, France, 9-16 Mar 2002.

[77] G. J. Feldman and R. D. Cousins, *A unified approach to the classical statistical analysis of small signals.* Phys. Rev. **D57**, 3873 (1998), physics/9711021.

[78] P. T. Wallace, *Slalib, positional astronomy library.* Starlink User Note67.61.

[79] E. Carmona, *Study of the event reconstruction and expected performances for point-like sources of the future Antares neutrino telescope.* Ph.D. Thesis, Universitat de València, 2003.

[80] M. Kendal and A. Stuart, *The advanced theory of statisics*, Vol. 2. Griffin & Co, 1978.

[81] M. Ambrosio et. al., *Neutrino astronomy with the MACRO detector.* ApJ **546** (2001), astro-ph/0002492.

[82] J. Ahrens, *Search for extraterrestrial point sources of neutrinos with AMANDA-II* (2003), astro-ph/0309585.

[83] S. Matsuno, *A search for astronomical neutrino sources with the Super-Kamiokande detector*. Prepared for 2nd Workshop on Methodical Aspects of Underwater/Ice Neutrino Telescopes, Hamburg, Germany, 15-16 Aug 2001.

[84] J. Ahrens, *Sensitivity of the IceCube detector to astrophysical sources of high energy muon neutrinos* (2003), astro-ph/0305196.

[85] J. Ahrens, et al., *Icecube: The next generation neutrino telescope at the south pole*. Nucl. Phys. Proc. Suppl. **118**, 388 (2003), astro-ph/0209556.

[86] S. Razzaque, P. Meszaros, and E. Waxman, *Neutrino tomography of gamma ray bursts and massive stellar collapses*. Phys. Rev. **D68**, 083001 (2003), astro-ph/0303505.

[87] F. Blanc, et al., *A data acquisition system for the antares neutrino telescope*. Presented by M.C. Bouwhuis on behalf of the ANTARES Collaboration, to appear in the proceedings of 28th International Cosmic Ray Conferences (ICRC 2003), Tsukuba, Japan, 31 Jul - 7 Aug 2003.

[88] W. Tompkins, *Applications of likelihood analysis in gamma-ray astrophysics* (1999), Ph.D. Thesis, astro-ph/0202141.

Summary

High energy cosmic rays consist mostly of protons which are thought to be accelerated in astrophysical shock waves and which can initiate neutrino production by interactions with photon or matter fields in the accelerating region. Decay of the charged pions produced in these interactions leads to the production of high energy neutrinos. The detection of high energy cosmic neutrinos would therefore shed light on the question on the origin of high energy cosmic rays

The ANTARES collaboration is building a detector for high energy cosmic neutrinos in the Mediterranean Sea. The detector will consist of 900 photomultiplier tubes, which are enclosed in pressure resistant glass spheres and which are positioned along 12 flexible, upright strings with a length of 400 m. This instrument will detect the Cherenkov light produced by muons that result from charged current interactions of muon-neutrinos.

The direction of muons is closely correlated to the neutrino direction, which allows for good angular resolution, provided that the direction of the muon is accurately reconstructed. This reconstruction relies on accurate information on the arrival times of the Cherenkov photons on the photomultipliers. The timing resolution of the detector is expected to be about 1.3 ns. Analysis of data obtained during tests of a prototype detector in the laboratory has confirmed this value.

In order to estimate the performance of the detector, simulations have been performed of the charged current neutrino-nucleon interactions, the propagation of the resulting muons from the interaction point to the detector, the production and propagation of the Cherenkov light through the instrumented volume and the response of the detector.

The algorithm for reconstructing muon tracks consists of several subsequent fitting procedures, which provide increasingly accurate estimates of the track parameters, but which also require increasingly accurate starting points. The final procedure is a maximum likelihood fit. The probability density function of the hit times used in the final fit takes into account the background photons, which are due to decaying ^{40}K and bioluminescence.

After the application of a set of quality criteria to select well reconstructed events, the obtained angular resolution is dominated by the scattering angle between the neutrino and the muon for neutrino energies below 10 TeV. At higher energies, the pointing resolution is dominated by the error on the muon direction and is typically smaller than 0.2°.

The background caused by down-going atmospheric muons that are reconstructed as up-going is rejected to the level of about one event per day by the selection criteria. The remaining background is dominated by atmospheric neutrinos, which account for 10 selected events per day.

A method was developed to search for point-like sources of neutrinos in the background of atmospheric neutrinos. The method is based on a likelihood ratio test. In contrast to

more widely used methods, this method takes into account all available information on the reconstructed direction of the neutrinos, the reconstructed energy and the error estimates provided by the reconstruction. Moreover, the loss of information due to binning effects is minimised.

The performance of the likelihood ratio method was evaluated for a full sky search for a point source of neutrinos with an energy spectrum proportional to E^{-2}. In order to discover the neutrino source at 3(5) σ confidence level after one year of data taking, a flux of $1(1.4) \times 10^{-3}\ E^{-2}$ GeV m^{-2} s^{-1} is needed, if the position of the source in the sky if favourable. This flux is about 35% smaller than the flux needed when using a method which relies only on binning of the reconstructed celestial coordinates of the events. The likelihood ratio method thus results in significant increase in the discovery potential.

The search method can also be used to set an upper limit on the flux from a particular direction. The average expected 90% confidence level upper limit that can be set by ANTARES after one year is between 5×10^{-4} and $2 \times 10^{-3}\ E^{-2}$ GeV m^{-2} s^{-1}, depending on declination. This is an order of magnitude smaller than the present limits for sources in the southern hemisphere. According to model predictions of neutrino fluxes, ANTARES will be sensitive to the most intense sources after about one year of data taking.

Samenvatting

De atmosfeer van de Aarde wordt voortdurend bestookt met zogenaamde kosmische straling, die voornamelijk bestaat uit protonen en andere atoomkernen die ergens in het heelal versneld worden tot zeer hoge energieën. Men gaat er doorgaans van uit dat deze deeltjes versneld worden doordat ze veelvuldig heen en weer 'stuiteren' in de materie die met hoge snelheid wordt uitgestoten door sommige astrofysische objecten. Daarbij kan men bijvoorbeeld denken aan de uitdijende schillen die overblijven na een supernova of aan de 'jets' die worden uitgespuwd door de kernen van sommige melkwegstelsels. Hoewel dit versnellingmechanisme veel van de waargenomen eigenschappen van de kosmische straling kan verklaren, is het echter nog niet gelukt vast te stellen welke objecten er precies verantwoordelijk zijn voor die versnelling. Dit komt onder andere doordat de elektrisch geladen deeltjes, waar de kosmische straling uit bestaat, worden afgebogen door de magnetische velden die zich in het heelal bevinden. Daardoor is de richting van de op Aarde gedetecteerde deeltjes niet gecorreleerd met de richting waarin hun bron gezocht moet worden.

Een veelbelovende manier om uit te vinden waar de kosmische straling vandaan komt is het detecteren van kosmische neutrino's. Neutrino's zijn elektrisch neutrale, elementaire deeltjes met de bijzondere eigenschap dat ze nauwelijks interacties aangaan met andere deeltjes. Als gevolg hiervan wordt hun richting niet beïnvloed door magnetische velden en kunnen ze de Aarde bereiken zonder geabsorbeerd te worden door interstellaire materie of straling. Neutrino's met een hoge energie (hoger dan ongeveer 100 GeV) kunnen geproduceerd worden in interacties van hoog-energetische protonen met bijvoorbeeld fotonen. Bij zulke interacties worden geladen pionen geproduceerd die vervallen naar neutrino's. Men verwacht dat zulke processen zich afspelen in de bronnen van de kosmische straling; daar worden immers protonen tot zeer hoge energieën versneld. Het observeren van een neutrinobron aan de hemel zou daarom een sterke aanwijzing zijn voor de oorsprong van de kosmische straling; temeer omdat er nauwelijks andere processen denkbaar zijn waarin neutrino's met dermate hoge energie geproduceerd worden (dit in tegenstelling tot neutrino's met energieën van rond de MeV, die geproduceerd worden in sterren en supernovae).

De geringe interactie die neutrino's hebben met materie, maakt ze echter ook moeilijk te detecteren. Daarom is een zeer groot detectievolume nodig om een redelijke kans te hebben een signaal te zien. In dit proefschrift wordt de ANTARES detector beschreven, die een afmeting zal hebben van ongeveer $200 \times 200 \times 400$ m^3. Deze detector wordt gebouwd op de bodem van de Middellandse Zee, zo'n 40 km uit de kust van Frankrijk, op een diepte van 2,4 km. Het neutrino zelf kan niet direct worden waargenomen, maar bij een interactie van een muon-neutrino met een atoomkern in het zeewater of in de

aarde eronder, kan een muon worden geproduceerd, dat wel waargenomen kan worden. Door de hoge impuls van het neutrino is de richting van het muon nagenoeg gelijk aan die van het neutrino, zodat de richtingsinformatie behouden blijft. Dit muon is elektrisch geladen en zendt het licht uit wanneer het zich, met bijna de lichtsnelheid, door het zeewater beweegt. De ANTARES detector zal bestaan uit 900 fotomultiplicatoren, die dit zogenaamde Cherenkov licht detecteren. Door de aankomsttijd van het licht op de verschillende fotomultiplicatoren te meten, kan de richting van het muon worden bepaald. Hiervoor is een meetnauwkeurigheid van ongeveer 1 ns nodig. Tests die zijn uitgevoerd met een prototype detector in het laboratorium hebben aangetoond dat deze nauwkeurigheid inderdaad gehaald wordt.

Een van de onderwerpen van dit proefschrift is de methode die gebruikt wordt om uit de aankomsttijden van het licht zo nauwkeurig mogelijk de richting en de positie van het muon te reconstrueren. Dit proces wordt bemoeilijkt door de aanwezigheid van achtergrond licht, dat veroorzaakt wordt door natuurlijke radioactiviteit van het zeezout en door lichtgevende organismes. Tevens moet er rekening gehouden worden met verstrooiing van het licht in het water en het licht dat veroorzaakt wordt door secundaire deeltjes. De ontwikkelde methode heeft vier verschillende stadia, die een steeds nauwkeurigere schatting geven van het muon spoor. In het laatste stadium wordt een 'maximum likelihood' methode gebruikt waarbij bovengenoemde complicaties worden meegenomen in de kansdichtheidsfunctie. Van neutrino's met een energie groter dan 10 TeV kan zodoende de richting worden bepaald met een nauwkeurigheid van ongeveer $0,2^\circ$. Verder blijkt het mogelijk om met een paar simpele selectiecriteria slecht gereconstrueerde muonen van de goede te scheiden. Door alleen opgaande muonen te selecteren wordt de achtergrond van neergaande atmosferische muonen, die gemaakt worden in interacties van kosmische straling in de atmosfeer boven de detector, sterk onderdrukt. Zo wordt dus vooral de zuidelijke hemel geobserveerd. De resterende achtergrond bestaat uit atmosferische neutrino's.

Een ander onderwerp dat in dit proefschrift beschreven wordt is een methode om te zoeken naar bronnen van kosmische neutrino's. Een astrofysische bron van neutrino's zal aan de hemel een puntbron lijken. De observatie van een aantal neutrino's die uit hetzelfde punt aan de hemel komen, zou een indicatie kunnen zijn voor de aanwezigheid van zo'n puntbron, maar door de eindige meetnauwkeurigheid van de detector zullen de neutrino's niet precies uit hetzelfde punt lijken te komen. We zoeken dus naar een cluster van neutrino's met ongeveer dezelfde gereconstrueerde richting. Zo'n cluster kan echter ook worden veroorzaakt door atmosferische neutrino's. Het zoeken naar een puntbron komt neer op het zo goed mogelijk onderscheiden van deze twee gevallen.

De meest gangbare methodes om naar puntbronnen te zoeken beperken zich tot het tellen van het aantal neutrino's dat zich in een cluster bevindt. De methode die in dit proefschrift beschreven wordt, gebruikt echter nog meer informatie. Zo wordt er gebruik gemaakt van informatie over de onderlinge positie van de neutrino's en van gemeten waarde van de muon-energie. Door deze informatie te gebruiken wordt de gevoeligheid van de detector om een puntbron te ontdekken vergroot met zo'n 35%. Een bijkomend voordeel is dat deze methode een nauwkeurige bepaling levert van de positie van de bron aan de hemel.

Uiteindelijk is een schatting gemaakt van de neutrino flux die nodig is voor een ontdekking. Na een jaar waarnemen zal ANTARES de bestaande bovengrenzen voor de flux

uit bronnen aan de zuidelijke hemel verbeteren met ongeveer een factor 10 en zodoende een waardevolle aanvulling zijn op de AMANDA neutrino telescoop op de zuidpool, die reeds begonnen is de noordelijke sterrenhemel te bestuderen.

Dankwoord

This thesis would not have been possible without the help and support of many people. I would like to thank the members of the ANTARES collaboration for a very enjoyable time and for all the help and encouragement I have received over the past five years.

Mijn promotor, Jos Engelen, bedank ik voor zijn vertrouwen en zijn steun op de belangrijke momenten. Els de Wolf, mijn co-promotor, was er voor de dagelijkse begeleiding. Zij heeft, naast het veelvuldig verbeteren van eerdere versies van het proefschrift, vaak geholpen bij de organisatorische kanten van het promoveren. Ik dank ook alle anderen die suggesties hebben gegeven voor verbeteringen aan het manuscript.

Maarten dank ik voor zijn grote enthousiasme voor mijn werk en dat van de andere promovendi. Dit heeft ertoe bijgedragen dat ik in de loop der jaren de NIKHEF-ANTARES groep als een zeer motiverende werkomgeving ben gaan ervaren. Ook de komst van Bram en Mieke heeft hier een belangrijk aandeel in gehad. Bram was een uitstekend kamergenoot en ik laat vol vertrouwen H351 met alle toebehoren in zijn beheer achter. Mieke dank ik voor haar analyses van het reilen en zeilen binnen ANTARES, die mij regelmatig hebben opgevrolijkt. Ik wens jullie alle succes met het voltooien van jullie proefschriften. En dat geldt natuurlijk ook voor Garmt, Ronald, Claudine en Hylke.

Veel van wat ik de afgelopen vijf jaar geleerd heb, heb ik te danken aan mijn collega promovendi. Ik heb genoten van de gesprekken met Niels en Ivo over inktvissen, statistiek en natuurkunde. De vele discussies met Marco, Rutger, Paul, Mark, René en Martin, die vaak plaatsvonden onder het genot van een pizza en één biertje, zal ik niet snel vergeten. Ook voor vragen over C++, LaTeX, of data-analyse kon ik altijd wel bij een van deze mensen de kamer binnenwandelen.

Mijn andere vrienden uit Amsterdam (Misja en de rest van W94) en Hoorn wil ik ook bedanken voor hun steun en belangstelling (en het soms verfrissende gebrek daaraan). Tot slot bedank ik mijn ouders voor het onvoorwaardelijke vertrouwen dat ze altijd in mij gehad hebben.